UNIVERSITÉ CATHOLIQUE DE LOUVAIN

INSTITUT DE PHYSIQUE THÉORIQUE

PROBING THE DYNAMICS IN SEQUENCES OF SOLAR ATMOSPHERIC IMAGES: ALGORITHMS AND RESULTS

Investigation de la dynamique de l'atmosphère solaire dans les séquences d'images: algorithmes et résultats

Membres du jury:

Prof. J.-P. Antoine (Promoteur)
Dr. J.-F. Hochedez (Co-promoteur)
Pr. D. Favart (Président du jury)
Pr. V. Barra
Dr. M. Crucifix
Dr. L. Jacques
Dr. V. Pierrard
Dr. R. Brajša

Thèse présentée en vue de l'obtention du grade de Docteur en Sciences par :

Samuel Gissot

September 2009

Acknowledgements

This PhD has been for me extremely exciting and instructive. It is a pleasure to acknowledge the persons listed on this page. Their encouragements and support have enabled my research and for this reason I would like this presentation of my results to be a tribute to their various contributions.

First of all, I would like to thank my supervisor, Professeur Jean-Pierre Antoine, for his inspiring and encouraging way to guide me to a deeper understanding of the wavelet theory, and his invaluable comments during the whole work.

I am grateful to Jean-François Hochedez, who is the co-promoter of this work. Despite his other important responsibilities, he has constantly acted as the guardian of our research, feeding me with insightful advices. He protected the original objectives, and solved with me difficult administrative and scientific problems. I would like to thank him heartily and look forward to collaborating further.

I am indebted to all my past and current colleagues of the Royal Observatory of Belgium and very grateful to the SIDC team, especially my office colleagues Ali Benmoussa, Andrei Zhukov, and Marie Dominique for all the discussions we had.

I have had a very interesting collaboration with Pierre Chainais, Vincent Barra and Émilie Koenig from ISIMA, Université de Clermont-Ferrand, leading to a fruitful project dealing with the synthesis of solar images for the calibration of the stereoscopic reconstruction. I also had the chance to enjoy a profitable collaboration with CEREMADE of Université de Paris-Dauphine: Françoise Dibos, Valérie Charoing, and Olivia Sanchez.

I also acknowledge Bernd Inhester for the great discussions I have had with him.

I also would like to thank the Université catholique de Louvain for supporting this PhD project, and in particular Laurent Jacques.

This work has been partially sponsored by the Air Force Office of Scientific Research (EOARD), USA, under grant number FA8655-05-1-3021.

The financial support has been provided by the Royal Observatory of Belgium and the Belgian government through PRODEX.

Finally, I would like to thank Pierre Cugnon who was the director of the department when I joined the Royal Observatory of Belgium.

Abstract

The dynamic nature of the solar atmosphere has been widely observed since the first telescopic observations of the Sun that began around 1610 with Galileo Galilei. The last two decades have highlighted the unsuitability of static assumptions in studying the physics of the chromosphere, the transition region, and the corona. In this work we investigate the dynamics of the solar atmosphere as observed by imaging telescopes in extreme ultraviolet (EUV) passbands. The dynamics is concerned with the study of fluid motion: we present algorithms of motion analysis specifically adapted to solar EUV images as produced by the EUV imaging telescope (EIT) on board the SoHO space mission, and other imagers onboard the TRACE and STEREO space missions. We present a multiscale optical-flow algorithm based on the Lucas-Kanade method and we apply it to the processing of EIT and TRACE series of EUV images. It can reliably retrieve motion from two successive images. We will demonstrate that this algorithm can be used for the detection and the analysis of coronal loop oscillations over long time periods via a tracking method over more than two images. The tracking technique is extended to the analysis of the solar rotation over the 23rd solar cycle that is now covered by the EIT archive. Using STEREO EUVI images, we introduce a stereoscopic reconstruction method achieving 3D reconstructions of filaments using the STEREO data. We also develop a spatio-temporal method of motion estimation based on a motion-oriented continuous wavelet transform, and we present its application on EUV images of the solar atmosphere. The results presented in this work illustrate how these novel methods are able to improve the existing observational methods of motion measurement: it represents a breakthrough that enables to quantify, in a reproducible way, measurements that are habitually achieved via manual methods and human observers. These developments also have a potential for chromospheric or coronagraphic image sequences, and for future observations from EUV solar imagers such as ESA PROBA2-SWAP and NASA SDO-AIA.

Résumé

La nature dynamique de l'atmosphère solaire a été observée depuis les premières observations télescopiques du Soleil depuis 1610 et les travaux de Galilée. Au cours des deux dernières décennies, il a été mis en évidence que les hypothèses statiques sont inadaptées à l'étude de la physique de la chromosphère, de la région de transition et de la couronne. Dans ce travail, nous développons des outils de mesure de la dynamique de l'atmosphère solaire observée par les télescopes dont les imageurs sont sensibles à des bandes passantes dans le domaine de l'extrême ultra-violet. La dynamique concerne l'étude des flots de fluide: ici nous présentons des algorithmes d'analyse de mouvement adaptés aux images EUV du Soleil telles que celles produites par le télescope EIT à bord de la sonde spatiale SoHO, ainsi que celles des missions spatiales TRACE et STEREO. Nous présentons un algorithme de flot optique multiéchelle basé sur la méthode Lucas-Kanade, et que nous appliquons au traitement des séquences d'images EUV fournies par EIT et TRACE. Ces techniques permettent des estimations de mouvement à partir d'une séquence de deux images successives. Nous démontrons que cette méthode peut être étendue à l'étude des oscillations des boucles coronales grâce à une méthode de suivi pour des séquences de plus de deux images. Cette technique de suivi est également utilisée pour l'analyse de la rotation du Soleil au cours du 23ème cycle solaire maintenant couvert par l'archive des images EIT. Nous introduisons une méthode de reconstruction stéréoscopique permettant la reconstruction 3D de filaments à partir d'images fournies par le télescope EUVI à bord des sondes STEREO. Nous développons également une méthode basée sur la transformée en ondelette spatio-temporelle et décrivons ses applications aux images EUV de l'atmosphère solaire. Les résultats présentés dans cette thèse de doctorat représentent une avancée considérable vers une validation d'outils d'estimation de mouvements et de dynamique dans les images solaires qui permettent désormais d'obtenir des mesures quantifiées et reproductibles. Ces travaux pourront être appliquées aux futures images fournies par SWAP à bord de PROBA2 ainsi qu'à celles fournies par AIA à bord de SDO.

Contents

List of Figures

List of Tables

Acronyms

ACE Advanced Composition Explorer

AIA Atmospheric Imaging Assembly

AR Active Region

AU Astronomical Unit

BCA Brightness Constancy Assumption

BV Brightness Variation

CH Coronal Hole

CCD Charge-Coupled Device

CDS Coronal Diagnostic Spectrometer

CME Coronal Mass Ejection

COI Cone of Influence

CR Count Rate

CRH Cosmic Ray Hit

CWT Continuous Wavelet Transform

DEM Differential Emission Measure

EIT Extreme ultraviolet Imaging Telescope

EM Emission Measure

EUI Extreme Ultraviolet Imager

EUV Extreme Ultraviolet

EUVI Extreme UltraViolet Imager

FOV Field of View

FFT Fast Fourier Transform

IDL Interactive Data Language

LASCO Large Angle and Spectrometric Coronagraph Experiment

LCT Local Correlation Tracking

LK Lucas-Kanade

LOS Line-Of-Sight

LS Least Squares

LUA Local Uniformity Assumption

MH Mexican Hat

MHD Magnetohydrodynamics

MK Mega Kelvin

MSE Mean Square Error

MTSTWT Motion-Tuned Spatio-Temporal Wavelet Transform

NASA National Aeronautics and Space Administration

NRL Naval Research Laboratory

OFCE Optical Flow Constraint Equation

PDE Partial Differential Equation

PFSS Potential Field Source Surface Model

PIL Polarity Inversion Line

PLS Point-like Structures

QS Quiet Sun

ROB Royal Observatory of Belgium

SDO Solar Dynamics Observatory

SECCHI Sun Earth Connection Coronal and Heliospheric Investigation

SEP Solar Energetic Particles

SIDC Solar Influences Data Analysis Center

SMEX Small Explorer

SNR Signal-to-Noise Ratio

SOFA Symmetric Optical Flow Analysis

SOHO Solar and Heliospheric Observatory

STEREO Solar TErrestrial RElations Observatory

SUMER Solar Ultraviolet Measurements of Emitted Radiation

SXT Solar X-Ray Telescope

TR Transition Region

TRACE Transition Region and Coronal Explorer

Introduction

A major field of solar physics is the study of the solar atmosphere. The Sun is a magnetized star of spectral type G and luminosity class V that is mostly made of hydrogen and helium with a small amount of heavier elements. The solar radius $R_\odot$ is approximately 6.955×10^8 m and its mass is 1.9891×10^{30} kg. The Sun's interior includes four regions (see Figure 1): from its centre to $0.25\, R_\odot$ is the core where the energy is generated by nuclear fusion converting hydrogen to helium. Between 0.25 and $0.7\, R_\odot$ is the radiative zone, where the energy emanating from the core diffuses outward by gamma- and x-rays radiation. Outward the radiation zone, the energy is transported via fluid flows through the convection zone in the outermost $0.3 R_\odot$ of the solar interior up to the solar surface. The tachocline is a thin interface layer between the radiative zone and the convection zone is where the solar magnetic field is thought to be generated. A good introduction to the physics of the Sun can be found *e.g.* in [37].

The dynamic nature of the solar atmosphere has been widely observed and since the first telescopic observations of the Sun that began around 1610 and dedicated to the study of the photospheric sunspots by Galileo Galilei. The present work deals with the probing, through measurements, of the dynamics in Extreme Ultraviolet (EUV) images of the solar atmosphere, namely the chromosphere, the transition region and the corona.

The Solar Atmosphere

The atmosphere of the Sun is a magnetized plasma that is made up of several regions located above the solar visible surface named photosphere. The extended solar atmosphere is observed during total solar eclipses, and is defined as the corona. The thin red layer close to the photospheric limb and observed for a few seconds just before and after the eclipse totality is the chromosphere. The thin layer that is conceptually located between the chromosphere and the corona is the Transition Region (TR).

The coronal plasma is a complex and non-uniform environment controlled by the magnetic field and its transients. The corona is thus not precisely defined, since it is inhomogeneous and has a non-stationary behavior. The three different regions (the chromosphere, the transition region and the corona) in the solar atmosphere above the photosphere (see Figure 1) are characterized by their height, their temperature and their density ranges. The chromosphere is located above the photosphere; the height of the chromosphere above the solar surface (at one solar radius) is equal to two or three thousand kilometres above the solar surface, and the temperature grows up from 5800 K to 20000 K. The transition region is a very thin “fractal” layer (its thickness is about 500 km) within which the temperature increases dramatically by almost two orders of magnitudes up to approximately 10^6 K (see Figure 2). The height of the transition region varies depending on the location because of the inhomogeneity of the solar corona. Above the transition region starts the corona observed by naked eye during eclipse totality. This is where the solar wind accelerates.

The emission of the solar corona includes four parts (K,F,E,T); in our applications, we observe the E-(Emission) corona. The E-corona is caused by emission of radiation by coronal highly-ionized atoms. This term was originally used for the emission lines in visible light, but we can extend it now to EUV spectral lines. As we know the temperature of existence of these species, as well as the wavelengths of their emission lines, we interpret the EUV images according to the temperature and the density of the emitting plasma elements.

On the photosphere, one can observe sunspots that appear as dark spots. The temperature near the center of sunspots drop to about 3700 K [37] and are thus colder than the surrounding photosphere whose temperature is 5800 K. They typically last for several days, but the largest ones may last for months. Sunspots are magnetic regions on the Sun with magnetic field strengths thousands of times stronger than the Earth’s magnetic field up and whose intensity can reach 3000 G. Sunspots usually come in groups with two sets of spots. One set will have positive or north magnetic field while the other set will have negative or south magnetic field. The field is strongest in the darker parts of the sunspots - the umbra, and is weaker and more horizontal in the lighter part - the penumbra. Areas near sunspots often flare up, heating material to millions of degrees in minutes and blasting billions of tons of material into space: the solar flares.

Scientific Challenges in Solar Physics

In modern solar physics, several problems remain unsolved even and are of vital importance to understand the Sun. We here detail unanswered questions in solar physics: the coronal heating process, the mechanisms of solar eruptions, the origin of the solar cycle of activity as well as the cause of the acceleration of the solar wind.

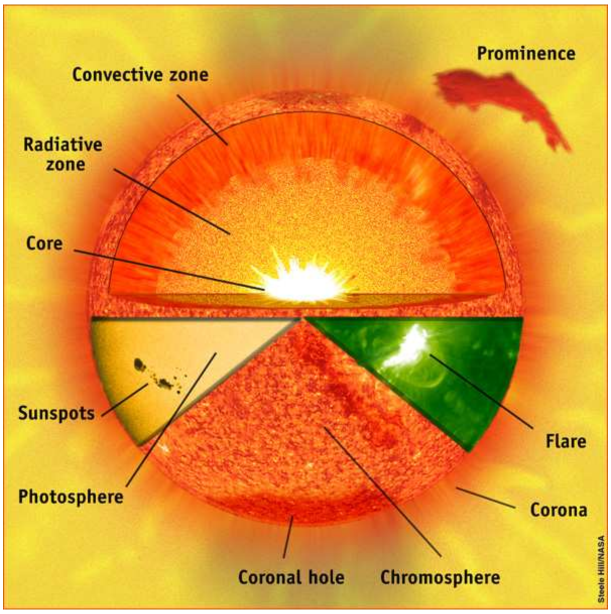

Figure 1: Introduction to the Sun internal and external components. The three major interior zones are the core, the radiative zone, and the convection zone. The energy is generated by nuclear reactions in the core. Heat travels outward by radiation through about $0.7 \times R_{\odot}$ of the Sun, and in the last zone the convection carries the energy to the surface. The flare, sunspots and photosphere, chromosphere, and prominence are all from actual images on the Sun. From NASA website `http://learn.arc.nasa.gov`.

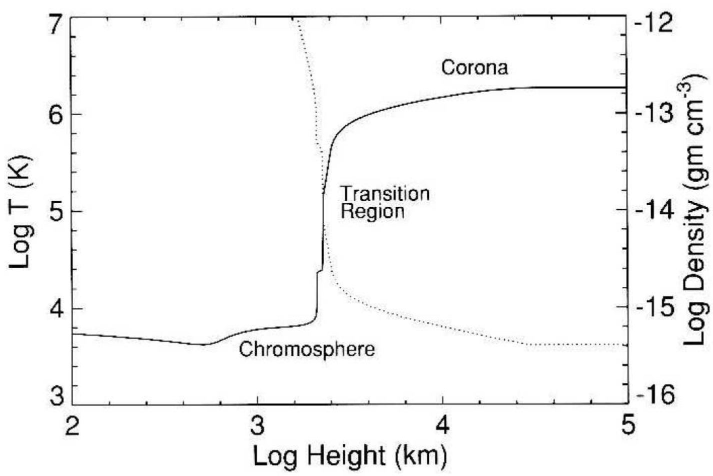

Figure 2: The three solar external zones above photosphere: the chromosphere, the transition region and the corona. Average temperature (solid line) and density (dotted line) structure of the chromosphere, transition region and corona (quiet conditions). Here the solar atmosphere is modeled [38] in 1D assuming hydrostatic equilibrium. From Mariska [69].

Coronal Heating

The Sun's outer atmosphere (the corona) is much hotter than the visible surface. It has a low density as illustrated in Figure 2. The corona is two orders of magnitude hotter than the underlying photospheric surface that is at an effective temperature of circa 5785 K [43]. As the height increases, the temperature increases up to more than 10^6 K contradicting the second law of thermodynamics stating that heat cannot spontaneously flow from a region at lower temperature to a region at higher temperature. Thus, the observed high temperatures require energy to be carried from the solar interior to the corona by non-thermal processes. This temperature increase occurs in the transition region, a region that is believed to to be only ~ 500 km wide. Several theoretical mechanisms have been proposed to explain this phenomenon, but none of them is consistent with observations and there is no consensus on which one, or which combination of them, is really responsible. The exact nature of the processes that heat the corona and produces the solar wind remains an scientific enigma. The two mechanisms favored include the dissipation of the mechanical and electromagnetic energy of Magnetohydrodynamics (MHD) waves (alternative current, AC heating) and the Joule dissipation of currents along the magnetic field lines (direct current, DC); the present understanding is that the coronal heating can be explained by a combination of AC and DC heating, depending on the solar region and its activity.

The Trigger of Solar Flares and Coronal Mass Ejection (CME)

Here again, we now know many facts about the eruptive events such as flares and CMEs, and we understand the basic mechanisms, but many details are missing. We still cannot reliably predict when and where a flare will occur or how big it will be. A deeper understanding of the physics of the corona is also needed for space weather services, which attempt to predict the influence of the Sun activity on the Earth environment. A CME is a transient event with ejection of plasma material. They are very well seen in the Large Angle and Spectrometric Coronagraph Experiment (LASCO) coronagraphs onboard SOHO. In EUV images, such as in the 19.5 nm passband, a CME sometimes appears as a dimming of intensity or as an "EIT wave". CMEs are often associated with solar flares and/or prominence eruptions but they can also occur in the absence of either of these processes. The frequency of CMEs follows the sunspot cycle: at solar minimum we observe about one CME per week, while near the solar maximum we observe an average of 2 to 3 CMEs per day.

The Origin of the Solar Cycle

Using ground- and space-based solar instruments, cycle studies exhibit a 11-year cycle and possibly cycles of longer periods in the activity of the Sun. Over about 11 years the Wolf's number index of sunspots seen on the Sun increases from nearly zero to over 100 and then decreases to near zero again as the next cycle starts. The butterfly diagram at the photospheric level is obtained either from the sunspot locations and area (see Figure 6) or from magnetogram data. The period of 11 years is variable: for instance, the 23rd solar cycle started in 1996 and ended in 2008. When a new cycle of activity starts, new sunspots and their solar atmospheric counterparts, the active regions, occur at high latitudes (30 degrees) in the southern and the northern hemisphere of the Sun (see for instance [81]). The maximum of activity is attained when the sunspot number is at its maximum, reached near 2002 during the 23rd solar cycle. Towards the solar minimum, they occur at lower latitudes, close to the equator, and are less numerous. The other solar activity indices, such as solar total irradiance, also follows this cycle. The nature and causes of the sunspot cycle constitute one of the great mysteries of solar astronomy. Dynamo mechanisms have been proposed to explain the 11-year cycle of the sunspots. While we now know many details about the sunspot cycle, and also about some of the dynamo processes that must play key roles in producing it, we are still unable to produce a model that will allow us to reliably predict future sunspot numbers using basic physical principles.

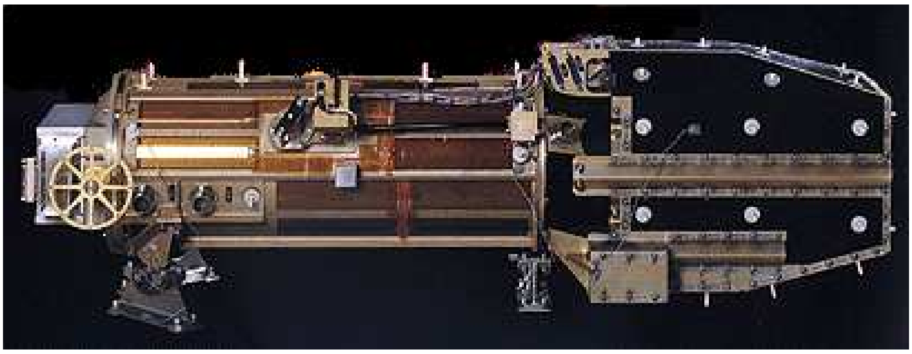

Figure 3: A picture of the EIT telescope, from Delaboudinière *et al.* [28].

The Acceleration of the Solar Wind

The solar wind is a continuous flux of charged particle streams outward from the Sun to interstellar space. A yet unanswered question is the location and the reason of the acceleration of the solar wind. It is accepted that the fast wind originates from coronal holes, while the sources of slow wind are not well identified: it is possible that they are located in bright streamers near active region [37]. The reader may find good introductions to this subject in [58] and [10]. The discrepancy between wind speed measurements and simple models could be explained by adjusting existing models through consideration of wave pressure, heat transport in the collisionless plasma, or effects of kinetic models [64]. But a real understanding of solar wind sources and acceleration processes may require detailed analysis of their links to the unsolved problems of the accelerations of spicules and high-speed jets in the chromosphere and transition region and their contribution to coronal heating.

History of EUV Imaging of the Solar Atmosphere

The study of solar physics has been revolutionized by observations from space with imaging telescope onboard spacecrafts. There are three major reasons for observing the Sun from above the Earth's atmosphere. The main reason is that it extends the range of available wavelengths to otherwise inaccessible spectral lines since the Earth's atmosphere highly absorbs at these wavelengths. Other reasons are reducing scattering and distortion, and the continuity of coverage that is more difficult to achieve using ground-based instruments because of bad seeing conditions.

A breakthrough for coronal observations therefore started with the space era of rocket flights and spacecraft missions, which enabled soft X-ray and EUV observations above the absorbing Earth's atmosphere. Early rocket flights were conducted by the U.S. Naval Research Laboratory (NRL) in 1946 and 1952, recording spectrograms at EUV wavelengths down to 190 nm and Lyman-α emission of H I at 121.6 nm. Solar physics then made progress thanks to X-ray photographs of the Sun obtained by Friedman in 1963 with a pinhole camera from a NRL rocket in 1960. These rocket flights last typically about 7 minutes, and thus allowed only for short glimpses of coronal observations. A series of eight satellites known as the Orbiting Solar Observatories provided much of the space-based solar observations through the 1960s and were launched into orbit during 1962-1975, equipped with non-imaging EUV, soft X-ray, and hard X-ray spectrometers and spectroheliographs. Although the OSO satellites (OSO-1 to OSO-8) were modest in size with relatively small instruments, they permitted long-term observations of the Sun at these wavelengths. The Skylab space-station mission, which operated from May 14, 1973 to February 8, 1974 was launched by NASA : Skylab carried a white-light coronagraph, two grazing-incidence X-ray telescopes, EUV spectroheliometers/spectroheliographs, and an UV spectrograph. Skylab allowed long-focal-length solar telescopes to be flown in space for the first time and its data are still being used today. Skylab made a number of important discoveries which significantly enhanced our knowledge of solar activity.

In the three decades following the launch of Skylab many solar observatories have been placed in space; the advent of orbiting satellites opened the way for continuous solar observations at wavelengths unreachable from the Earth. The Solar Maximum Mission (SMM) spacecraft was launched on February 14, 1980, near the maximum of the solar cycle, to enable the solar physics community to examine flares in more physically meaningful details than ever before. We present here the missions such as SOHO, TRACE, and Solar TErrestrial RElations Observatory (STEREO). Other successful solar missions include Solar-A and Solar-B (Hinode), Coronas- I and F.

Observing the Sun with EUV Telescopes

Hereafter we introduce with more details the three ongoing missions that provided the data we use in this work. The following projects maintains an Open Data Policy: all data are available from the data archives to the science community as soon as the spacecraft data have been processed.

SOHO-EIT

The SOHO spacecraft has been launched on December 2, 1995, just before solar minimum and was sent to the Sun-Earth L1 Lagrange point, at 1.5×10^6 km from Earth. The EIT, see Figure 3, is an instrument onboard SOHO providing images in four wavelengths. The mission has covered completely the solar cycle 23: it has enabled the study of coronal activity from the minimum to the maximum of the solar cycle. Human observations and interpretations have nowadays become almost

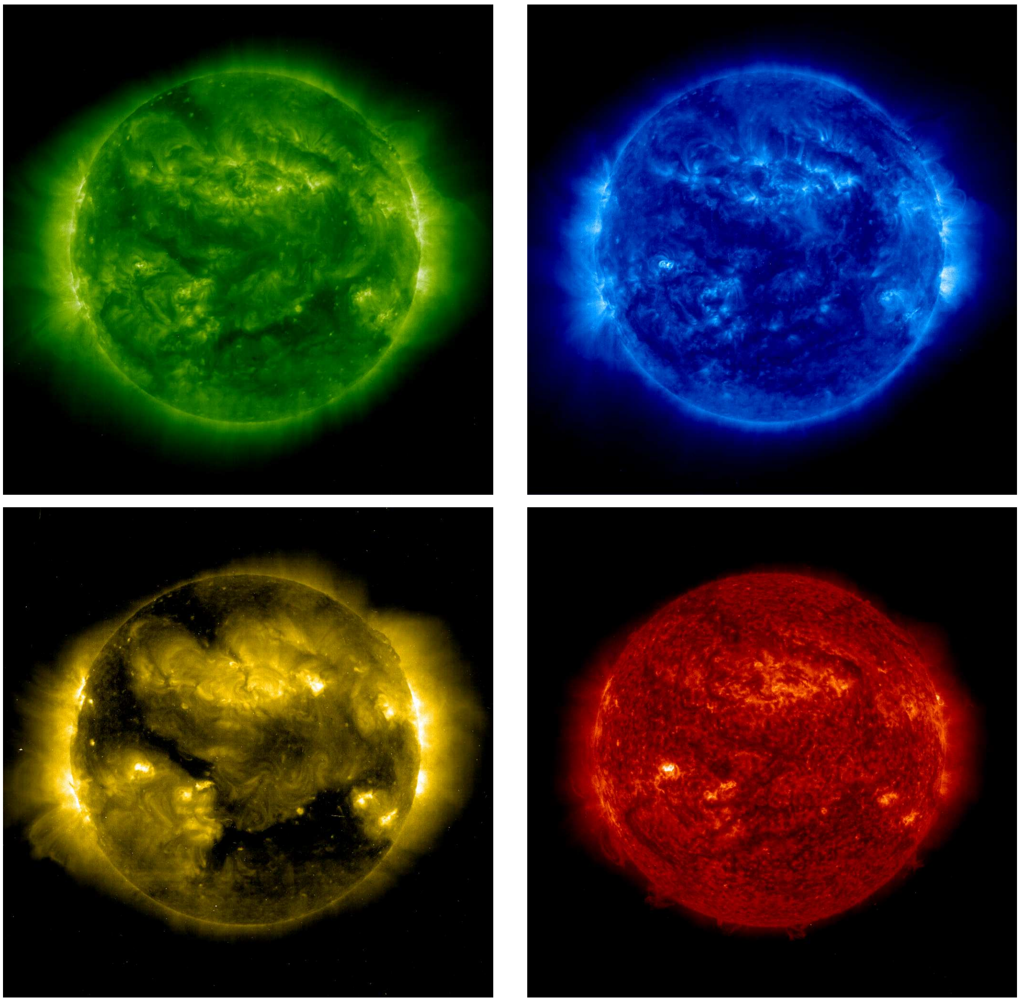

Figure 4: Image taken by the SOHO telescope in the four wavelengths of the EIT instrument on 2 June 2001. Upper left: 19.5 nm. Upper right: 17.1 nm. Lower left: 28.4 nm. Lower right: 30.4 nm showing the upper chromosphere and the transition region.

Wavelength	Ion	Peak Temperature	Observational Objective
304 Å	He II	8.0×10^4 K	chromospheric network; coronal holes
171 Å	Fe IX–X	1.3×10^6 K	corona/transition region boundary; structures inside coronal holes
195 Å	Fe XII	1.6×10^6 K	quiet corona outside coronal holes
284 Å	Fe XV	2.0×10^6 K	active regions

Figure 5: The EIT passbands and their scientific objectives, from Delaboudinière *et al.* [28].

impossible due to the amount of data to process. The four EUV channels of EIT are identified by the characteristic wavelength of the passband, see Figure 5.

The first three are coronal lines:

- 17.1 nm, FeIX/X emission line, formed at the peak temperature $T \simeq 1.3$ MK, by convention in blue color table, showing the corona, and the transition region boundary and structures inside coronal holes,

- 19.5 nm, FeXII emission line, formed at the peak temperature $T \simeq 1.6$ MK, in green color table, particularly adapted for observations of the quiet corona outside coronal holes,

- 28.4 nm, FeXV emission line, formed at the peak temperature $T \simeq 2.0$ MK, in yellow color table, exhibiting the hotter parts of active regions,

and one cooler line of the upper chromosphere and the transition region:

- 30.4 nm, HeII emission line, formed at the peak temperature $T \simeq 80000$ K, in the red color table, corresponding to the upper chromosphere and the chromospheric region, and where one observes the chromospheric network and the filaments as black features.

One important property of the three coronal lines is that they are optically thin. This means that no photon is re-absorbed by the plasma, and thus the flux of photons of each pixel is integrated along the line-of-sight, down to the opaque solar surface: the support of the emitting source of radiance is consequently not necessarily well located along the line-of-sight.

The EIT telescope provides images with a maximum size of 1024×1024 pixels. The pixel spatial resolution is 2.6 arcsec, which represents roughly 1800 km on the solar surface at disc centre. There are three main modes of synoptic observations: the "CME Watch", the shutterless mode and the 6 hour "synoptic'" mode. In the latter mode, one image in each wavelength is taken every six hours. The shutterless mode is

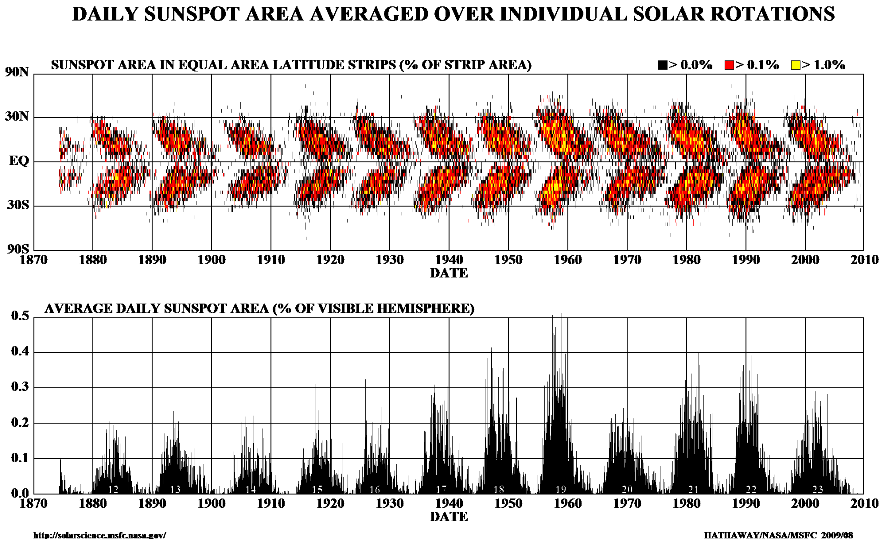

Figure 6: The butterfly diagram obtained by the estimation of the sunspot area index. From the website http://solarscience.msfc.nasa.gov. Courtesy of NASA Marshall Space Flight Center.

operated during high-cadence campaigns of observation with one image per minute; in this mode, the shutter is not used. The "CME Watch" is the regular observation mode, for which one image is taken normally at 19.5 nm every 12 minutes. The sequences used in this work comes from the "CME Watch" mode. It should be noted that in the "CME Watch" regular mode, the cadence is such that when the Sun rotates, the maximum displacement due to rigid rotation of a structure at Sun centre is about one pixel between two frames. An EIT archive is available at the Solar Influences Data Analysis Center (SIDC) of the Royal Observatory of Belgium (ROB).

TRACE

TRACE is a NASA Small Explorer (SMEX) mission to image the solar corona and transition region at high angular and temporal resolution. The TRACE investigation explores the dynamics and evolution of the solar atmosphere from the photosphere to the corona with high spatial and temporal resolution [44, 92]. Similarly to the EIT instrument, TRACE uses normal incidence multilayer optics to follow the evolution and dynamics of the solar atmosphere at selected temperatures over the range 6000K-10MK. The TRACE instrument comprises White Light (500.0 nm, broad), Lyman Alpha (121.6 nm, temperature range $1 - 3\ 10^3$ K), C IV 1550, UV Continuum (160.0 and 170.0 nm, broadband), 17.3 nm (transition region), 19.5, and 28.4 nm (coronal lines). It runs high-cadence campaigns of observations (1 minute cadence) in a narrower Field of View (FOV) than EIT, but at a better resolution (0.5 arcsec per pixel, meaning a pixel resolution of 350 km).

STEREO-SECCHI-EUVI

The STEREO mission is the third mission in NASA's Solar Terrestrial Probes program. It employs two nearly identical space-based observatories - one ahead of Earth in its orbit, the other trailing behind - to provide the first-ever stereoscopic (3D) measurements to study the Sun and the nature of the CMEs. The STEREO spacecraft is separating at a rate of about 45 degrees per year, thereby providing two distinct and unique approaches to understanding the key physics leading to CMEs. Early in the mission both STEREO spacecraft view the same features in the corona on a variety of scales. During the later part in the mission, STEREO provides unique perspectives of the CME process from widely separated viewpoints. Sun Earth Connection Coronal and Heliospheric Investigation (SECCHI) takes full advantage of these capabilities to improve dramatically on the existing knowledge of the eruptive process. Among the SECCHI instruments (see Figure 7), the Extreme UltraViolet Imager (EUVI) telescope imager observes the chromosphere and low corona in four different EUV emission lines similar to the EIT bandpasses. To meet its scientific objectives, the EUVI has a full Sun FOV extending to 1.5 solar radii and a good spatial resolution defined by 1.59 arcsec per pixel, to be compared with the resolution of 2.6 arcsec per pixel for EIT and 0.5 arcsec for TRACE. It also has the capability to image the corona at different temperatures, and the capability for fast image cadence. The EUVI is a small Cassegrain telescope with heritage from EIT and TRACE with detector providing higher sensitivity, resolution, and image cadence. The EUVI images show strong lossy compression effects due to high compression ratio achieved onboard.

Motions in Images of the Solar Atmosphere

EUV images of the solar atmosphere display many different motions, produced by variable sources of plasma emitting in the EUV wavelengths, from the large-scale solar differential rotation to smaller scale transient events such as loop motions and CME. Standard techniques for motion measurement include visual observations and manual extraction of motion, requiring the interaction with a human observer. As noted by Young and Gallagher [111], the measurements based on human visual system are inherently subjective and prone to error. Moreover, these techniques do not so far provide important properties of coronal features like velocity and lifetime. These quantities would be of greatest interest in order to better understand the dynamics in the lower corona. They do not provide statistical uncertainties and are not reproducible. The recent and great progress of instrumentation in solar space

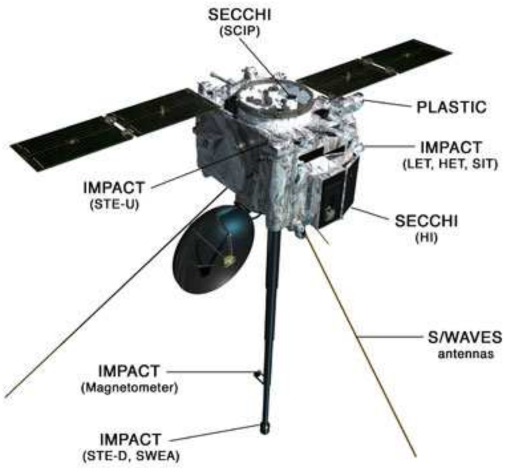

Figure 7: The STEREO spacecraft and its four instrument packages: SECCHI, SWAVES, IMPACT, and PLASTIC. Image Credit: APL.

missions has imposed the development of image processing techniques to enable fast and reproducible treatments of the increasing volume and flux of solar EUV images. First attempts to process an image archive was accomplished recently [49]. In order to quantify visual observations such as apparent motion of structures, there is a need to develop new efficient and adaptive tools such as motion analysis algorithms. Furthermore, using motion analysis is also a way to extract objects that are not well defined in single images, but that we are clearly identifying through visual observations of sequence of images. Extraction and tracking in an objective and automated way represents a scientific challenge for any coronal structure.

Modern image processing techniques are required to handle the data provided by the upcoming Solar Dynamics Observatory (SDO) mission, or the EIT archive that now covers completely the solar cycle 23 (from year 1996 to the current extended solar minimum 2008-2009). Unfortunately, image processing of solar EUV image sequences is difficult: the main problems stem from noise, the variations in source brightness, rapid and hence under-sampled topological changes, the lack of spatial resolution (spatial aliasing), and transparency. One of the main problem we have to cope with in coronal images is the intensity variations that are not caused by motion of the coronal features. These variations arise from the locally variable plasma, that is to say from solar activity itself, as well as from instrumental and observational noises. It results in large perturbations to the standard in motion estimation. Thus, we need to develop a motion analysis method robust to those variations and providing a confidence quantity to the computed parameters. We focus our attention on the study of motions and intensity variability in sequences of EUV images of the solar atmosphere, and our goal is to take up the challenge of image processing of the EUV images of the solar atmosphere.

Space weather services have motivated this work [*e.g.* 50], but the range of potential interests extends beyond early warnings of flares and CME onsets. It includes, for example, studies of bright points and filaments, differential rotation, coronal seismology (loop oscillation tracking and wave investigations), event detection (extreme outlying motions), etc.

Outline of the Thesis

In Chapter 1, we briefly present the dynamic events observed in the solar atmosphere. The source of light is spatially inhomogeneous and temporally variable. Several mechanisms explain this variability, but an important reason inherent to the solar atmospheric plasma is the variation of the physical parameters such as density and temperature of elementary volumes of coronal plasma as well as the transparency effects along the Line-Of-Sight (LOS). In addition to the activity of the solar cycle that has a duration of 11 years, we introduce the solar phenomena that will be of interest in this work: the solar rotation, of the order of 25 days, and the transient events such as the flares and the CMEs that occur irregularly and whose typical time scales are of the order of hours to days.

In Chapter 2, we introduce the main motion analysis techniques and how they have been applied to solar physics. Motion analysis is a complex image processing task that has been widely studied and for which there is no simple solution. In this chapter we particularly detail the concept of optical flow, an estimate of the projected 2D velocity field, as well as the main classes of algorithms that implement the estimation of motion.

In Chapter 3, the objective is the analysis of dynamic events that are observed in a succession of two images. Estimating both speed and Brightness Variation (BV) simultaneously is mathematically achievable, and physically meaningful since solar activity exhibits motion and intensity changes, such as brightening or flaring, and dimming effects. We present here a technique capable of producing velocity and brightness variation maps that addresses essentially all phenomena observed in sequence of images. The method is based on the Lucas-Kanade optical flow algorithm, that we use in its symmetric formulation, and extended to the estimation of BV. It is multiscale and regularized against aperture effects. We also present an error prediction system based on a quality index, and a calibration procedure.

In Chapter 4, the optical-flow algorithm is applied here to the estimation of dimming maps and brightening maps in SOHO-EIT images at all wavelengths (17.1 nm, 19.5 nm, 28.4 nm and 30.4 nm) in Chapter 4. We demonstrate the ability of our optical flow algorithm to interpret the difference image of a sequence of two EUV images as the sum of two components, one associated to motion and the second to brightness variation of the moving objects. Real EIT sequences are analyzed in terms of motion and brightness variations over the full solar image.

In Chapter 5, the objective is to build the correct tools to identify and track the main dynamic features in EUV sequences of images of the solar atmosphere. The tracking of features extends the two-frame motion estimation to larger displacements and longer-length sequences. The motion estimation is combined with a tracking algorithm in order to detect and analyze the loop oscillations in the coronal EUV images using sequence of TRACE images. The tracking algorithm is used to analyze the differential rotation over the solar cycle when applied to the EIT archive available at ROB-SIDC. This represents a new measurement of the solar differential rotation.

In Chapter 6, we apply on STEREO-SECCHI-EUVI images our algorithm to derive the 3D coordinates of the solar features observed in the 30.4 nm passband. We present our method of stereoscopic reconstruction using pairs of EUVI images provided by the two STEREO spacecrafts. We first establish in the heliocentric coordinate system the formula that provides, given the separation angle and a pre-processing step, the expected displacement between two pixels at the photospheric radius. We derive the stereoscopic reconstruction formula that gives the radius of solar features. In the sequence of 19 May 2007, the study of the altitude of an eruptive filament is achieved.

In Chapter 7, we use spatio-temporal techniques to integrate the temporal information of sequences longer than two images. A sequence of images form datacubes of dimension 2 in space and 1 in time (2D + T) equivalent to a 3D datacube. Its $(2+1)D$ continuous wavelet transform is used to represent the image datacube according to the following parameters: location in space and time, spatial scale, and velocity parameters (direction and velocity amplitude).

Chapter 1

Dynamic Events in EUV Observations of the Solar Atmosphere

Extreme Ultraviolet (EUV) images of the solar atmosphere display many different sorts of motions, produced by variable sources of plasma emitting in the EUV wavelengths. They reveal the dynamic nature of the external layers of the Sun, and the study of moving atmospheric elements can bring crucial information about the remaining unanswered questions in solar physics. The succession of images provide scenes extremely rich in events of primary importance that may help to elucidate the solar atmosphere. The concept of motion must be approached from different viewpoints and has been studied in physics, in applied mathematics, as well as in cognitive science; to each of them correspond specific methods of estimation. In the case of solar atmospheric observations in the EUV domain, estimating motion represents a challenge because of the properties of the images; indeed, in the solar atmospheric plasma, the source of light is spatially inhomogeneous and temporally variable. Several mechanisms explain this variability, but an important reason inherent to this plasma is the variability of its physical parameters such as density and temperature. In addition to the plasma variability, another important physical cause is the fact that the coronal plasma is optically thin, meaning that the photon flux received by the telescope detector is integrated along the Line-Of-Sight (LOS). Furthermore, the instrument passband is relatively narrow in wavelength, and thus in temperature passband, see Figure 1.3. Image processing of solar EUV images is made difficult, and in the particular case of image sequences, the main problem stems from the variations in source brightness. We summarize here these issues in these three statements:

- The coronal plasma is optically thin; therefore signal is integrated along the line-of-sight, and several coronal structures sometimes pile up. This will be dubbed the "transparency challenge".

- EUV solar telescopes use multilayer mirrors to observe within a wavelength passband, and to hence select useful emission lines and thereby their temperature regime. Temperature changes cause coronal features to get in or out a given passband, thus modulating their brightness. Typical values for the Transition Region and Coronal Explorer (TRACE) instruments can be found in [45], see Figure 1.1.

- The magnetized plasma can be very unstable and swift topological reconfigurations are frequent. The typical 12-minute nominal cadence of the EIT CME watch mode leads to temporal under-sampling (aliasing).

Yet, there is a need for a motion estimation technique, which disentangles motions from the possible brightness variations. Solar atmospheric events are dynamic, and are characterized by spatial and temporal scales; small-scale objects generally have faster motions and shorter lifetimes. Historically, analyzes of *Skylab* data have proven that the solar corona is fundamentally structured on a wide range of scales, and extremely dynamic. Vaiana and Rosner [102] noted that "*intensity fluctuations of coronal structures occur on virtually all observable spatial and temporal scales*". In order to analyze the phenomena observed in the EUV wavelengths, we present the physical phenomena associated to the dynamic events occurring in sequences of EUV images. We then introduce the main approaches of motion estimation, as well as some of the most recent related works applied to solar physics.

1.1 EUV Imaging of the Corona

Observing the corona in EUV spectral lines may be achieved either with spectroheliographs that can record images at a high spectral selectivity but only using rastering techniques, that cannot quickly build an image for mechanical reasons. From the analysis of spectral lines emitted in the photospheric layers one can derive the LOS velocity by estimating the Doppler shifts, and the magnetic field value along LOS by measuring the spread of the line triplets caused by the Zeeman effect. The splitting can not be measured in the corona because the coronal magnetic field is too weak to split strongly enough an EUV line emitted by the coronal plasma (see [81]). Because of this limitation, coronal magnetic field measurements can only be achieved through indirect measurements such as the techniques of coronal seismology, via the analysis of the loop oscillations that we will introduce in Chapter 5. Here we introduce the concepts of EUV imaging that will allow us to understand how the images of the instruments used in this work are formed.

Wavelength (Å)	Emission	Bandwidth (Å)	Temperature (K)
171	Fe IX/X	6.4	1.6–2.0×10^5
195	Fe XII/XXIV	6.5	5.0–20×10^5,
			1.1–2.6×10^7
284	Fe XV	10.7	1.25–4.0×10^6
1216	H I Ly α	84	1.0–3.0×10^4
1550	C IV	30	6.0–25×10^4
1600	UV Cont, C I, Fe II	275	4.0–10×10^3
1700	Continuum	200	4.0–10×10^3
5000	White Light	broad	4.0–6.4×10^3

Figure 1.1: The temperature response of the TRACE instrument, from Handy *et al.* [45].

1.1.1 Formation of an EUV Bandpass Image

The measured radiation by the coronal plasma depends on the instrument response as well as on the physical parameters describing the plasma. To simplify the description of the plasma, one defines the Differential Emission Measure (DEM) function $\phi(T)$, that describes the amount of plasma along the LOS at a given temperature. The DEM $\phi(T)$ is defined such that $\phi dT = N^2 dV$ where N is the electron density. The Emission Measure (EM) is defined by

$$EM = \int_{\mathrm{LOS}} N^2\, dV \ .$$

One can express the intensity in the spectral line λ_i as an integral over the temperature T:

$$I(x,t,\lambda_i) = \int K_{\lambda_i}(T)\phi(T,x(t),t)dT \ [\mathrm{erg\ cm^{-2}\ s^{-1}\ sr^{-1}}] \tag{1.1}$$

where we assume that $K_{\lambda_i}(T) = A(Z)G_i(T,N)$ does not depend on the pixel location x (nor on time t) and where A is the elemental abundance, ϕ is the DEM in temperature, N is the electron density, T is the electron temperature, G is the "contribution function" that contains all of the relevant atomic physics coefficients, including constant factors. The function G depends on electron density and temperature.

To simplify the problem, on can assume that given the wavelength, the DEM function ϕ only varies with time t. In the case of multi-structure plasma, where several different plasma elements such as loops are situated along the LOS, all contribution of the emitting plasma are summed up in the integral term, which may lead to a broadening of the spectral line profile because of cumulative Doppler effects.

1.1.2 Transparency and Optical Thickness

The transparency properties of the plasma depend on the absorption coefficient of the given line. In the case of the Extreme ultraviolet Imaging Telescope (EIT) instrument, the three coronal channels (17.1, 19.5, and 28.4 nm) can be considered as optically thin. The upper chromosphere/transition region channel around the emission line 30.4 nm is considered mostly optically thick ondisc.

1.1.3 Instrument Responses

The response of the instrument to the emitted signal is the result of the convolution over wavelength of the density of the emitting plasma by the instrument response. One can write the count rate as the result of the convolution over wavelength of the density of the plasma emitted intensity by the instrument response

$$\mathrm{CR} = \iint R(\lambda)\, G(n, T, \lambda)\, \phi(T)\, d\lambda dT \ , \tag{1.2}$$

where G is the theoretical plasma emissivity in photons $\mathrm{cm}^6\ \mathrm{s}^{-1}\ \mathrm{sr}^{-1}\ \mathrm{A}^{-1}$, ϕ is the DEM, and R is an effective area of the instrument. The digital output signal received by the detector is counted in the non physical unit DN s^{-1} pixel^{-1}, modeled for EIT by [30].

The Count Rate (CR) depends on the instrument function R, which regroups the contributions of the geometric area and the reflectance of the telescope mirror, the entrance and the focal plane filter transmissions and the Charge-Coupled Device (CCD) quantum efficiency. In the case of the EUV imagers, the width of the response function determines the selectivity of the instrument; typical values of width can be found in Figure 1.1. It is usually too large to select only one emission line, and includes more than one emission line so that the count rate is a combination of signals emitted at different plasma environments and temperature.

Figures 1.3 and 1.4 respectively show the instrument responses of the EIT and the Extreme UltraViolet Imager (EUVI) instruments, for a given emission measure. The typical EIT emission measures of the solar regions are given in Figure 7.5. The temperature bandpasses are not narrow enough to consider that an image is formed at single temperature. Rather, one can think of the EUV image of the Sun as the peak of a temperature distribution, but one has to remember that wide-range temperature variations (or density variation at a given temperature range) may have an impact on the count rate CR through the bandpass of the contribution function.

Feature	Temp. (MK)	Em. meas. (cm^{-3})	α	Exp. (s)	171 Å	195 Å	284 Å
					Signal (DN) in one pixel		
Coronal hole	1.3	2×10^{42}	1	20.	70	30	< 1
X-ray bright point	1.8	7×10^{43}	1	10.	179	320	10
Coronal loop	2.1	1×10^{43}	10	60.	4	8	< 1
Active region	2.5	3×10^{45}	144	60.	40	41	7
Impulsive C flare	12.0	5×10^{48}	10	0.5	1200	5032	24

Figure 1.2: The typical EIT intensities depending on observed solar region. From Delaboudinière *et al.* [28].

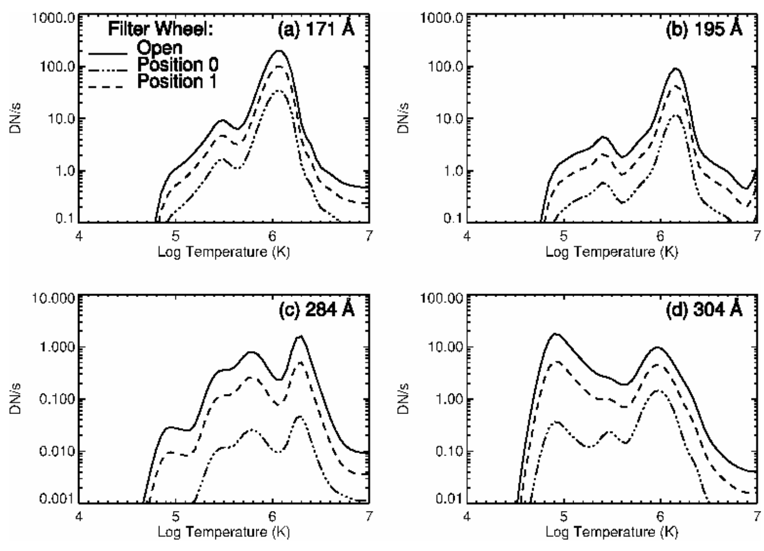

Figure 1.3: The EIT imager intensities for a synthesized solar atmospheric region ($EM = 10^{44}\mathrm{cm}^{-3}$). Each curve represents the count rate of a given bandpass as a function of the temperature of the emitting plasma volume. From Delaboudinière *et al.* [28].

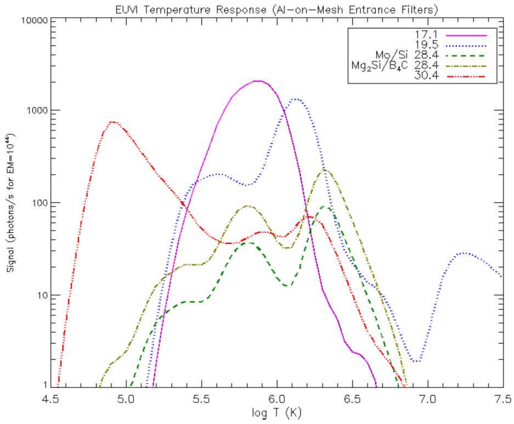

Figure 1.4: The STEREO telescope response for a synthesized solar atmospheric region ($EM = 10^{42}\text{cm}^{-3}$). Each curve represents the count rate of a given bandpass as a function of the temperature of the emitting plasma volume. Courtesy of the STEREO team.

1.2 Description of the Solar Atmospheric Motions and Their Observations

The first observations of dynamic solar events were achieved during the 20th century. One can classify the solar atmospheric motions into global and local motions. Global motions are dominated by the differential rotation, while many kind of local small-scale motions exist (loop oscillation, proper motion of bright-point, etc). Variations of brightness such as dimmings exist at all observable spatial scales.

1.2.1 The Three Solar Regions

The atmosphere of the Sun is categorized into three distinct regions: the Active Region (AR), the Quiet Sun (QS), and the Coronal Hole (CH). An AR is a region of intense magnetic activity, that overlies the suns, due to magnetic field emerging from inside the Sun. It contains portions at various temperatures, from 10^4 to 10^6 K. It is hotter and denser than quiet-sun regions. The signal intensity, or photon flux, as recorded by the EIT instrument, related to the radiance, is higher on ARs where the plasma material is confined, tracing the closed magnetic field lines. Active regions can last for several weeks up to months.

A CH is a low-density and “cold” region found at the solar poles during solar minimum, with open magnetic field lines. Coronal holes are the source of the fast solar wind, and can be equatorial during solar maximum periods.

The set of QS regions, covering the solar network outside AR and CH, is the third part of the solar disc, with dimmer emission, somewhat enhanced along the network and on bright points.

1.2.2 Dynamic Features of the Solar Atmosphere

We give here a non-exhaustive list of the solar phenomena visible in the three regions mentioned above. Solar features and phenomena are defined by the wavelength passband of the instruments and their definitions are mostly observational.

The Chromospheric Network

The chromospheric network is a web-like pattern seen with difficulties in the emissions of the red line of hydrogen (H_{α}) and the ultraviolet line of calcium. The network outlines the supergranule cells and is due to the presence of bundles of magnetic field lines that are concentrated there by the horizontal and outward motions. The chromospheric network, its size and multiscale dimension have been analyzed in the 30.4 nm channel of EIT by [29]. The typical size of the chromospheric network is 20-30 Mm.

Prominences

The prominences - or filaments when observed on the solar disc - are cold high-density regions that absorb the EUV photon flux, thus appearing as a dark volumes in EUV images. A prominence is an object in the corona that is denser and cooler than its surroundings. Long-lived (days to months) prominences seen away from active regions and large sunspots are referred to as quiescent prominences. Filaments are typically observed in absorption in the Lyman$-\alpha$ channels. Their height may vary from 1 to 10 percent of the solar radius $R_{\odot}$. Rapidly changing prominences are named active or eruptive prominences. They break away from the solar atmosphere and being part of a Coronal Mass Ejection (CME) (see Figure 1.5). Both filaments and prominences can remain in a quiet or quiescent state during several rotations. However, as the magnetic loops that support them slowly change, filaments and prominences can erupt and rise off of the Sun over the course of a few minutes or hours. Their sudden disappearance within few hours is called a “disparition brusque”. There are two possible configurations for the prominence as shown in Figure 1.6. Filippov and Den [34] have proposed a way to estimating critical heights at which the prominence is theoretically unstable and is more likely to erupt. In the coronal lines and in the HeII 30.4 nm bandpass, prominences look dark because they absorb the light; but they look bright in HeII offdisc, and are observed in emission as illustrated in Figure 1.5.

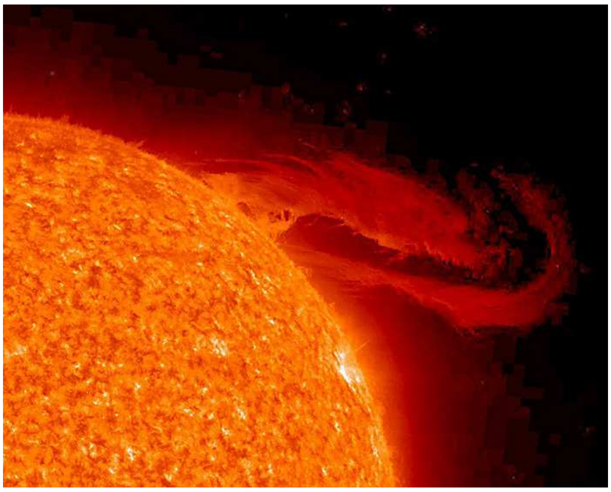

Figure 1.5: On September 29, 2008, an eruptive solar prominence lifted away from the Sun's surface and observed by the STEREO spacecraft in the 30.4 nm bandpass. Courtesy of the STEREO team.

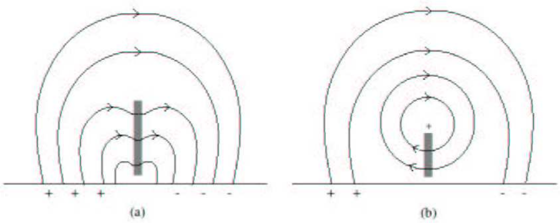

Figure 1.6: Two magnetic field models to support a prominence: (a) Kippenhahn-Schlüter model; (b) Kuperus-Raadu model. The figures show the field lines projected perpendicularly to the long axis of a prominence (shaded region).

Spicules and Fibrils

Spicules are cylindrical objects with a diameter of about 1000 km reaching from the low chromosphere 6000 to 10000 km into the corona. Their lifetime is about 5 to 10 min and the whole spicule shows an upward motion up to 30 km s^{-1}. After their ascent many spicules diffuse and fade out, while others are seen to descend, seemingly following in reverse the path of ascent. Much of the dynamics in the magnetized regions associated with the magnetic network and plage is dominated by these short-lived, jet-like features. A whole range of names have been applied to describe these chromospheric features, they are observed in Hα as thin, elongated features that reach heights of on average 5-9 Mm during their lifetimes of 3-15 minutes [9]. Their widths (0.2-1 Mm) and dynamics have, until recently, been very close to the resolution limits of observations. Fibrils are long thin dark threads visible in Hα on the disc at the edge of plages and near the edge of sunspot penumbra [65]. According to [24], fibrils are short-lived jet-like features. At the quiet-sun limb, they correspond to spicules.

Helmet Streamers

Helmet streamers are large cap-like coronal structures with long pointed peaks that usually overlie sunspots and active regions. Usually a prominence lies at the base of these structures. Helmet streamers are formed by a network of magnetic loops that connect the sunspots in active regions and supports the prominence material above the solar surface. The closed magnetic field lines trap the plasma to form these relatively dense structures. The pointed peaks are formed by the action of the solar wind blowing away from the Sun in the spaces between the streamers.

Polar Plumes

Polar plumes are long thin high-latitude streamers that project outward from the Sun's North and South poles. We often find bright areas at the footpoints of these features that are associated with small magnetic regions on the solar surface. These structures are associated with the "open" magnetic field lines at the Sun's poles. The plumes are formed by the action of the solar wind in much the same way as the peaks on the helmet streamers.

Coronal Loops

The solar corona is fundamentally structured on a wide range of scales, and its basic building block is a closed magnetic structure named coronal loop. They are usually visible located in active regions in the coronal bandpasses, near the sunspot groups where there exist strong magnetic fields. The bipolar (or multipolar) nature of active regions implies that the plasma is made up of closed magnetic field lines, namely the loops. Magnetic activity, including magnetic flux emergence, flux cancelation, and magnetic reconfiguration and reconnections, which are one mechanism of plasma heating and other phenomena such as waves, flares, and CMEs. A consequence of chromospheric heating is upflow into coronal loops, which gives active regions the characteristic appearance of numerous coronal loops which are hotter and denser than the background corona, producing bright emission in soft X-rays and EUV wavelengths. A closed field line does not constitute a coronal loop by itself; a loop is a closed flux that is filled with plasma. Coronal loops are exceptions in the solar atmosphere because the majority of closed flux structures are essentially empty. This means the mechanism that heats the corona and injects chromospheric plasma into the closed magnetic flux is localised. The explanation for plasma filling, dynamic flows and coronal heating remains unknown. The mechanisms must be stable enough to continue to feed the corona with chromospheric plasma and powerful enough to accelerate and therefore heat the plasma from 6000 K to well over 1 MK over the thin transition region. Anchored to the photosphere, coronal loops are fed by chromospheric plasma, pass through the transition region and are observed at coronal temperatures. Post-flare loops [37] are phenomena of short lifetime that are visible after flares, as shown in Figure 1.7.

X-ray and EUV Bright Points

EUV bright points are found over the whole solar disc. The typical size of these coronal features is smaller than 60 arcsec, their lifetime is less than two days and characterized with enhanced emission. A small fraction of soft X-ray bright points (which are the sites of microflares) are associated with an emerging bipole, while a much larger fraction was associated with magnetic cancelation features (Harvey et al. 1994).

Cosmic Ray Hits

Cosmic rays are high energy charged particles, originating either in outer space (such as Supernovae or stellar flares) or in solar flares. They hit directly the silicon in the CCD sensor of the telescope. They are randomly distributed over the image, and hence are present at a given location in one frame only; they are not imaged by the telescope. We will refer to such a feature as a Cosmic Ray Hit (CRH).

1.2.3 Transient Solar Events

Among all the different events that we can observe in the corona, there are two special types: flares and CME.

Flares

A flare is a dramatic heating of a solar region (up to several 10^7 K) with a high radiative energy release, that is very localized and causes bursts of x-ray, γ, α and neutrons high energetic particles. They appear as dramatic local brightening of the corona within active region. A solar flare can generate a burst of particle acceleration, heating of plasma to tens of millions of degrees, and are often associated with eruption of large amounts of solar mass (Coronal Mass Ejection). Flares are believed to result from the abrupt release of the energy stored in magnetic fields in the zone around sunspots.

There is a lot of evidence that chromospheric reconnection with magnetic flux cancelation is the most likely mechanism to explain chromospheric variabilities (UV explosive events, H upflows, spicules, and soft X-ray brightenings), but this mechanism is probably not the primary driver for larger flares [4]. Contrary to small and compact flares, largest flares show features such as post-flare loops (see Figure 1.7)

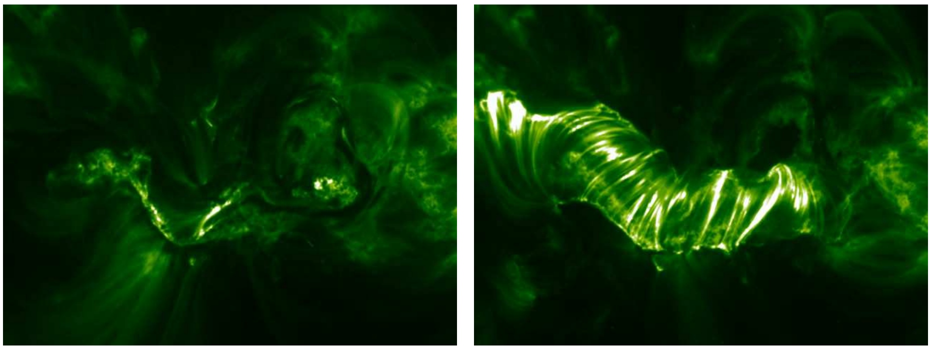

(a) Before the flare. (b) After the flare.

Figure 1.7: Post-flare loops observed after a solar flare, and captured by the TRACE spacecraft in the 19.5 nm channel. Courtesy of NASA/Lockheed Martin Solar and Astrophysics Laboratory.

and are named “two-ribbon flares” because of the existence of two ribbons usually observed in the Hα and the 30.4 nm passbands. The two narrow ribbons are located on each side of the Polarity Inversion Line (PIL) which represents the line where the LOS component of the magnetic field reverses. The ribbons are the footpoints of the bright coronal loop arcades. A possible explanation of this phenomenon is a “disparition brusque” of an active region filament located along the magnetic neutral line before it lifts off, see Figure 1.8. We will discuss this model in our stereoscopic reconstruction method (see Chapter 6).

There are two types of flares: impulsive and gradual. Impulsive flares accelerate mostly electrons, with some protons. They last minutes or hours and the majority appear near the solar equator. Impulsive flares occur at a rate of about 1000 per year during solar maximum. Gradual flares accelerate electrons, protons, and heavy ions to near the speed of light, and the events tend to last for days. They occur mainly near the poles of the Sun and happen about 100 times per year. This acceleration of solar flare particles to extremely high energies involves all the different elements in the solar atmosphere. Ions of elements such as carbon, nitrogen, oxygen, neon, magnesium, silicon, and iron, excited in this way, end up in solar cosmic rays, also called Solar Energetic Particles (SEP).

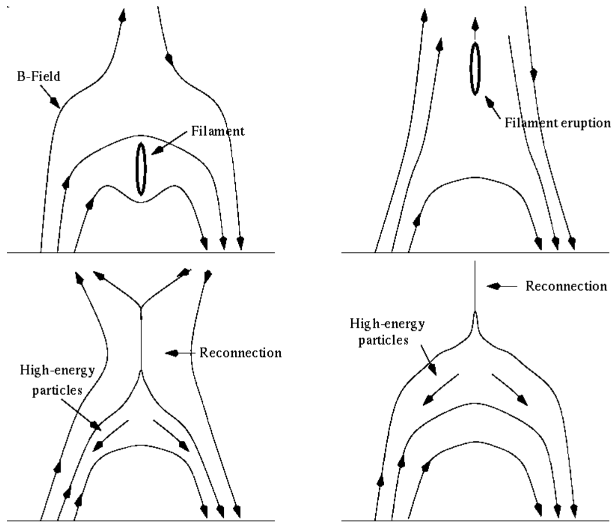

Figure 1.8: A basic model of filament eruption associated to a two-ribbon solar flare. Courtesy of Scrijver et al. 2001.

Coronal Mass Ejections (CMEs)

A CME is a transient event with ejection of plasma material into the heliosphere, i.e. away from the Sun. They are very well seen in LASCO coronagraphs onboard Solar and Heliospheric Observatory (SOHO). In EUV images, such as in the 19.5 nm bandpass, the CME ondisc signature appears as a dimming of intensity or as transient coronal holes. In the low corona, CME onset signatures include filament eruptions, waves, loop openings, post-eruption arcades observed in the EUV, and sigmoid-to-arcade restructuring in soft X-rays [53]. The morphology of a CME can vary: balloon-shaped bursts, loop-like structure, or more irregular structure; all of them rise above the solar corona and expand as they climb. In recent studies, the favored geometry is a three-dimensional helical flux ropes.

The super-heated electrons from CMEs move along the magnetic field lines faster than the solar wind can flow. Rearrangement of the magnetic field, and solar flares may result in the formation of a shock that accelerates particles ahead of the CME loop. Each CME releases up to 100×10^9 kg of this material, and the speed of the ejection can reach 1000 km s^{-1}. Solar flares and CMEs are currently the biggest sudden energy release in our solar system. They can trigger major disturbances in Earth's magnetosphere, known as geomagnetic storms and whose prediction is one of the topic of space weather.

Filament Eruptions

A filament or prominence may undergo sudden disappearance, or "disparition brusque" in French. It is a consequence of an instability, with subsequent eruption into to corona and interplanetary space, often accompanied by a flare or coronal mass ejection (see *e.g.* Figure 1.8). Sometimes, such an eruption "'fails" and the prominence material does not erupt properly.

1.2.4 The Differential Rotation

The Sun is a non-solid object that rotates around itself in 25 to 30 days. The solar rotation is *differential*, from its interior above the tachocline and convective layers up to the external layers of its atmosphere. The rotation rate varies as a function of latitude and radius within the Sun. In solar atmospheric images, this phenomenon has been widely observed and analyzed, but mostly at the photospheric level. In EUV observations, the model used for the differential rotation is the one used at the solar photospheric surface. First direct measurements of the differential rotation of sunspots as they cross the solar disc were achieved in 1951 by Newton and Nunn [73]. In the solar atmosphere, this rotation is such that the angular speed is greater at the equator than at the poles.

Rotation and Solar Dynamo The differential rotation is a key element in the current models of solar dynamo. It is widely believed that the Sun's magnetic field is generated by a magnetic dynamo within the Sun. The fact that the Sun's magnetic field changes dramatically over the course of just a few years, and that it changes in a cyclical manner indicates that the magnetic field continues to be generated within the Sun.

We observe a variety of flows on the Sun's surface and within its interior. Nearly all of these flows may contribute in one way or another to the production of the Sun's magnetic field. Magnetic fields within the Sun are stretched out and wound around the Sun by differential rotation: this is called the omega-effect (omega for rotation). The solar differential rotation with latitude can take a north-south oriented magnetic field line and wrap it once around the Sun in about 8 months. The solar rotation then twists the magnetic field lines: this is called the alpha-effect. Early models of the solar dynamo assumed that the twisting is produced by the effects of the solar rotation on very large convective flows that carry heat to the Sun's surface. One problem with this scenario is that the expected twisting is too large and it produces magnetic cycles that are only a couple years in length. More recent dynamo models assume that the twisting is due to the effect of the Sun's rotation on the rising "tubes" of magnetic field from deep within the Sun. The twist produced by the alpha effect makes sunspot groups that obey Joy's law (tilt of sunspot groups) and also makes the magnetic field reverse from one sunspot cycle to the next (Hale's law), see Golub and Pasachoff [43] or Foukal [37].

Today the Sun's magnetic field is supposedly being produced in the interface layer between the radiative zone and the convection zone: the tachocline. This interface layer is also a place where we find rapid changes in rotation rate as we look inward or outward across it. The flow of material along meridian lines from the equator toward the poles at the surface and from the poles to the equator deep inside - must also play an important role in the Sun's magnetic dynamo. This rate of flow is very similar to that of the sunspot activity bands seen in the sunspot butterfly diagram. The magnetic butterfly diagram also shows the weak surface fields being carried toward the poles by the flow at the surface.

A successful model for the solar dynamo must explain several observations: the 11-year period of the sunspot cycle, the equator-ward drift of the active latitude as seen in the butterfly diagram, the Hale's polarity law and the magnetic cycle, the observed tilt of sunspot groups, and the reversal of the polar magnetic fields near the time of cycle maximum.

Differential Rotation Measurements The differential rotation is usually modeled [16] using the law [73]

$$\omega(b) = A + B \sin^2 b \ , \tag{1.3}$$

where ω is the rotation rate and b is the solar latitude. Later, Howard and Harvey [52] proposed a refined model of differential rotation given by

$$\omega(b) = A + B \sin^2 b + C \sin^4 b \ . \tag{1.4}$$

In the latter model, the uncertainty on the coefficients B and C are in fact not independent. Figures 1.9 and 1.10 both show measurements of the differential rotation in various solar external zones of its atmosphere. From [108], as illustrated in Figure 1.9a, one can already conclude that different methods applied on solar structures provide quite different differential rotation coefficients.

The solar internal rotation is studied below the surface and is supposed to be rigid from the centre to the tachocline, and start to be differential from the base of the convection zone; at the photospheric level, as well as in the solar atmosphere (chromosphere, transition region, and in the corona), the rotation is differential at the notable exception of the coronal holes which rotate rigidly. In the solar atmosphere, the differential rotation has been studied by several authors. In the coronal EUV channels of the EIT instrument, Brajša *et al.* [15] have analyzed the rotation of the coronal bright points.

1.2.5 Tracking of Solar Dynamic Features

The tracking of solar features and motion measurements inform quantitatively solar physicists about dynamic events occurring in the solar atmosphere. We here give a non-exhaustive list of solar features and the expected scientific results the tracking may bring. Among them, we may cite the study of spicules [24], the eruption of prominences, the study of EIT waves [82], of EUV bright points [15]. It also

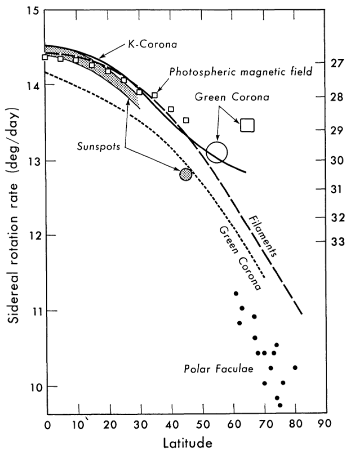

(a) From Wilcox and Howard [108].

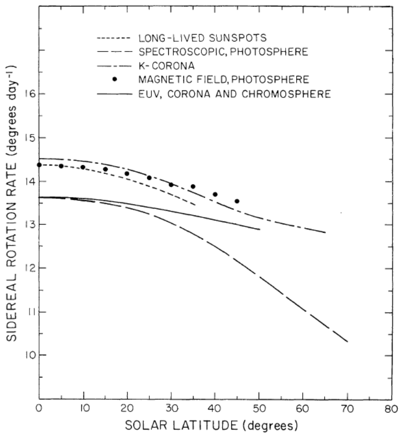

(b) From Henze and Dupree [47].

Figure 1.9: Measurement of differential rotation for different type of tracers including sunspots, filaments, and polar faculae.

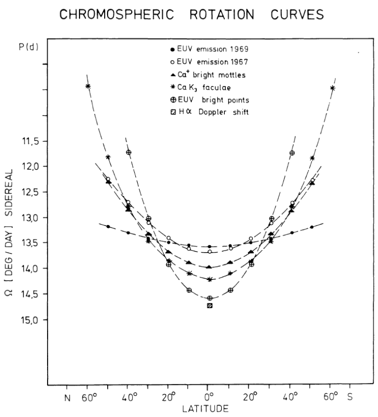

(a) A comparable study from Schroeter [94].

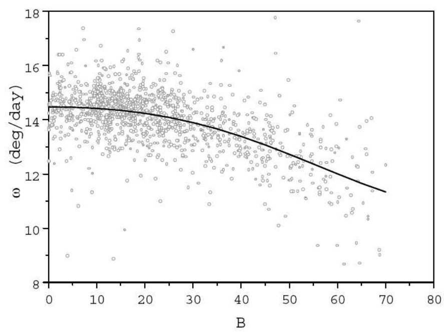

(b) The rotation $\omega(B)$ of EUV bright points as studied by Vršnak *et al.* [106].

Figure 1.10: Measurement of differential rotation. Several features and their differential rotations including bright points are compared, and the rotation of bright points alone is shown in the right figure.

encompasses the coronal loop oscillations and waves, as well as the propagating disturbances along loops with moving nodes and upward flows from loop footpoints), that are most probably slow-mode Magnetohydrodynamics (MHD) waves. Important oscillating events are coronal transverse oscillations which consist in lateral displacements of the loop plasma and we will detail in Chapter 6 an analysis of one case similar to [104].

Motions in Quiet Sun and Coronal Hole

In quiet sun regions, no significant flow speeds were found [46] or only small ones [20]. But observations show emergence of bright points and their proper motions, as well as Point-like Structures (PLS) with independent motions. The rotation velocity of X- and EUV- bright points has been studied by [15–18]. Coronal holes are known to rotate rigidly, but their motion is mainly defined by their border.

Active Region and Magnetic Extrapolation

In Figure 1.11, an AR with beta-gamma magnetic configuration is modeled by potential extrapolation and the magnetic field lines are superimposed on top of the original image as observed in the 17.1 nm TRACE channel. One can notice that in this example, the magnetic field potential extrapolation does not exactly match the active region loops. When the magnetic pressure is much higher than the thermodynamic pressure, the coronal loops may be assumed to trace the magnetic field. The frozen-in theorem imposes that the plasma material is restricted to move along the magnetic field lines; the magnetic field is displaced by the motion of its footpoints at the photospheric level. Unfortunately, in order to track the coronal loop structures, one cannot use the magnetic extrapolation because it is unreliable and the coronal loops that trace the apparent coronal field lines are extremely difficult to extract. This is one of the reasons for which advanced methods of motion analysis are required to analyze dynamical events in AR.

Flows and Oscillations in Coronal Loops

Different sorts of loop motions are observable in coronal EUV observations. In addition to the solar differential rotation, loop motions include oscillations and wave motions. Apparent flows in active regions can also be measured by feature tracking. Loop oscillations, likely to be excited by filament destabilization or flares, have been well observed : some recent observations show bi-directional or counter-streaming flows [84], or highly-fragmented downflows in catastrophically cooling loops, also called coronal rain [36, 91]. When speaking of the observed MHD waves, one traditionally distinguishes between oscillations that are the standing waves with fixed nodes, while propagating waves have moving nodes. One important observational

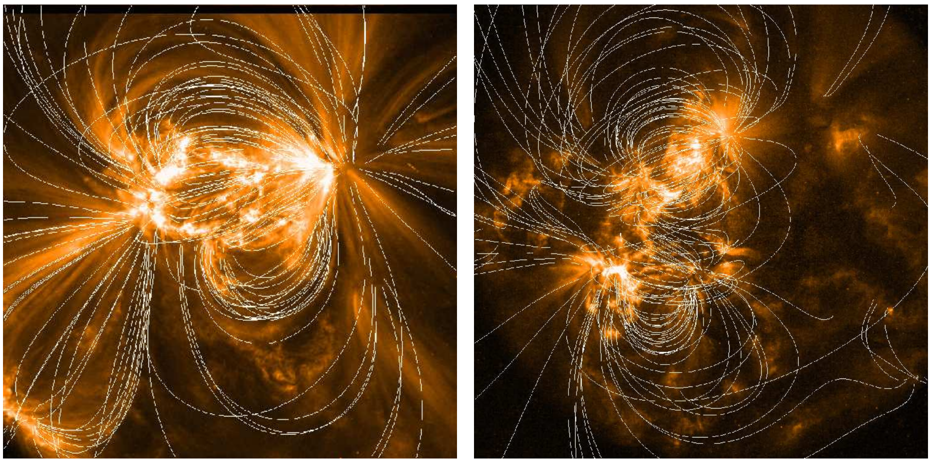

(a) 25/10/1999. (b) 07/08/2003.

Figure 1.11: A TRACE active region, and a superimposed potential field extrapolation computed using the Potential Field Source Surface Model (PFSS). Courtesy of the TRACE team.

discovery was the magneto-acoustic oscillations of the fast kink mode in EUV wavelengths with TRACE [5, 93]. They are usually observed as oscillatory motions transverse to the loop. Their period, damping time and their amplitudes are of particular importance for the purposes of coronal seismology. We will present our method for detection of such loop oscillations in Chapter 5. Acoustic waves propagating along coronal loops were probably first noticed in EUV images of EIT observations. Significant flow speeds were discovered in active region loops mainly with Coronal Diagnostic Spectrometer (CDS) [20], but also with Solar Ultraviolet Measurements of Emitted Radiation (SUMER) [110] and with TRACE [109]. Is is likely that flows exist in the majority of active region loops, but their measurement is difficult with every existing method: if spectrographs (such as CDS or SUMER) are used, then the Doppler shift can only be measured along the line-of-sight and may largely cancel out in images with insufficient spatial resolution, and if high-resolution imaging such as TRACE is used, then only inhomogeneities in flowing plasmas can be tracked, while laminar flows appear indifferent to static loops. In the following we describe some of the few existing coronal flow measurements [4].

During reconnection processes, the loops interact; in reconnection models, the inflow velocity relates to the reconnection rate, and some authors have measured this inflow velocity [74]. Furthermore, when CME events occur, some coronal loop in active regions opens during a very short amount of time [112]: this motion is one of the signatures of the CME onset in solar disc EUV observations which represent a motion clearly different from the global differential rotation.

1.3 Variability in the Solar Atmosphere

By variability, we here mean the variability of observed intensity of solar objects in the EUV images. Transient loop brightenings and small "flare-like" events in the solar atmosphere are important variable events occurring in the solar atmosphere and observable in EUV images. Transient brightenings have been studied in [11–13]: they find an unexpectedly large number of small-scale brightenings in EUV images of the solar atmosphere. The thousands of brightenings observed by EIT in the transition region include many that are similar to "blinkers" observed with spectrographs. The sources of variability of the EUV signal, as well as the origins of the signal variations, include:

- intrapixel variations: waves (variations of velocity, magnetic field, density), enhancements of density and temperature at small time scales,
- large-scale effects (observed): dimmings and CME onsets, brightenings, oscillations, flares and flare-like events.

In EUV observations, one usually observes that the variation of the intensity is correlated with the intensity level so that the variance of the intensity follows a power law of the intensity. The combination of sources of intensity variability, that are accompanied by detector noises in the EUV images, justifies the need for an algorithm that can disentangle in difference images the signal part that is due to motion of solar structures from the pure variation of intensity listed above.

Chapter 2

Methods of Motion Analysis

Motion analysis is a complex image processing task that has been widely studied and for which there is no simple solution. In this chapter we introduce the concept of optical flow, an estimate of the projected 2D velocity field, as well as the main classes of algorithms that implement the computation of the optical flow. A classical review of optical flow algorithms can be found in [8].

2.1 The Perception of Motion

For human perception, motion is a primary sensory quality. Early studies showed that motion perception does not depend on separate spatial displacements and temporal intervals. It has been demonstrated that human motion perception does not require the prior computation of spatial displacement or temporal intervals. Nevertheless, at the computer numerical level, one has to measure displacements over discrete time intervals. In both cases, one estimates an apparent velocity field that is a projection of the real motion field. Unfortunately, there exist visual effects that may prevent the recovery of the true motion vectors and that can be mathematically explained.

2.1.1 Apparent Motion

Apparent motion is really best thought of as a projected and sampled motion. An image on a computer screen is made up of discrete pixels, which are samples of a continuous signal. The experience of smooth continuous motion can be understood in the same way. Continuous motion is sampled in the form of discrete frames. At high cadence, the individual frames cannot be resolved by the eye, and the sampled motion is indistinguishable from continuous motion. Introducing the concept of *apparent motion* immediately states a fundamental limitation of imaging data: images are projections of 3D features in the sky into the 2D plane. This problem of perspective in the mostly transparent corona corresponds not only to geometrical distortions of the velocity fields but also to ambiguities, if more than one "feature" are superimposed on the Line-Of-Sight (LOS). It also generates occlusions where opaque objects, such as prominences or the solar disc itself, are considered. However, the issue of apparent motion goes beyond projection effects alone: motion tracking algorithms, as well as human observers, can trace only intensity patterns but not actual plasma elements. Without spectroscopic information, propagating brightness patterns are *a priori* indistinguishable from actual motions [23]. Fortunately, at the same time, this ambiguity gives access to a range of phenomena able to bring physical insights of their own [*e.g.* 26, 59].

2.1.2 The Blank Wall

As illustrated in Figure 2.1, the zone in the centre of the square does not contain an adequate texture to track. This is the blank wall effect, when no texture is present in the region where motion is estimated. Mathematically, it means that there is no possibility to retrieve any component of the solution to the motion estimation problem from the given data. In practice, there is always some texture in the image, and even when the Signal-to-Noise Ratio (SNR) is low, the presence of noise makes that in the case of solar images the pure blank wall effect is never met. In the worst case of low SNR, the blank wall effect makes the solution extremely sensitive to noise perturbation and the motion estimation then has a small robustness.

2.1.3 Aperture Effect

The aperture effect may be seen as an illusion effect in visual perception. As noted by Hildreth [48], the motion of a homogeneous contour is locally ambiguous (see Figure 2.1). This is so because a motion sensor has a finite receptive field: it "looks" at the world through something like an aperture. In mathematical terms, when the aperture effect occurs along an elongated object, the solution of the motion inverse problem is not unique and consequently, the determination of the 2D motion field is an ill-posed problem. In practice, in the case of optical flow, one ends up with one equation for two unknowns per pixel. In our three-parameter space consisting in motion components and the brightness variation, the aperture effect can extend to the ambiguity between motion and Brightness Variation (BV). In Figure 3.2, one can see that the evolution of a 1D signal may be interpreted as a combination of motion and brightness variation.

2.2 Motion Estimation as an Inverse Problem

In 1923 Hadamard defined the conditions needed for an inverse problem to be *well posed*:

- a solution exists,

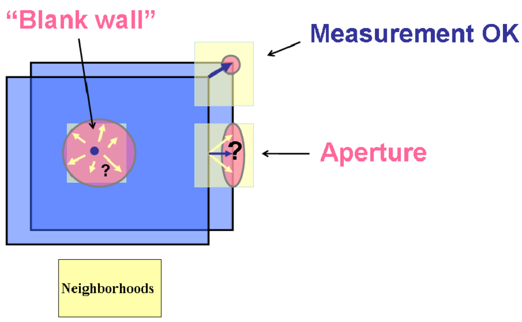

Figure 2.1: Illustration of the "blank wall" effect and the "aperture effect". When trying to track the blue square from the first to the second position, within a local neighbourhood (yellow), the blank wall effect occurs since there is no texture at the centre of the blue square. At the edge of the square, only the normal component of the motion: this is the aperture effect.

- the solution is unique,
- the solution depends continuously on the data.

Motion estimation is an ill-posed problem since one of the previous conditions can be invalid: the motion can be undefined (no solution exists, *e.g.* in case of occlusion), there can be several possible solutions (aperture problem, along elongated objects), and the solution can be discontinuous which may lead to non-robust estimations. Verri and Poggio [103] stated that optical flow is known as an "ill-posed problem" and its estimation is "intrinsically unreliable".

2.3 Main Approaches to Apparent Motion Estimation

Motion analysis techniques that estimate the optical flow velocity field fall into the following main categories. A velocity field is defined as a vector field of velocity: to each pixel correspond a velocity vector.

2.3.1 Local Correlation Tracking (LCT)

The LCT is a procedure that gives the displacement field minimizing the cross-correlation quantity

$$C(\vec{b},\vec{x}) = \left\langle \frac{I_1 - \mu_{I_1}}{\|I_1 - \mu_{I_1}\|}, \frac{T_{\vec{b}}(I_2 - \mu_{I_2})}{\|T_{\vec{b}}(I_2 - \mu_{I_2})\|} \right\rangle_{\Omega(\vec{x})} \tag{2.1}$$

where $\langle \cdot, \cdot \rangle_{\Omega(\vec{x})}$ is the inner product over the window domain centred on $\vec{x}$, $\|\cdot\|$ is the L^2 norm over $\Omega(\vec{x})$, μ_I is the mean of the signal I, and T is the translation operator such that $T_{\vec{b}}I(\vec{x}) = I(\vec{x}+\vec{b})$. The quantity $C(\vec{b},\vec{x})$ is the correlation coefficient between both signals for the estimated displacement $\vec{b}$. The LCT displacement map $\widehat{\vec{b}}$ at each location $\vec{x}$ is given by

$$\widehat{\vec{b}}(\vec{x}) = \arg\max_{\vec{b}\in\Omega_N} C(\vec{b}, \vec{x}) \ . \tag{2.2}$$

The main disadvantage of the correlation-based methods is its lack of robustness: a small perturbation in the data caused *e.g.* by noise can cause dramatic change of the estimated displacement. This will be of particular importance in tracking applications, since it may cause an irremediable loss of a tracked feature. This approach is limited to structured environments in which a dense distribution of features is present.

2.3.2 Energy-based approach

The second important class of motion estimation algorithms are energy-based. In this case, the optical flow is defined as the minimization of an energy term E measuring the deformation rate over the entire image domain Ω. In the pioneering work of [51], the velocity $\hat{V} = (\hat{u}, \hat{v})$ is the minimizer of

$$\hat{V} = \arg\min_{u,v} E_{\text{HS}}(u, v) \tag{2.3}$$

where

$$E_{\text{HS}}(V) = \int_\Omega \|\vec{\nabla} I \ \cdot \vec{v} + I_t\|^2 + \lambda^2(\|\vec{\nabla} u\|^2 + \|\vec{\nabla} v\|^2) \, d\vec{x} \tag{2.4}$$

where λ is a free parameter that regularizes the motion field, $\vec{\nabla} I$ is the image spatial gradient, and I_t is the image sequence temporal gradient. To get the motion field , Equation (2.4) is minimized with Euler-Lagrange equation. This method has been applied to imaging of fluid motions by [22].

2.3.3 Gradient-based approach

The third class is the gradient-based family of motion estimation. Though several approaches have been proposed, we choose here the Lucas-Kanade approach for its simplicity and its proved efficiency. It is easily verifiable that the minimizer of the right hand side of Equation (2.2) is equal to the minimizer of

$$E(\delta\vec{x}, \vec{x}) = \int_\Omega \|I_2(\vec{x} + \delta\vec{x}) - I_1(\vec{x})\|^2 d\vec{x} \ .$$

2.4 The Lucas-Kanade Method

In 1981, Lucas-Kanade (LK) proposed their method for solving the optical flow from two successive images. The advantage of the LK approach is the estimation of the covariance matrix obtained in the Least Squares (LS) estimation. The locality of the estimation ensures that a perturbation caused by an error at one location only has a local impact over the global field. It also permits a local prediction of the error of estimation, which can later on be used to select the most reliable regions, *i.e.* the regions where the predicted error is the lowest. There exists automatic methods for choosing the matching window [77].

2.4.1 Optical Flow Assumptions

The 2D apparent motion field is the projection in the image plane of the 3D velocity field of the moving coronal plasma. We distinguish between three different velocity vector fields:

- the 3D motion (real motion),
- the apparent motion (projected speed in image plane),
- estimation of the apparent motion: the optical flow quantity.

The 3D motion is well defined when the emitting source is opaque, but the corona is optically thin: the emitting source of radiative flux is not well defined over the line-of-sight. The photon flux is integrated along the optical path in the coronal plasma. This effect of transparency should be kept in mind in the interpretation of the velocity fields. Here we note by I the intensity of the image, $\vec{x} = (x, y)^T$ (index T means transpose) is the location of a pixel, and t is the time variable. In the optical flow method that we use, the motion $\vec{v}(\vec{x}, t)$ is computed from the intensities in the neighbourhood of the pixel at time t and time $t + \delta t$.

Brightness Constancy Assumption

The principle of the optical flow technique is based on the assumption that the brightness pattern of the image is constant during the sequence. This assumption is usually referred to as the Brightness Constancy Assumption (BCA). This assumption can be written as:

$$\frac{dI}{dt}(\vec{x}(t), t) = 0 \ . \tag{2.5}$$

The BCA assumption can be modified so that the brightness pattern of the image is linearly evolving during the sequence. We refer to this assumption as the Modified Brightness Constancy Assumption ($MBCA$), which can be written as:

$$\frac{dI}{dt}(\vec{x}(t), t) = c \ .$$

2.4.2 Optical Flow Constraint Equation (OFCE)

If we expand the left-hand side of equation (2.5) in terms of partial derivatives, taking into account the dependence of I on $\vec{x}$ (spatial coordinates) and t (the temporal variable), as well as the dependence of x on the time t, we get:

$$\frac{dI}{dt}(\vec{x}(t),t) = \frac{dx}{dt} \times \frac{\partial I}{\partial x} + \frac{dy}{dt} \times \frac{\partial I}{\partial y} + \frac{\partial I}{\partial t} \tag{2.6}$$

The brightness constancy assumption finally gives, for each pixel $\vec{x}$ of an image I:

$$\vec{\nabla} I \cdot \vec{v} + I_t = 0 \text{ (OFCE)} \tag{2.7}$$

where

$$\vec{v} = (v_x, v_y)^T = (\frac{dx}{dt}, \frac{dy}{dt})^T, \tag{2.8}$$

$$\vec{\nabla} I = (\frac{\partial I}{\partial x}, \frac{\partial I}{\partial y})^T, \tag{2.9}$$

$$I_t = \frac{\partial I}{\partial t} \tag{2.10}$$

For the computation of the spatial derivatives, we use robust kernel of convolution (finite difference with implicit interpolation). Temporal derivative is estimated by a forward finite difference (difference of the two successive images). Unfortunately, the Brightness Constancy Assumption (BCA) only provides one equation for two unknowns per pixel (the two components of the velocity vector). This is equivalent to the aperture problem (one equation, two unknowns). In order to solve aperture, we use the Lucas-Kanade algorithm. The optical flow formulation is in fact equivalent to a linearization of the Local Correlation Tracking (LCT).

2.4.3 Lucas-Kanade Formulae

In the LK algorithm [67], a local uniformity of the velocity field is assumed. For a given neighbourhood $N_{\vec{x}}$ of a pixel located at $\vec{x}$, we define a linear system of N optical flow equations, one per each pixel in $N_{\vec{x}}$. This linear system is solved by minimizing an energy E_I:

$$\vec{v}_{LK} = \arg\min_{\vec{v} \in V} E_I(\vec{v}) \tag{2.11}$$

where

$$E_I(\vec{v}) = \sum_{\vec{x} \in N_{\vec{x}}} (\nabla \vec{I} \cdot \vec{v} + I_t)^2 \tag{2.12}$$

Equations (2.11) and (2.12) can also be seen as a Taylor expansion of a local correlation energy to be minimized, for small temporal shifts δt:

$$\min_{v_x, v_y} \sum_{\vec{x} \in N_{\vec{x}}} (I(x + v_x \delta t, y + v_y \delta t, t + \delta t) - I(x, y, t))^2 \tag{2.13}$$

For the purpose of improving our motion analysis tool, we introduced a new constraint that makes the algorithm more robust to the intensity variations that are not caused by the motion of the emitting coronal source. The BCA [51] states that the source of intensity remains constant over time. This provides a single equation per pixel –the OFCE– while there are two unknowns, namely the two velocity vector coordinates. This is the *aperture problem*. To solve this under-determination, following Lucas and Kanade [67], we further assume a local uniformity of the velocity field in the neighbourhood of the estimation. An alternative approach would be to solve globally the velocity field [51] by adding a constraint on its smoothness. The disadvantage of this latter method is that bad estimations can propagate to the rest of the image. Furthermore, a local diagnostic of the quality of the estimation would be impossible when the solution is global. Other important approaches to optical flow computation are probabilistic [100, 101] or robust minimization [14].

Brightness Variation and Affine Models

This Local Uniformity Assumption (LUA) assumption is valid when the shapes of the moving objects remain constant within the considered neighbourhood: this can be assumed for sufficiently short time and spatial scales. One may also introduce additional parameters in the model of motion: the global variation of intensity δI and also affine transform parameters. Originally, Lucas introduced this parameter to measure the global change of illumination in the scene. Several mechanisms may explain the variation of intensity that is not due to the 3D motion. We will see in Chapter 3 that disentangling brightness variation from 2D motion in apparent motion, when it is possible, is a way to solve this ambiguity and to obtain an optical flow regularized against the aperture effect. As noted by Shi and Tomasi [97], "*translation gives more reliable results than affine changes when the inter-frame camera translation is small, but affine changes are necessary to compare distant frames to determine dissimilarity*", and affine changes are shown to be superior to a pure translation model when they are used to measure dissimilarity in tracking applications over long sequences.

Some Properties of Optical-Flow Estimation

Lucas and Kanade [67] establishes the formula of the estimated displacement $\widehat{\delta x}$ as a function of the real value δx of the displacement. In the ideal $1D$ continuous case, where the Fourier series expansion of I defined over the interval $[0, 1]$ is given by $I(x) = \sum r_k \cos(2\pi kx + \theta_k)$, the estimation $\widehat{\delta x}$ of the displacement δx to measure between $I(x)$ and $I(x + \delta x)$ is given by

$$\widehat{\delta x} = \frac{\sum_{k\geq 0} r_k^2 k \sin(2\pi k \delta x)}{2\pi \sum_{k\geq 0} r_k^2 k^2} \ , \tag{2.14}$$

where the r_k's are the Fourier series coefficients of the signal I. The optical flow equation (formula 2.7) gives a perfect solution when the signal is linear (straight line in the neighbourhood of estimation), and the formula (2.14) allows for a prediction of the error when the signal is not linear. One important remark is that this error depends only on the power spectrum of the signal and not on the phase spectrum: two images will have similar optical-flow motion estimation if they have a common power spectrum, even if their phase spectra greatly differs, meaning that they may appear dissimilar.

As a result, for a pure sine wave such as a signal $I(x) = 1 - \cos(2\pi x)$ defined in the interval $[0, 1]$, the estimated displacement is given by

$$\widehat{\delta x} = \delta x - \frac{2\pi^2}{3}\delta x^3 + O(\delta x^5) \ . \tag{2.15}$$

The relative error $\epsilon = \| \frac{\widehat{\delta x} - \delta x}{\delta x} \|$ is equal to

$$\epsilon = \frac{2\pi^2}{3}\delta x^2 + O(\delta x^4) \ . \tag{2.16}$$

We define S_I to be the support of the sinusoidal signal I over the $[0, 1]$ interval given by

$$S_I = 2\sqrt{\int_0^1 (x - \mu)(I(x)^2)dx} \tag{2.17}$$

where μ is the central value of the support S_I (in this simple case, $\mu = 0.5$). In the case of the signal $I(x) = 1 - \cos(2\pi x)$, the support is equal to $S_I = \frac{1}{2\pi}\sqrt{\frac{\pi^2}{2} - 2}$. This provides the following empirical rule

$$\frac{\delta x}{S_I} = \sqrt{\frac{3}{\pi^2 - 4}} \times \epsilon^{1/2} \tag{2.18}$$

where ϵ is the relative error on δx given by Equation (2.16). One derives from this formula that independently of the size of the object and under the previous assumptions, the error ϵ reaches 100 % when the displacement δx is 71.5% of the object typical size S_I. The error goes down to 10 % for a displacement equal to 23% of the object size S_I, and to 1 % when δx is equal to 7.15% of S_I. From this properties one can derive:

- the relation between the displacement and the shape of the signal,
- the role of the derivation formula,
- the importance of smoothing before estimation.

The shape of the signal is determined by the signal itself and by the window, or neighbourhood, where the motion is locally estimated. The smoothing, applied on the signal I prior to the estimation, tends to lower the effect of the high-terms in Equation (2.15) because it attenuates the high-frequency terms.

In the real case, the signal is not continuous but this does not change the main conclusions on the last comments, although the previous results is not valid anymore in the case of small displacements because the discretization effects must be taken into account. Furthermore, the signals are not pure sinusoids and the other orders in the error formula (2.14) should be considered as well. An important source of error is also, for small displacements δx, the noise contained in the difference image. Robinson [87] has further developed this study. This motivates the development of a method of error prediction that is presented in Section 3.4. It is based on the fact that the LK approach has the potential of providing the error on estimation through the least-square formula of the covariance matrix.

2.4.4 Feature Selection and Tracking Algorithms

The extraction of features, or tracers, and their tracking over time has been proposed by Shi and Tomasi [97]. The goal was to restrict the processing of a video sequence to trackable features, in the sense of the Shi and Tomasi method who proposed a feature tracker based on the LK estimation. We have modified it towards an efficient tracking procedure adapted to the Extreme Ultraviolet (EUV) features of the solar atmosphere.

2.5 Velocity Estimation Techniques and Tracking Methods in Solar Physics

The dynamic nature of the solar atmosphere has been widely observed and modeled [*e.g.* 70, 80, 92]. The past two decades have highlighted the unsuitability of static assumptions in studying the physics of the chromosphere, transition region, and corona. The probe of dynamics is concerned with the effects of forces upon motion, and reciprocally, the knowledge of motions and accelerations must constrain the models, consequently validating or falsifying the underlying physics. While forces are invisible, motion can be quantitatively estimated by observational means; both spectroscopy and image sequences can reveal motion. Spectroscopy informs on the LOS velocity component for moving plasma from Doppler measurements, while movies exhibit the transverse component of the speed. Both approaches have their respective advantages and restrictions, but they are complementary when the two types of observations coincide [*e.g.* 62].

Temperature variations are ubiquitous, and when they coincide with instrumental passbands, the observed volumes of plasma brighten or darken. As long as too few bandpasses are recorded, the Differential Emission Measure (DEM) cannot be

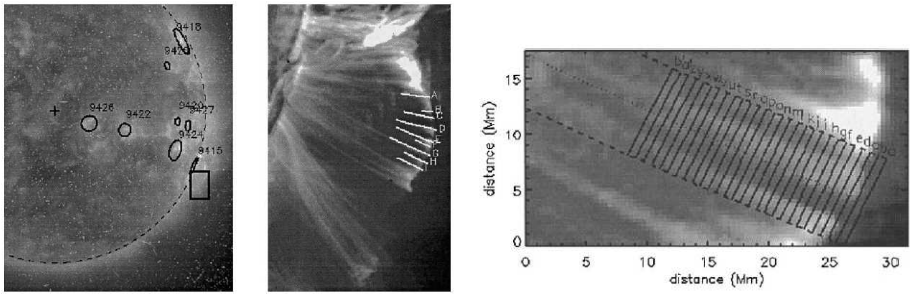

(a) Line segments along the coronal loops. (b) Paths perpendicular to the line segments.

Figure 2.2: Locations where X-T diagrams are used to estimate motions, as used by Verwichte *et al.* [104]. Along the paths, the motion is found by fitting a straight line in the X-T diagram.

recovered and it is necessary to separate motion from Brightness Variation (BV). We show the required conditions for this disentanglement in Section 3.4.

Since the beginning of EUV imaging of the solar atmosphere, numerous authors have developed methods for apparent motion estimation. Specific methods exist for tracking the propagation of dimmings by solar physicists to analyze the precursors of the Coronal Mass Ejection (CME) onsets, but also as the main feature of Extreme ultraviolet Imaging Telescope (EIT) waves [82].

The "X-T" diagram is the most popular and has recently been used by [104]. It consists in tracing manually the line segments along which the intensity is measured at time t; several measurements are done at successive instants, which fills an X-T space where X is the location along the line segment and T is the time. In this diagram, the intensity of a feature with a linear motion is spread over a line whose slope is the motion of the feature.

This technique has been applied by Aschwanden *et al.* [5] for the first detection of spatial oscillation of loops in EUV images (TRACE 17.1 nm). Standing wave mode (with fixed nodes at the footpoints) have been detected also using X-T diagrams by Robbrecht *et al.* [86] who analyze a propagating disturbances along a loop. Schrijver *et al.* [93] have catalogued transverse oscillations in coronal loops observed with TRACE and 17 loop oscillations were identified. Other examples include Noglik *et al.* [74] who calculate the reconnection rate from the estimated velocity at which successive loops brighten.

Nowadays there exist several methods of CME tracking. The first major CME detector and tracker has been developed at Royal Observatory of Belgium (ROB) by Robbrecht and Berghmans [85]. This method an elaborated X-T diagram representation also include Hough transform. It has been made entirely and nowadays achieves autonomous detection of CME providing their location and their speeds.

The solar rotation dominates the motion in image sequences. The first method of sunspot tracking has been proposed by [98]. Recent works [*e.g.* 15, 106] have studied the differential rotation of the atmosphere. After compensation of differential rotation, the residual motion yields a wealth of insights. The method of tracking is used here for measuring the solar differential rotation. Brajša *et al.* [15] uses a feature-based method to track bright points and Point-like Structures (PLS), where each feature is a point in the $(\mathrm{B}, \omega_{\mathrm{rot}})$ plane, with B the heliospheric latitude and ω_{rot} the angular velocity. The authors then fit a parametric model of differential rotation through the cloud of feature points. This method is sensitive to the reliability of the feature extraction.

Among the methods of motion estimations [8], gradient-based and matching-based, such as LCT are said to be *dense*, in contrast to feature-based methods, in the sense that they estimate the velocity at every pixel and not only at sparse features. Dense does not mean that the quality of the estimation is uniform over the image, and we expect that some regions will have better estimations if motion is better defined at these locations. So far, the main motion analysis tool applied in solar physics involves local correlation technique to magnetic field component images (magnetograms): November and Simon [75], Simon *et al.* [99]. Local correlation tracking techniques lacks efficiency in noisy data, especially in the case of EUV images of the solar corona. In feature-based methods, the extraction of the features is a problematic preprocessing step. Some authors have proposed matching techniques based on the LCT for sequences of photospheric images [75, 107]. This technique has also been modified by Roudier *et al.* [89] and applied to TRACE photospheric data [see 60, 61]. All these techniques deal with photospheric velocity flows. Note that the present study does *not* incorporate any physical assumption, but instead utilizes *only* the information found in the two images.

The velocity of magnetic features, observed in magnetograms at the photospheric level have been successfully tracked by combining the induction equation with standard LCT techniques [107] or global optimization methods [66]. The latter method, called the minimum energy fit, demands that the photospheric flow agrees with the observed photospheric field evolution according to the magnetic induction equation. Schuck [95, 96] also suggested to keep optical flow consistent with the induction equation in order to estimate correctly motion in sequence of magnetograms. A recommendation from an expert group on magnetogram velocity estimations have been published [27].

Combined with segmentation techniques [6], tracking using LK has also been successfully used in [7].

Chapter 3

A Motion Analysis Algorithm Dedicated to EUV Images of the Solar Atmosphere

Movies of the solar atmosphere reveal motion and variations of brightness. In particular, sequences of coronal images exhibit the plane-of-the-sky component of the velocity combined with other variations of the signal. The various solar atmospheric motions described in Chapter 1 demonstrate the need of a versatile tool able to measure apparent velocity. Our method consists in adapting a gradient-based estimation of optical flow [67, 68] in order to estimate simultaneously the apparent motion vector and the variation of brightness from two successive images of the solar atmosphere in the extreme-ultraviolet domain, such as those recorded by the Extreme ultraviolet Imaging Telescope (EIT) on board the Solar and Heliospheric Observatory (SOHO) or by the Transition Region and Coronal Explorer (TRACE). The displacement map is a projection of the velocity field of the plasma, while the brightness variation map measures the instantaneous variation of emission along the Line-Of-Sight (LOS). The *Velociraptor* algorithm presented here is a multiscale optical flow algorithm derived from the local gradient-based technique of Lucas-Kanade (LK) [67], see Chapter 2. This work deals only with apparent motions, focusing specifically on solar Extreme Ultraviolet (EUV) images as produced by EIT [28] on board SOHO and TRACE [45]. However these developments have potential for application to magnetographic, photospheric, and coronagraphic image sequences or future observations from EUV imagers PROBA2-SWAP, SDO-AIA, or STEREO-SECCHI. In Section 3.1, we present the formulation of our new method of motion analysis. In Section 3.8, we show the results of the calibration of the method on synthetic signals. Several applications will be further detailed in Chapter 4 and 6. It is *symmetric* (see Section 3.2), and regularized against aperture effects (see 3.5), and we show the effects of this approach on synthetic data.

3.1 Description of the Algorithm

In order to calculate the coordinates of the velocity vector for each pixel, we first establish the optical flow (OF) equations using the Brightness Constancy Assumption (BCA) described in Chapter 2. In the sequel, we extend the optical flow to estimate both the velocity and brightness variation (δI) fields in the special case of coronal ultraviolet images. A *multiscale* computation of the flow iterates the estimation from larger to smaller scales, the scale being associated to the size of the neighborhood where the least-square estimation is performed. The estimation is updated across scales, along with its *quality* index, as defined in Section 3.4, used for error prediction (see Section 3.8.1). In the present section, after describing the preprocessing that we apply to the images (Section 3.1.1), we introduce the symmetric optical flow equations (SOFA, see Section 3.2). It induces a symmetry constraint between the first and the second images, and we interpret this constraint in the Bayesian framework.

3.1.1 Preprocessing

First, we remove the cosmic ray hits (CRHs) using a median filter provided by the Interactive Data Language (IDL) solar soft library. This preprocessing may have an impact on the intensity of the signal, but has the advantage of preventing unreliable estimations caused by the Cosmic Ray Hit (CRH) features. Another way of removing the CHRs has been proposed by Jacques [56]. In the case of solar EUV images, we transform the image using a logarithmic or square root function to bring out the low-intensity part of the signal. Thirdly, we smooth the image using a Gaussian kernel. This step allows us to compute robust spatial gradient estimations. Thus, if g_a is the Gaussian kernel of our smoothing, of bandwidth a, we denote the preprocessed image $I_{\text{preprocessed}} = g_a \star I_{\text{raw}}$. The spatial derivative along x (same along y) is

$$\frac{\partial I_{\text{preprocessed}}}{\partial x} = \frac{\partial}{\partial x}(g_a \star I) = \frac{\partial g_a}{\partial x} \star I. \tag{3.1}$$

We have access to an analytical derivative of the preprocessed signal $I_{\text{preprocessed}} = g_a \star I$ where a is the scale of the Gaussian function $g_a(\vec{x}) = \frac{1}{2\pi a^2} \exp\left(-\frac{\vec{x}^2}{2a^2}\right)$. An anisotropic filtering would be more adapted to preserve edges, especially for the preservation of the coronal loops. In the rest of this chapter, we do not recall this preprocessing and only refer to I. We choose a scale $a = 2$ pixels so that it does not filter the images too much. The subscripts x and y in I_x or I_y designate the partial derivative with respect to x or y.

3.1.2 Optical-flow Equations

There are two equivalent formulations of the Optical Flow Constraint Equation (OFCE): Partial Differential Equation (PDE) and image registration. We want to estimate the deformation, if it is "small enough", between the first image I_1 and the second I_2. The PDE formulation can be found in appendix.

Image Registration

We denote $\vec{x} = (x, y)^T$, the spatial position in the image plane (plane-of-the-sky). We can formulate the BCA as

$$I_2(\vec{x} + \delta\vec{x}) - I_1(\vec{x}) = 0. \tag{3.2}$$

A linear approximation of this equation, using a Taylor series expansion at the first order on the left hand side, gives

$$\vec{\nabla} I_2 \cdot \delta\vec{x} + I_2(\vec{x}) - I_1(\vec{x}) = \xi(\vec{x}, \delta\vec{x}) \ . \tag{3.3}$$

This formulation, where the time variable does not appear explicitly, is used by Lucas and Kanade [67]. The motion vector can then be defined as $\vec{v} = \delta\vec{x}/\delta t$, where δt is the time difference between the two images I_1 and I_2. This approach leads to the same equation as the PDE formulation, so that in practice they are equivalent.

Least-square Estimation of Optical Flow

In the original Lucas and Kanade [67] optical flow estimation which aims to solve the aperture problem, a local uniformity assumption (LUA) is imposed on the velocity vector: $\vec{v}$ has to be uniform over a local neighborhood (see Figure 3.1). The set of OFCE equations in this neighborhood Ω yields a linear system, where the unknowns are the two parameters of the deformation (the motion vector). If $\Omega(\vec{x})$ (centred on $\vec{x}$) contains $N > 2$ pixels, this assumption provides more equations of type (3.3) than unknowns δx_i and correspond to the linear system $A\delta x = b$, where

$$A = \begin{bmatrix} I_{2x}(\vec{x}_1) & I_{2y}(\vec{x}_1) \\ \vdots & \vdots \\ I_{2x}(\vec{x}_N) & I_{2y}(\vec{x}_N) \end{bmatrix} \text{ and } b = \begin{bmatrix} -(I_2 - I_1)(\vec{x}_1) \\ \vdots \\ -(I_2 - I_1)(\vec{x}_N) \end{bmatrix} .$$

This linear system is overdetermined and can be solved using a weighted linear least-square method [83]. The local uniformity assumption means that one imposes Equation (3.3) in such a way as to be true locally around the location $\vec{x}$, that is, over a finite domain neighborhood $\Omega(\vec{x})$. The LK optical flow is the least-square minimizer of ξ in (3.3) on Ω

$$\hat{\delta\vec{x}}(\vec{x}) = \arg\min_{\delta x} \|\xi(\delta\vec{x})\|^2_{\Omega(\vec{x})} \ , \tag{3.4}$$

where $\|\xi(\delta\vec{x})\|_{\Omega(\vec{x})} = (\sum_{i=1}^{N} \xi(\vec{x}_i, \delta\vec{x})^2)^{1/2}$ is the Euclidean norm on $\mathbb{R}^{\mathrm{N}}$ of ξ. This solution is the maximum likelihood estimator when the residual term ξ is a random variable following a Gaussian distribution $N(0, \sigma_\xi^2)$. In fact, we assign weights to each pixel, or equivalently to each optical flow equation in the neighborhood $\Omega(\vec{x})$, so that the pixel at the centre has a greater statistical weight than at the boundaries of $\Omega(\vec{x})$. The minimising vector defined in Equation (3.4) is the solution of the normal equation $A^T A \delta\vec{x} = A^T b$. When the matrix $A^T A$ is invertible, the solution is

$$\hat{\delta\vec{x}} = (A^T A)^{-1} A^T b \ . \tag{3.5}$$

We denote $V_\xi = \sigma_\xi^2 I$, the covariance matrix of the residual error ξ. The covariance matrix of $\hat{\delta\vec{x}}$ is then given by

$$V_{\hat{\delta\vec{x}}} = (A^T V_\xi^{-1} A)^{-1} \ . \tag{3.6}$$

In the rest of this work, we refer to this covariance matrix as $V_{\hat{\delta\vec{x}}}$ and use it to define our criterion for the quality of the estimation.

3.2 Symmetric Optical Flow Analysis (SOFA)

We opt for a symmetric formulation of the optical flow, and this generates a stabilising constraint on the flow $\delta\vec{x}$. To impose symmetry in the optical flow estimation, we combine the two reciprocal equations

$$\begin{aligned} I_2(\vec{x} + (\delta\vec{x} + \delta\vec{x}_{th})) &= I_1(\vec{x}) \ , \\ I_1(\vec{x} - (\delta\vec{x} + \delta\vec{x}_{th})) &= I_2(\vec{x}) \ . \end{aligned}$$

We linearise both equations assuming that $\delta\vec{x}_{th} = \vec{0}$. It is possible to impose a predetermined $\delta\vec{x}_{th}$, for instance the theoretical differential rotation or the estimate on a larger scale as below. We get

$$\vec{\nabla} I_2 \cdot \delta\vec{x} + I_2(\vec{x}) - I_1(\vec{x}) = \xi_1 \ , \tag{3.7}$$

$$\vec{\nabla} I_1 \cdot \delta\vec{x} + I_2(\vec{x}) - I_1(\vec{x}) = \xi_2 \ . \tag{3.8}$$

We denote I_m the mean image and I_d the difference image

$$\begin{aligned} I_m &= \frac{I_1 + I_2}{2} \ \text{(mean)} \ , \\ I_d &= I_2 - I_1 \ \text{(difference)} \ . \end{aligned}$$

Adding and subtracting (3.7) and (3.8), we obtain

$$2 \times \left(\vec{\nabla} I_m \cdot \delta\vec{x} + I_d(\vec{x})\right) = \xi_1 + \xi_2 \ , \tag{3.9}$$

$$\vec{\nabla} I_d \cdot \delta\vec{x} = \xi_1 - \xi_2. \tag{3.10}$$

The goal of the algorithm is now to minimise a redefined cost function $\|\xi\|^2$, using the parallelogram identity, as

$$\|\xi\|^2 = \frac{1}{2}(\|\xi_1\|^2 + \|\xi_2\|^2) = \|\frac{\xi_1 + \xi_2}{2}\|^2 + \|\frac{\xi_1 - \xi_2}{2}\|^2 \ . \tag{3.11}$$

We denote $\hat{\delta\vec{x}}$ the vector that minimises the quantity $\|\xi(\delta\vec{x})\|^2_\Omega$. We can interpret this new minimisation as a Tikhonov regularization. The advantage of this method is that the regularization constraint is derived from the data (the matrix M further introduced) and does not require any extra arbitrary parameter. Furthermore, the estimation is symmetric: the parameters that minimise $\|\xi\|^2$ do not depend on the ordering between I_1 and I_2. We define

$$\begin{aligned}
A &= \begin{bmatrix} I_{m,\vec{x}}(\vec{x}_1) & I_{m,y}(\vec{x}_1) \\ \vdots & \vdots \\ I_{m,\vec{x}}(\vec{x}_N) & I_{m,y}(\vec{x}_N) \end{bmatrix} , \\
b &= \begin{bmatrix} -I_d(\vec{x}_1) \\ \vdots \\ -I_d(\vec{x}_N) \end{bmatrix} , \\
M &= \frac{1}{2}\begin{bmatrix} I_{d,\vec{x}}(\vec{x}_1) & I_{d,y}(\vec{x}_1) \\ \vdots & \vdots \\ I_{d,\vec{x}}(\vec{x}_N) & I_{d,y}(\vec{x}_N) \end{bmatrix} .
\end{aligned}$$

The cost function $\|\xi\|^2$ can be written as

$$\begin{aligned}
\|\xi\|^2 &= \frac{1}{2}\left(\|A\delta\vec{x} - b\|^2 + \|M\delta\vec{x}\|^2\right) \\
&= \frac{1}{2}\left(\|A\delta\vec{x} - b\|^2 + \|\delta\vec{x}\|^2_{M^TM}\right) \ .
\end{aligned}$$

A possible interpretation of the regularization may be found in the Bayesian framework: it appears that imposing the symmetry may be equivalent to adding a prior constraint to the vector $\delta\vec{x}$. Using Bayes' rule, we may interpret Equation (3.11) as the following conditional probability

$$\Pr(\delta\vec{x}|I_d) = \frac{\Pr(I_d|\delta\vec{x}) \times \Pr(\delta\vec{x})}{\Pr(I_d)} \ , \tag{3.12}$$

where

$$\Pr(I_d|\delta\vec{x}) \propto \exp\left(-\frac{1}{2}I_d^T V_{\vec{\xi}}^{-1} I_d\right) \ , \tag{3.13}$$

$$\Pr(\delta\vec{x}) \propto \exp\left(-\frac{1}{2}\delta\vec{x}^T(M^T V_{\vec{\xi}}^{-1} M)\delta\vec{x}\right) \ . \tag{3.14}$$

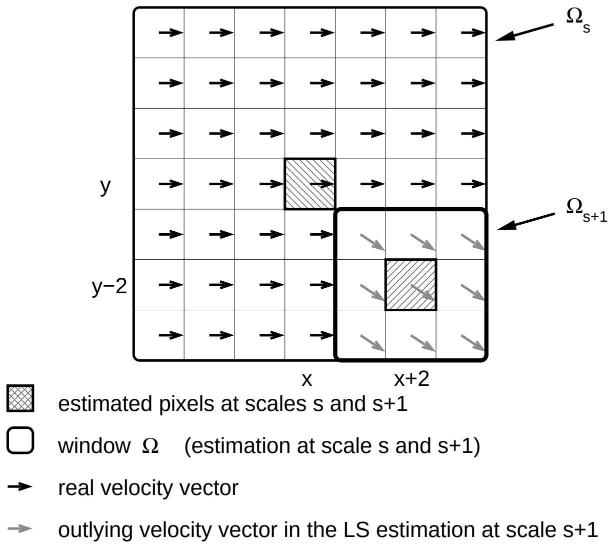

Figure 3.1: The local uniformity assumption in the multiscale estimation process with an update between scale $s+1$ and scale s. In the lower right corner, the estimation at location $(x+2, y-2)$, and the quality Q will be updated (see Section 3.4).

Indeed, Equation (3.10) can be used to define a prior distribution on $\delta\vec{x}$. This prior distribution plays a role when the gradient texture is deformed, and the two diagonal elements $M^T M$ then represent the deformation rates along the x and y axes. When the gradient texture is deformed between I_1 and I_2, because of occlusion or strong deformation, then the estimation is forced to tend to the displacement vector used to linearise the model (here $\vec{0}$ vector, but it could be *e.g.* the differential rotation). Basically, it stabilises the estimation towards the reference value when the gradient texture is modified between I_1 and I_2. Finally, we get the pseudo-inverse solution

$$\hat{\delta\vec{x}} = (A^T A + M^T M)^{-1} A^T b \ . \tag{3.15}$$

In the Bayesian interpretation, the covariance matrix of $\delta\vec{x}$ is

$$V_{\hat{\delta\vec{x}},\mathrm{sym}} \quad = \quad (A^T V_\xi^{-1} A + M^T V_\xi^{-1} M)^{-1}.$$

A symmetry optical flow was originally proposed by Lucas [68] and is detailed in Section B.1.1.

3.3 Brightness Variation Maps

We extend the OFCE with δI, which estimates the brightness variation between the two images, relaxing the BCA assumption. This approach was suggested by Lucas

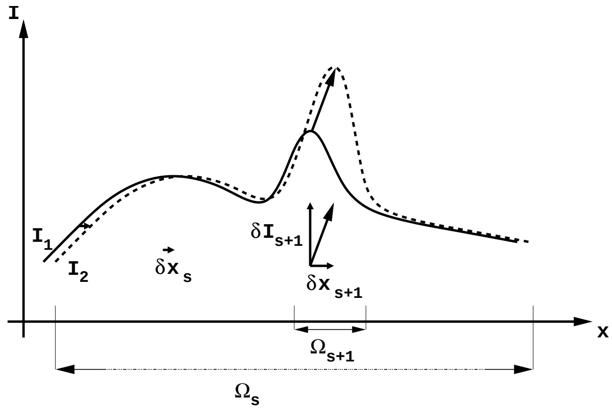

Figure 3.2: In this 1D example, the estimation is locally updated in motion and brightness variation from scale s to $s+1$.

and Kanade [67] and recently used by several authors [*e.g.* 76, 79]. An example of a 1D signal undergoing a translation plus a brightness variation is shown in Figure 3.2. The Brightness Variation (BV) map can be interpreted as the variation in the LOS emission parameters (temperature and density).

Pixel Weighting In addition to this extension, we weight each pixel equation within the neighborhood Ω using a function w to penalise the pixels that are far from the estimated pixel $\vec{x}$, avoiding a "square paving" effect. The symmetric optical flow Equation (3.9) becomes

$$w_i \cdot \left(\vec{\nabla} I_m \cdot \delta\vec{x} + I_d + \alpha \cdot \delta I \right) = \xi(\vec{x}, \delta\vec{x}), \tag{3.16}$$

but Equation (3.10) remains unchanged (except for the weights w_i). The α parameter is used to define δI in the same unit as δx and δy. The set of weights w_i penalises the pixels of the neighborhood Ω that are far from the pixel where the parameter set has to be estimated. They are weighted so that

$$\sum_{x_i \in \Omega} w_i^2 = 1.$$

Multiscale Scheme In order to make the maps $(\delta x, \delta y)$, which corresponds to the velocity vector map, and δI as local as possible, we compute the optical flow in a multiscale framework (see Figs. 3.1 and 3.3). The scale is defined by the scale parameter s of the Gaussian kernel associated to Ω. The first computation is carried out on a predefined large scale s_0. On this scale, a large number of pixels are used in the estimation, which therefore increases its significance. This estimation may nevertheless be biased. Furthermore, within a large neighborhood (*i.e.* large scale), the hypothesis made on the optical flow (extended BCA and Local Uniformity

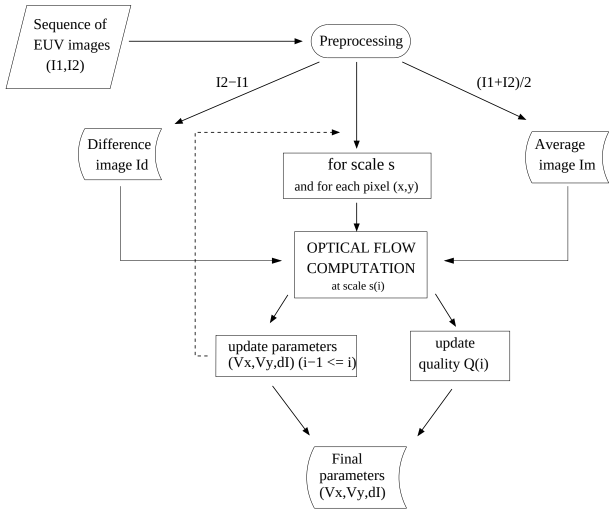

Figure 3.3: Overview of the motion analysis algorithm.

Assumption (LUA)) is less valid. To compensate for this effect, we add a multiscale updating step. It consists in an update of the parameter estimation from larger to smaller scales. This is explained in Section 3.6.

From now on, we note the vector to estimate in the space of parameters

$$\hat{\vec{\theta}} = (\delta x, \delta y, \delta I)^T \ .$$

The solution becomes

$$\hat{\vec{\theta}} = (A^T A + M^T M)^{-1} A^T b \ , \tag{3.17}$$

while the covariance matrix of $\vec{\theta}$ is still given by Equation 3.6.

3.4 Quality of Estimation

Contrary to global methods such as in Horn and Schunck [51], our optical flow approach gives the possibility of carrying out the registration depending on the neighborhood content. For that reason, we define an index Q (for "quality"). We use this index for error prediction of the estimation. In order to illustrate the meaning of Q, we can use the space of parameters $(\delta x, \delta y, \delta I)$. If we assume $V_\xi = \sigma_\xi^2 I$ and since $A^{\mathrm{T}}A$ is symmetric, we can write $A^{\mathrm{T}}A = P^{\mathrm{T}}D'P$, or $A^{\mathrm{T}}A + M^{\mathrm{T}}M = P^{\mathrm{T}}D'P$ in the symmetric case, where $P^{\mathrm{T}} = P^{-1}$. Equivalently, we have

$$\begin{aligned} V_{\delta\hat{\vec{\theta}}} &= PDP^{\mathrm{T}} \\ \text{where } D &= \begin{bmatrix} \sigma_\xi^2/\lambda_1 & & \\ & \sigma_\xi^2/\lambda_2 & \\ & & \sigma_\xi^2/\lambda_3 \end{bmatrix} = \sigma_\xi^2 D'^{-1} \\ \text{and} \quad & \lambda_1 < \lambda_2 < \lambda_3. \end{aligned}$$

We denote $\vec{p_i}$ as the eigenvectors of the matrix $V_{\hat{\vec{\delta\theta}}}$, which are the columns of the matrix $P = (\vec{p_1}\ \vec{p_2}\ \vec{p_3})$. Our solution can be written as

$$\hat{\vec{\theta}} = \hat{\theta}_1 \vec{p_1} + \hat{\theta}_2 \vec{p_2} + \hat{\theta}_3 \vec{p_3}. \tag{3.18}$$

We then define our quality index as:

$$Q = (Det\, D)^{-1/3} = \frac{(\prod_i \lambda_i)^{1/3}}{\sigma_\xi^2} \ .$$

It is correct to interpret Q^{-1} as the variance around the estimated vector $\vec{\theta}$. We will see that the aperture reduction (see Section 3.5) lowers the components of the estimation that are in the larger variance direction. For that reason, we relate it to the norm of the error vector. If we denote $S = \frac{1}{\sigma_\xi^2}$ and $T = (\prod_i \lambda_i)^{1/3}$, which is homogeneous to λ, we finally obtain

$$Q = S \cdot T \tag{3.19}$$

where S can be seen as the similarity between both images after deformation, while T quantifies the amount of texture in the observation window. Indeed, we have

$$S = \frac{1}{\hat{\sigma_\xi}^2} \ , \tag{3.20}$$

where

$$\hat{\sigma_\xi}^2 = \sum_{x_i \in \Omega} w_i^2 (I_d(x_i) + \alpha \delta I + \vec{\nabla} I_m(x_i) \cdot \vec{\delta x})^2. \tag{3.21}$$

The quantity

$$-(\vec{\nabla} I_m \cdot \vec{\delta x} + \alpha \delta I)$$

is our model for the difference image I_d. In Section 5.2.4, we analyze which part of the observations I_d is explained by this model, and S^{-1} is an estimation of the quantity σ_ξ^2. As the noise on images I_1 and I_2 is assumed to be Gaussian white noise $N(0, \sigma_I^2)$, σ_ξ^2 can be interpreted as an estimation of $2\sigma_I^2$. It is also bounded by the dynamics of the signal. T corresponds to a "texture" criterion. It is homogeneous with $\sum I_x^2$, which indicates that it is high when the texture is well-suited to the motion analysis. It is low when there is a blank-wall effect or a strong aperture. We use the quality criterion for error prediction (see Section 3.8.1). If T is large, then the quality is high because the texture of the signal enables motion analysis (no aperture problem). The use of least-squares is well-adapted in the case where the residual ξ is a Gaussian random variable, but it may be not Gaussian for the following reasons:

- non-Gaussian noise implying a non-Gaussian residual distribution (statistical error): *e.g.* Poisson noise, spatial noise, etc.

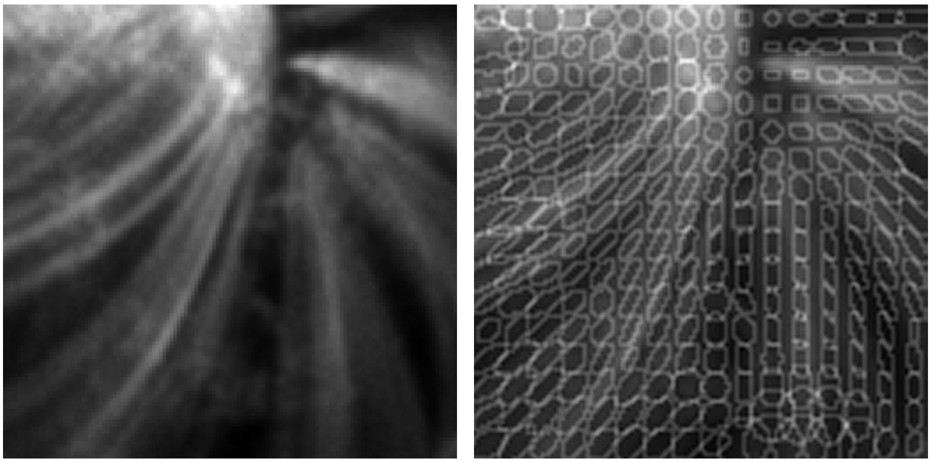

(a) Original image. (b) Error ellipses.

Figure 3.4: Superposition of the error ellipses on top of the original TRACE image. It shows how elongated the ellipses are along the coronal loops.

- modeling error (non-zero second or higher-order terms): motions more complex than translation, non uniform intensity variations,
- noise in the matrix A caused by noisy spatial gradient estimations (spatial aliasing),
- noise in temporal derivative measurement as a consequence of temporal aliasing.

A possible way to cope with non Gaussian errors in the future is to use robust minimisation, or iterative weighted least-squares.

3.5 Aperture Reduction

We correct for the aperture effects using the ellipse of error dispersion. The ellipse of error dispersion is illustrated in Figures 3.4 and 3.5.

The $\vec{p_i}$ vectors (in the space of parameters) are the eigenvectors of the matrix $V_{\hat{\delta\vec{\theta}}}$ defined earlier. Contrary to global methods such as in [51], the LK optical flow approach gives the possibility of carrying out the registration depending on the neighborhood content.

To correct the aperture effect, we apply the following rule

$$\begin{aligned} \vec{\theta} &\leftarrow \vec{\theta} - (\alpha_1 \vec{p_1} + \alpha_2 \vec{p_2} + \alpha_3 \vec{p_3}) \\ \text{where } \alpha_i &= \begin{cases} \beta\, \sigma_\xi^2/\lambda_i \text{ if } |\theta_i| > \beta\, \sigma_\xi^2/\lambda_i \\ 0 \text{ otherwise} \end{cases} \end{aligned}$$

where β is an arbitrary parameter that sets the level of constraint we need for the application. A large β will strongly correct the estimations. The aperture effect between two variables (e.g. $(\delta x, \delta y)$ or $(\delta x, \delta I)$) occurs when there is no unique solution to solve the linear system. The aperture reduction helps the algorithm to choose the smallest norm solution. In the estimation of loop motions (see Section 4.1.3), this constraint tends to remove the aperture along the loop, while keeping the component of the motion perpendicular to the loop (and parallel to the main local direction).

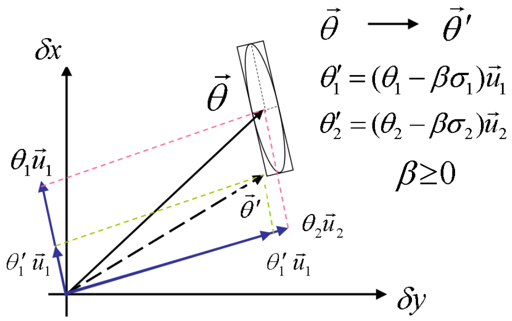

Figure 3.5: Illustration of the aperture reduction mechanism. Each component of the estimated vector is corrected along its corresponding axis of the error ellipse. This has the effect of forcing the estimation to the normal flow when the image pattern is directional, which would otherwise cause an aperture effect. If the ellipse is small, the correction is negligible.

3.6 Multiscale Updating

We use a multiscale implementation to benefit from each scale of observation starting from the coarsest scale. On coarse scales, the number of pixels used in the estimation (number of "observations") is higher than on finer scales, which ensures a better goodness-of-fit for a given residual than on a smaller scale (or small neighborhood Ω). The flowchart of the algorithm is shown in Figure 3.3. For our applications, we have chosen the set of scales s to: 16, 12, 8, and 4 pixels. From scale s_i to scale s_{i+1}, we propagate the estimation by adding the computed residual to the current parameters:

$$\vec{\theta_{i+1}} = \vec{\theta_i} + \delta\vec{\theta_i}.$$

For scale refinement of the quality criterion Q, we use the fact that the inverse of Q can be interpreted as the variance of the error vector in the parameter space that can be simply added in the case of two independent random variable. The quality is initialized to

$$Q_0 = q_0.$$

The scale updating strategy from larger scale s_i to lower scale s_{i+1} is

$$Q_{i+1}^{-1} = Q_i^{-1} + q_{i+1}^{-1};$$

hence, Q is given by the final formula

$$Q_{final} = \frac{\prod_i q_i}{\sum_i \prod_{j \neq i} q_j}$$

In the case where the aperture reduction condition is not satisfied, there is no update neither in parameter estimation nor in quality. This updating formula improves the relative error on θ if the quality Q has improved as explained in Appendix B.1.7.

3.7 Postprocessing: Heliographic Coordinates

For the Extreme ultraviolet Imaging Telescope (EIT) sequences that are full-disc observations, we convert the velocity parameters $v_x = \delta x/\delta t$ and $v_y = \delta y/\delta t$ into heliographic coordinates to get the rotation velocity and the meridional velocity. In the applications, we only use the synodic observation. Assuming that the solar corona is a sphere with a photospheric (EIT limb) radius R, we transform the spatial coordinates into heliographic coordinates and invert the following relationships (true if $\delta\Lambda$ is small)

$$\begin{aligned}
x &= R \cos B \sin \Lambda \\
y &= R(\sin B \cdot \cos B_0 - \cos B \cdot \cos \Lambda \cdot \sin B_0) \\
\delta x &\simeq R \cos B \cos \Lambda \cdot \delta\Lambda \\
\delta y &\simeq R \cos B \sin \Lambda \cdot \cos B_0 \cdot \delta\Lambda
\end{aligned}$$

where x and y are the Cartesian coordinates of the plane-of-the-sky with origin at the centre of the disc, Λ is the longitude, B is the latitude, and B_0 is the heliographic latitude of the centre of the solar disc. We obtain the expression of the angular rotation using the time interval δt separating the images I_1 and I_2:

$$\omega_{\mathrm{rot}}(x, y) = \frac{\delta\Lambda}{\delta t} \simeq \frac{\delta x}{R \cos(B) \cos(\Lambda) \delta t} \ . \tag{3.22}$$

3.8 Calibration

3.8.1 Calibration and Error Prediction using Synthetic Images

We used synthetic data to predict the error of our estimations of velocity and brightness variation. For a given constraint on the parameters to estimate, the velocity vector and the brightness variation, we generated pairs of images with varying texture and additive noise that perturb the estimation. In doing so, we obtained the empirical relationship between the quality factor Q to the estimation error. These empirical rules can be used and interpreted for error prediction: if we know the quality factor of an estimation, we derive the predicted error from the empirical rule. We first model the error parameters in Equations (3.23) and (3.24):

$$\begin{aligned} \delta I_{estimated} &= \delta I_{theoretical} + \delta I_{error} \\ \delta\vec{x}_{estimated} &= \delta\vec{x}_{theoretical} + \delta\vec{x}_{error}. \end{aligned}$$

We define $\rho = \|\delta\vec{x}_{error}\|$. We prescribe the values of $(\delta x_{theoretical}, \delta I_{theoretical})$ within the range of test values, where δx_{th} is translation in one direction with varying amplitude; we estimate the empirical rules for the errors err_ρ and $\mathrm{err}_{\delta I}$ as functions of $(\delta\vec{x}_{th}, \delta I_{th})$:

$$\mathrm{err}_\rho = 10^{b(\delta x_{th},\delta I_{th})} \cdot Q^{a(\delta x_{th},\delta I_{th})} \tag{3.23}$$

$$\mathrm{err}_{\delta I} = 10^{b'(\delta x_{th},\delta I_{th})} \cdot Q^{a'(\delta x_{th},\delta I_{th})}. \tag{3.24}$$

Each of these exponents in (3.23) and (3.24) is a function of the parameters to estimate according to the model:

$$\begin{aligned} a(\delta x_{th}, \delta I_{th}) &= c_1 \cdot \delta x_{th} + c_2 \cdot \delta I_{th} + c_3 \\ b(\delta x_{th}, \delta I_{th}) &= d_1 \cdot \delta x_{th} + d_2 \cdot \delta I_{th} + d_3 \\ a'(\delta x_{th}, \delta I_{th}) &= c'_1 \cdot \delta x_{th} + c'_2 \cdot \delta I_{th} + c'_3 \\ b'(\delta x_{th}, \delta I_{th}) &= d'_1 \cdot \delta x_{th} + d'_2 \cdot \delta I_{th} + d'_3. \end{aligned}$$

The parameters found after the calibration are gathered in Table 3.1 and 3.2. After introducing the parameter α in Section 3.4, the brightness variation parameter is measured in pixel unit. The parameters of the empirical rules (3.23) and (3.24) have been found for prescribed velocity and brightness variation varying from zero to one pixel. In the future, we will study the empirical rule for parameters larger than one pixel. In Section 4.1.1, we use this error model in order to check the correctness of the estimated velocities and brightness variations.

3.8.2 Semi-artificial EIT Sequences

We also calibrated our method on semi-artificial solar sequences. We applied a displacement field to an EIT image I_1 and obtained a second image $I_{1,dr}$ using the

Table 3.1: Model for error prediction, with the parameters determined by the calibration using synthetic images.

Mode	Parameters of err_ρ: c_i (first line) and d_i (second line)		
$(\alpha, \beta) = (0.1, 0.1)$	-6.4×10^{-2}	-7.2×10^{-3}	-0.504
	0.17	2.1×10^{-2}	-7.7×10^{-1}
$(\alpha, \beta) = (1, 0.5)$	-0.39	1.69	-0.31
	1.63	-4.13	-1.07

Table 3.2: Model for error prediction, with the parameters determined by the calibration using synthetic images.

Mode	Parameters of $\mathrm{err}_{\delta I}$: c'_i (first line) and d'_i (second line)		
$(\alpha, \beta) = (0.1, 0.1)$	-8.16×10^{-2}	-1.1×10^{-2}	-2.4×10^{-1}
	8.9×10^{-2}	1.7×10^{-2}	-1.82
$(\alpha, \beta) = (1, 0.5)$	-0.054	-0.24	-0.18
	0.155	0.73	-2.44

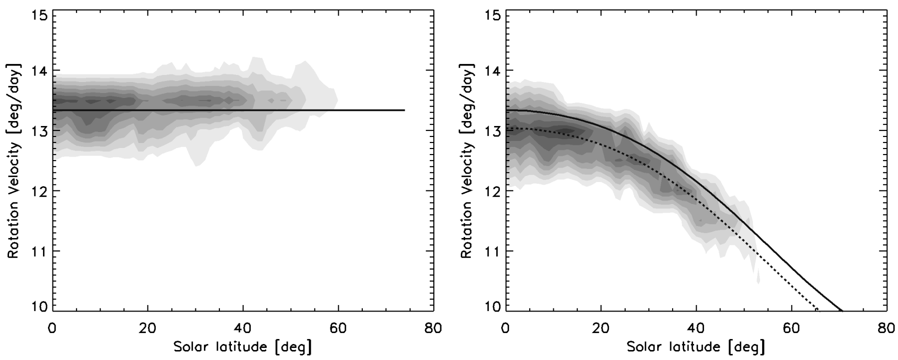

(a) Rigid rotation. (b) Differential rotation.

Figure 3.6: Calibration using *semi-artificial* EIT sequences on which a synthetic rotation has been applied for a rigid rotation (plain line in Figure (a)) and a differential rotation (Figure (b)). Vertical axis: synodic rotation velocity (in degree per day). Horizontal axis: solar latitude (in degree). The grey level represents the density of solar-disc pixels according to their latitude and estimated rotation velocity. In Figure (b), the plain line represents the differential rotation found by Vršnak *et al.* [106]. The dotted line follows the maximum density of pixels: it shows that the differential rotation measured by the algorithm has a small bias (-0.3 degree per day).

parametric models of rigid and differential rotation estimated by Vršnak *et al.* [106]. The interpolation procedure is based on the IDL function of cubic interpolation [78]. This method uses cubic polynomials to approximate the optimal *sinc* interpolation function. Due to spatial aliasing, this gives bad results when there are high spatial frequencies since it assumes that the signal is band-limited [25]. This effect lowers the similarity term S, since the image pattern is not correctly deformed, and the simple model of deformation (local translation and constant BV) is no longer valid. The measurements are then projected back into rotational motions and meridional motions. In Figure 3.6 we compare the extracted rotation velocity with the curve of the theoretical rotation. Each bin is 0.5 degree-per-day wide and 1 degree in latitude high. The relative dispersion around the theoretical rotation is approximatively ± 0.5 degree-per-day (± 5 %). This value is to be compared with the dispersion that we find on real sequences (Section 5.2.4).

3.8.3 Validation of SOFA and Aperture Reduction

The Symmetric Optical Flow Analysis (SOFA) analysis is a regularization against noisy estimation, but also regularizes the flow estimation against occultation which act as temporal irregularities of the image signal. In Figures 3.7 and 3.8, we present a study showing the successive effect of the symmetric approach (SOFA), and then of the aperture regularization for several values of the β parameter. The algorithm is applied to a synthetic sequence (see Figures 3.7a and 3.7b) containing two moving object labeled 1 and 2, moving at velocities $(1, 0)$ and $(2./3, 0.4)$ in pixel unit, on top of a static background region labeled 3. For each method used (basic Lucas-Kanade LK, SOFA, SOFA with $\beta = 0.1$, SOFA with $\beta = 0.5$), we compute the Mean Square Error (MSE) of the velocity estimated on each of the three regions $R = 1, 2, 3$ using the following formula:

$$MSE(R) = \frac{1}{N} \sum_{x \in R} \|\vec{v}(x) - \vec{v}_{th}\|^2$$

where N is the number of pixels in R. In Figure 3.7, the velocity MSE of region 3 (dashed curve) decreases because of the symmetric approach, and further more when applying the aperture reduction. The MSE curve of objects 1 and 2, showing a similar profile, tends to be stabilized until the β value gets too high causing an increase of the estimation bias caused by the regularization effects. For a noise of MSE level 0.01, the resulting velocity fields are shown on top of the first image in Figure . The regularization against aperture effect, and the symmetric approach when the regularization plays a role (see Section 3.2), tends to lower the absolute value of the estimation.

As noted by [35], a biased estimation "*will not correctly estimate the speed or direction of patterns where the local uncertainty is large. This has the benefit that*

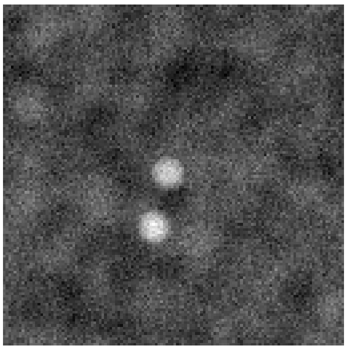

(a) First image of the synthetic sequence

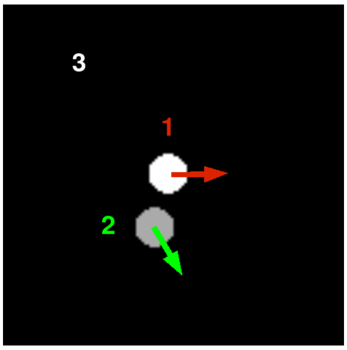

(b) Synthetic motion pattern

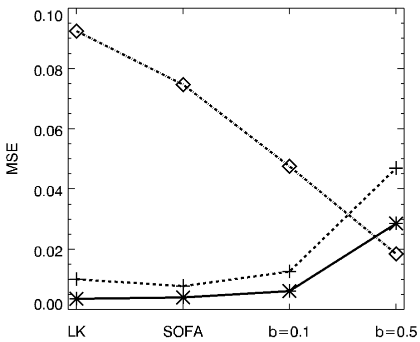

(c) noise RMSE = 0.01

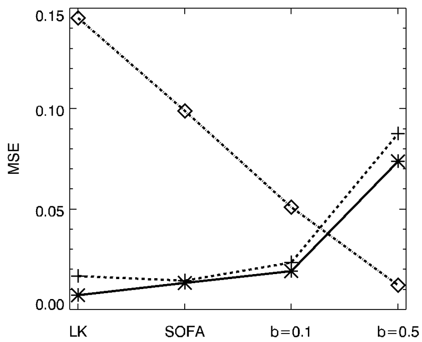

(d) noise RMSE = 0.02

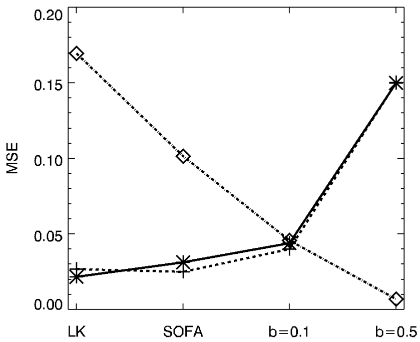

(e) noise RMSE = 0.03

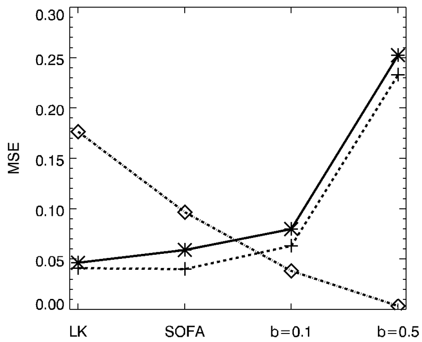

(f) noise RMSE = 0.04

Figure 3.7: Estimation of optical flow on a synthetic sequence for three different noise levels. In Figures 3.7c to 3.7f, $\star$ (solid line): object 1, + (dashed line) object 2, $\diamond$ (dashed-dotted line): background (region 3) with no signal.

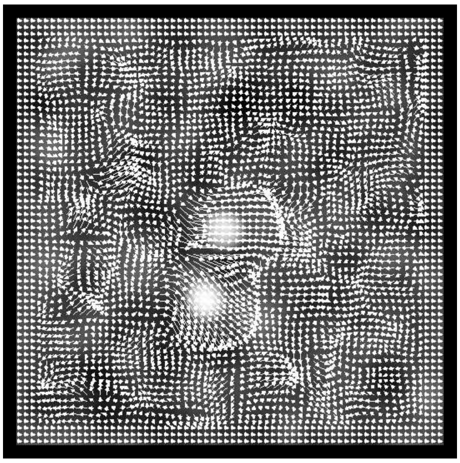

(a) Lucas-Kanade.

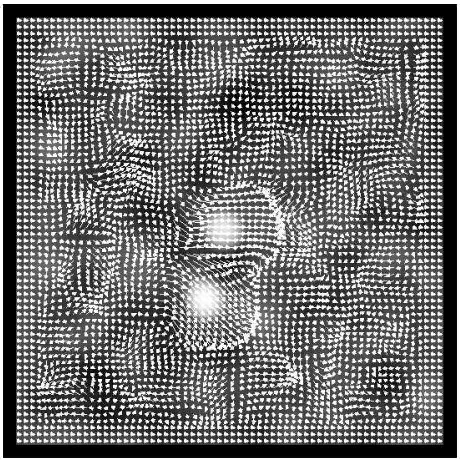

(b) SOFA with aperture reduction parameter $\beta = 0$.

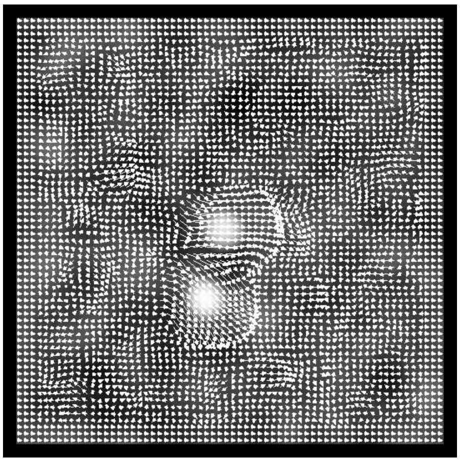

(c) SOFA with aperture reduction parameter $\beta = 0.1$.

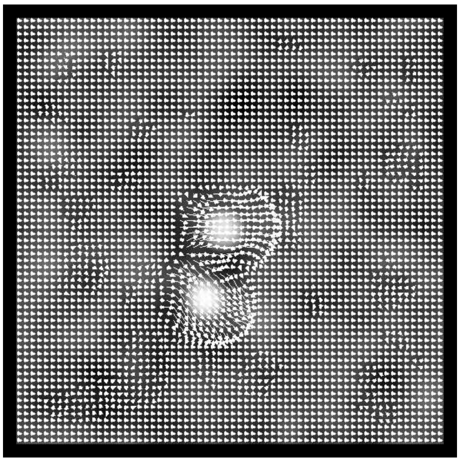

(d) SOFA with aperture reduction parameter $\beta = 0.5$.

Figure 3.8: Optical flow estimation with symmetry constraint and different aperture reduction parameters.

it dampens the estimate [in uncertain regions] to help avoid divergence in iterative refinement and tracking".

3.9 Discussion of the Algorithm

Optical flow estimations using a gradient-based approach have inherent limitations. In particular, strong spatial variations in the signal intensity introduce an error into the gradient computation if the signal is undersampled, and the optical flow estimation may be unstable. In that case, the gradients are dissimilar in both images. The SOFA constraint, which measures the dissimilarity between gradients in the two images, will then regularize the estimation (implying $\delta\vec{\theta} \to 0$ in Section 3.6) to prevent unstable estimation. In EUV images of the corona, the loops appear smooth, but brightenings or Point-like Structures (PLS) present strong small-scale intensity variations that may suffer from this effect in the optical flow estimation.

The requirement on the spatial resolution is given by the smallest neighborhood Ω of the multiscale process. If there are several moving objects smaller than the lowest scale (4 pixels here) within the neighborhood, the estimated motion will be a "mean motion" of these objects.

The requirement on the temporal resolution is given by the maximum size of the vector that can be estimated. Indeed if the optical flow vector to estimate is too large, the spatial gradients at a given pixel location in I_1 and I_2 will differ. The condition on the maximal movement measured by a gradient-based OF approach is that, over the displacement range δx, the slope ∇I must be uniform; in other words, this condition of gradient uniformity ensures that the second-order (Hessian matrix, see appendix), and even higher-order, terms of the OF residual vanish over the displacement range. If the motion is too large, and the gradients of both successive signals are different, the symmetry constraint will again penalise the optical flow estimation thereby preventing unstable computation.

There is no such condition on the brightness variation estimation, and the only encountered limitation occurred on small-scale and strongly-peaked brightness variations. This is due to the size of the smallest neighborhood, which is too large for such variations. Unfortunately, we cannot use smaller neighborhoods since the variance estimation then becomes too high (too few pixels, *i.e.* too few equations in the linear system). It is possible that the aperture reduction permits use of even lower neighborhood size, but it has not been assessed yet.

Algorithms exist that extend optical flow to more than two images, but we think that it is better to choose the simplest motion model (local translation over the time difference gap, 12 minutes in the case of EIT images), as we did, and to postprocess the results to build trajectories, by linking the successive displacements when they are reliable. This post-processing can be applied to the detection of oscillations of features in the sequence.

The adaptation of *Velociraptor* to sequence of more than two frames is explained in Chapter 5, as well as the method of automatic detection and analysis of oscillating features.

Chapter 4

Probing of Solar Dynamics in EUV Sequences of the Corona Using Optical Flow

The *Velociraptor* algorithm is designed to analyze the Extreme Ultraviolet (EUV) images of the solar atmosphere, such as the Extreme ultraviolet Imaging Telescope (EIT) and Transition Region and Coronal Explorer (TRACE) database. STEREO analyzes and 3D reconstruction will be presented in Chap. 6. Given a pair of frames and its difference image, the algorithm can disentangle the motion effect from the brightness variation map caused by variation of the source of EUV emission. It is also able to identify coronal events as regions exhibiting a significant brightness variation or an outstanding velocity field. This tracking approach may serve as a new way of analyzing the differential rotation measurement technique. The range of potential interests includes but also extends beyond ondisc signatures of flares and Coronal Mass Ejection (CME). It encompasses for example studies of nanoflares and macrospicules, coronal seismology, Magnetohydrodynamics (MHD) and EIT wave investigations.

We demonstrate a new differential rotation measurement and identify coronal events as outliers to the differential rotation or as regions exhibiting a significant Brightness Variation (BV). We apply the algorithm to EIT sequences of May 3, 1998 and April 17, 1999, and to a TRACE sequence of July 14, 1998. We discuss the analysis of solar observations in Section 5.2.4.

4.1 EUV Two-frame Analysis

We have defined a number of sequences of the solar atmosphere that show typical phenomena similar to the events mentioned in Chapter 1.

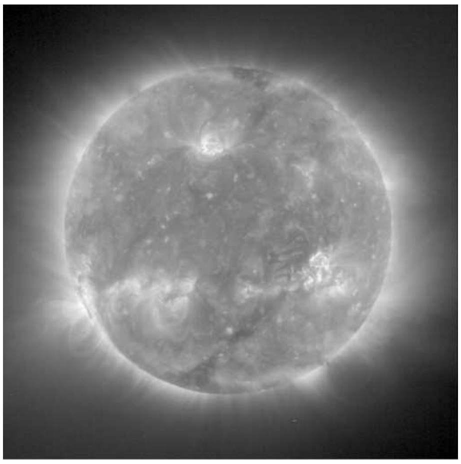

a. First EIT image

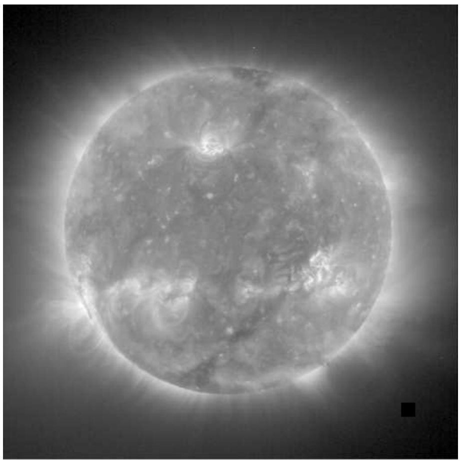

b. Second EIT image

Figure 4.1: Sequence of two EIT images

In this section, we present the processing of three pairs of images: (I_1,I_2), (J_1,J_2), and (K_1,K_2). The images I_1 and I_2 were observed by EIT on 1999-04-17, respectively, at times 00:00:11 and 00:36:10 in the CME watch mode, at the wavelength 19.5 nm. The second EIT sequence (J_1, J_2) was observed on 1998-05-03, respectively at times 21:12:09 (J_1) and 21:25:35 (J_2). We ran the algorithm on rebinned images with a resolution of 512×512 pixels. The last sequence is a pair of TRACE images observed on 1998-07-14 at times 12:50:16 (K_1) and 12:52:46 (K_2) in the 17.1 nm passband, with a resolution of 768×768 pixels. EIT images were processed using the eit_prep IDL procedure of the SolarSoft and cleaned of cosmic rays. TRACE images were processed using the trace_prep IDL procedure of the SolarSoft; they were cleaned of cosmic rays, destreaked, and derippled.

4.1.1 EIT Sequence 1 (EIT1)

We analyzed the rotation on a sequence taken on 1999-04-17 in the EIT 19.5 nm bandpass during a CME Watch observation campaign. The images were observed at 1999-04-17T00:00:11 and 1999-04-17T00:36:10. We analyze the sequence (I_1, I_2) in the same conditions as in Section 3.8. We choose the following parameters: $\beta = 0.1$ ("weak" aperture reduction) and $\alpha = 0.1$. In Figure 4.2, the subsampled resulting velocity is displayed. Figure 4.3a shows the rotation velocity of all on-disc pixels, while in Figure 4.3b we select the pixels that have the most reliable estimation ($\|\delta\vec{x}\|/\|\delta\vec{x}_{error}\|$, see Figure 4.4a), according to their latitude and their velocity rotation ω_{rot}. The selected pixels are shown in Figure 4.4a. We also plot the theoretical rotation (plain line). The estimated velocities are variable (up to $\pm$ 2 degrees per day, $\pm$15 %). Figure 4.8 shows the model $-(\vec{\nabla} I_m \cdot \vec{\delta x} + \alpha \delta I)$ of the difference image I_d (Figure 4.5) that is provided by the algorithm. This model has a variance of

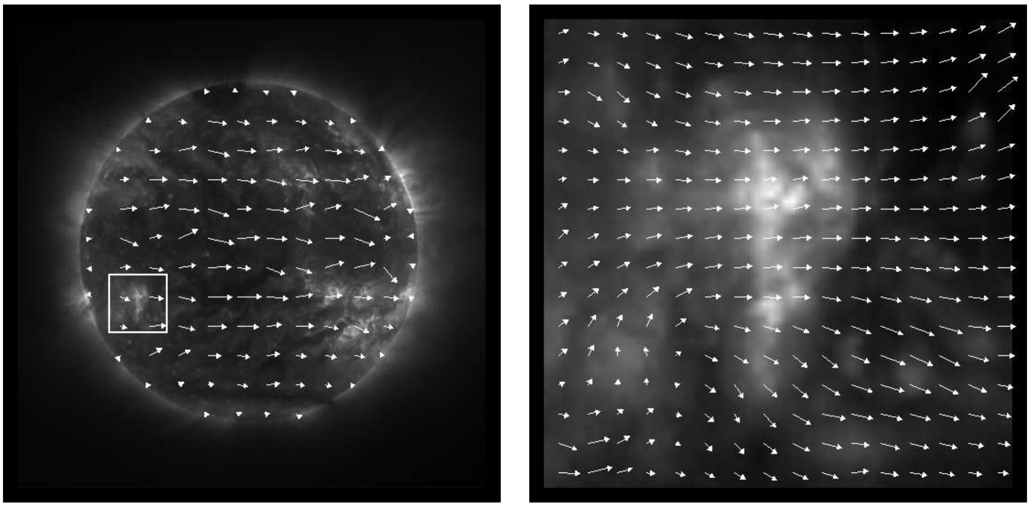

Figure 4.2: EIT1. Left: on-disc subsampled velocity field $(\delta x, \delta y)$ for the couple of images (I_1, I_2). Right: zoom showing the active region.

7×10^{-4}, lower than the variance of the difference image (9.2×10^{-4}), but it has the same order of magnitude (76% of the difference image variance). The modeled difference image (Figure 4.8) is the sum of $-\vec{\nabla} I_m \cdot \vec{\delta x}$, caused by the velocity (59% of the difference image variance, see Figure 4.6) and of $-\alpha\delta I$ caused by the brightness variation (41% of the difference image variance, see Figure 4.7). Figure 4.4b shows the two regions R1 (left) and R2 (right) extracted from the thresholded BV map $\alpha\delta I > 0.14$. We choose this threshold from analysis of the BV histogram. We use the error prediction to derive the mean values of $\mathrm{err}_{\delta I}$ over regions R1 and R2, which are 0.007 and 0.006, respectively. Finally, we obtain (units are in DN):

$$\begin{aligned} \mathrm{mean}(\mathrm{bv}(R_1)) &= -0.206 \pm 0.006 \ , \\ \mathrm{mean}(\mathrm{bv}(R_2)) &= 0.166 \pm 0.009 \ . \end{aligned}$$

The remaining residual is shown in Figure 4.9 (variance: 9.35×10^{-5}). Furthermore, one can use the BV map (Figure 4.7) to study what could be a bright front above the dimming. The positive aspect of this technique is that it does not use any compensation for rotation using an interpolation.

At high resolution (1024×1024 pixels), we applied the same algorithm using the same neighborhood sizes. We found, as expected, that the residual and model maps appear sharper (Figs. 4.10 and 4.11). The variance of the model is 1.4×10^{-3}, which is 78% of the difference image variance. The ratios between residual variance and the difference image variance are the same at both resolutions (10%). The sum of the model and the residual explains 86% of the difference image variance at low resolution and 88% at high resolution. The coefficients of correlation between the model and the difference image are the same at both resolutions ($\rho = 0.95$). The coefficient

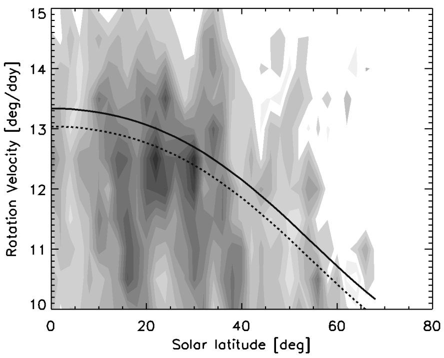

(a) All pixels.

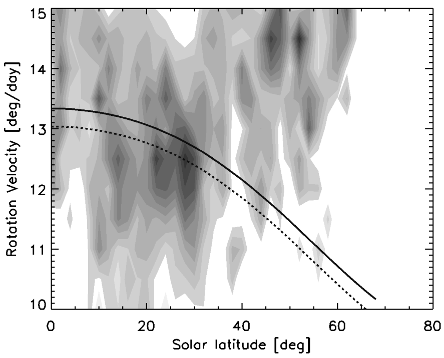

(b) Selected pixels.

Figure 4.3: EIT1. Figure (a): rotation for all pixels located on the solar disc for (I_1, I_2). The grey value represents the density of pixels. There is high variability around the theoretical differential rotation. Figure (b): rotation estimated for pixels with a high $\|\delta\vec{x}\|/\|\delta\vec{x}_{error}\|$ ratio (> 5). In Figs. (a) and (b), each column (or band of latitude) is normalised so that black means 100% of the latitude band, while white means 0%. The plain line represents the differential rotation found by Vršnak *et al.* [106]. The dotted line shows the bias found on the semi-artificial EIT sequence. In Figure (b), the velocity of the estimated pixels has a high level of confidence according to our error prediction. At the highest available latitude (> 40 degrees), the rotation velocity of most pixels is higher than expected.

of correlation between the model and the residual is $\rho = 0.25$ at the 512 pixel resolution, and lower ($\rho = 0.23$) at the 1024 pixel resolution, which confirms a better decomposition of the data I_d into the model and the residual at high resolution. The algorithm will be applied on full resolution data when the code is optimised.

4.1.2 EIT Sequence 2 (EIT2)

We analyzed a brightness variation occurring on 1998-05-03, at times 21:12:09 (J_1) and 21:25:35 (J_2) in the CME Watch mode, at the passband 19.5 nm. The original image J_1 is shown in Figure 4.12a. In the difference image J_d (Figure 4.12b), there is a strong brightness variation. For this application, we chose the aperture reduction mode: $\beta = 0.5$ and $\alpha = 1$. In the particular region where we focus the study (see Figure 4.12a), it appears clearly from both the velocity field (Figure 4.13) and the brightness variation map (Figure 4.12b) that the algorithm is able to carry out a correct interpretation of the difference image, confirmed by a visual inspection. The motion of the loop is detectable in Figure 4.13 in the middle of the image. This mode increases the bias, so that the parameters, e.g. the velocity vector, is underestimated. For this reason the predicted error is also pessimistic. Nevertheless it is possible to

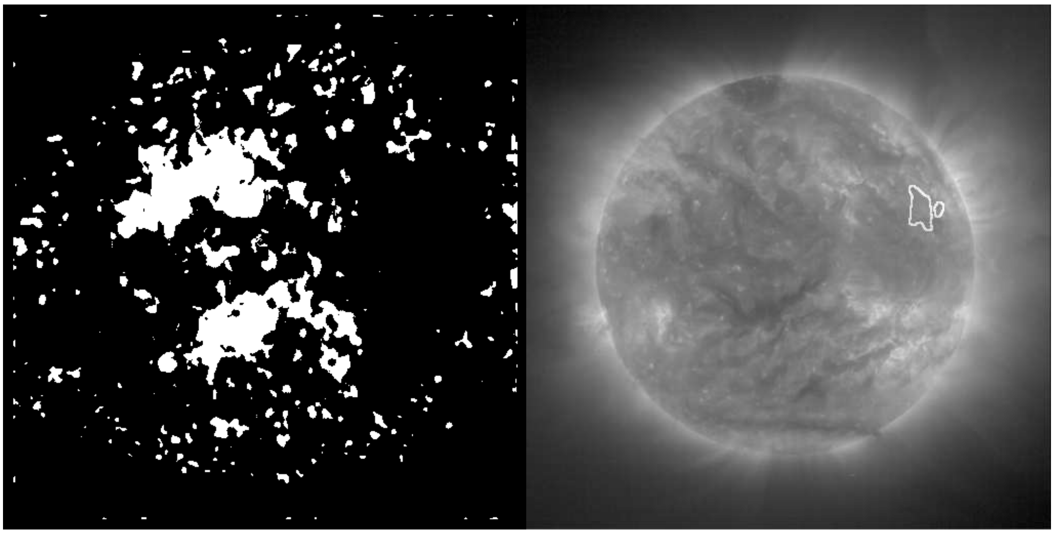

(a) Map of selected pixels (b) First image I_1

Figure 4.4: EIT1. Left: map of selected pixels according to the criterion $\|\delta\vec{x}\|/\|\delta\vec{x}_{error}\| > 5$. The error prediction ensures that the selected pixels have reliable velocity estimations. Right: first image I_1 with two regions R1 and R2 extracted from thresholded BV map $\alpha\delta I$.

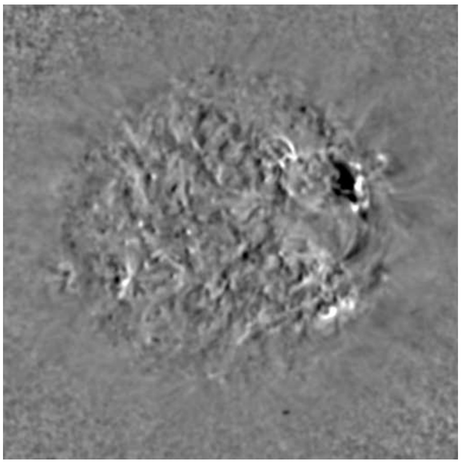

Figure 4.5: EIT1. Difference image for the sequence (I_1, I_2) at the 512 pixel resolution. The variance is 9.2×10^{-4} at the 512 pixel resolution, and 1.8×10^{-3} at the 1024 pixel resolution.

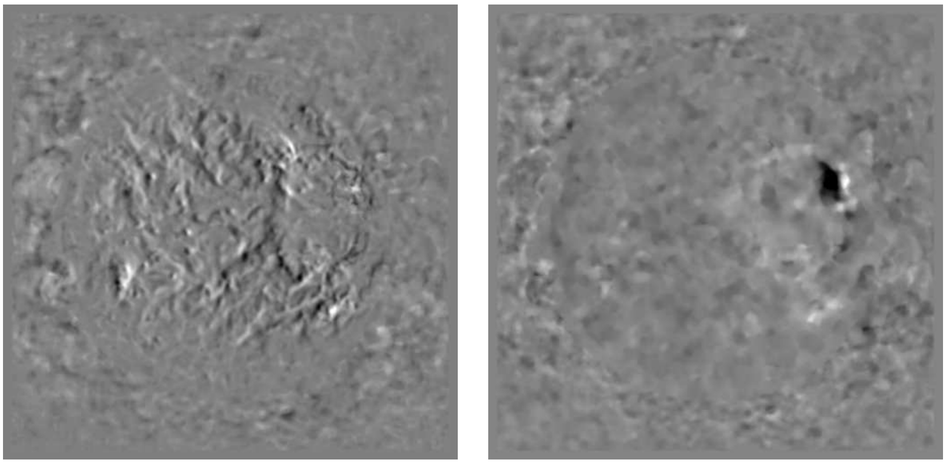

Figure 4.6: EIT1. (a) Proportion of difference image interpreted as motion for the sequence (I_1, I_2). This is the quantity $-\vec{\nabla} I_m \cdot \vec{\delta x}$ at the 512 pixel resolution. The variance is 5.4×10^{-4}. (b) Proportion of difference image interpreted as brightness variation for the sequence (I_1, I_2). This is the quantity $-\alpha \delta I$ at the 512 pixel resolution. The variance is 4.2×10^{-4}.

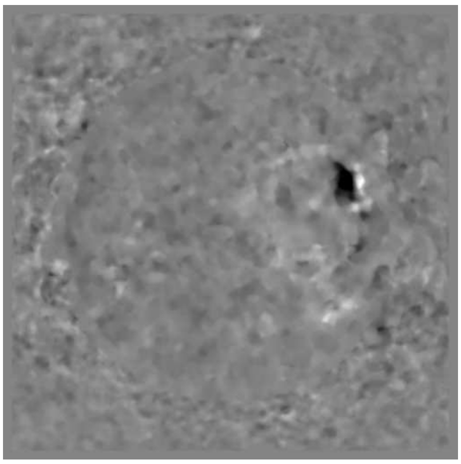

Figure 4.7: EIT1. Proportion of difference image interpreted as brightness variation for the sequence (I_1, I_2). This is the quantity $-\alpha \delta I$ at the 512 pixel resolution. The variance is 4.2×10^{-4}.

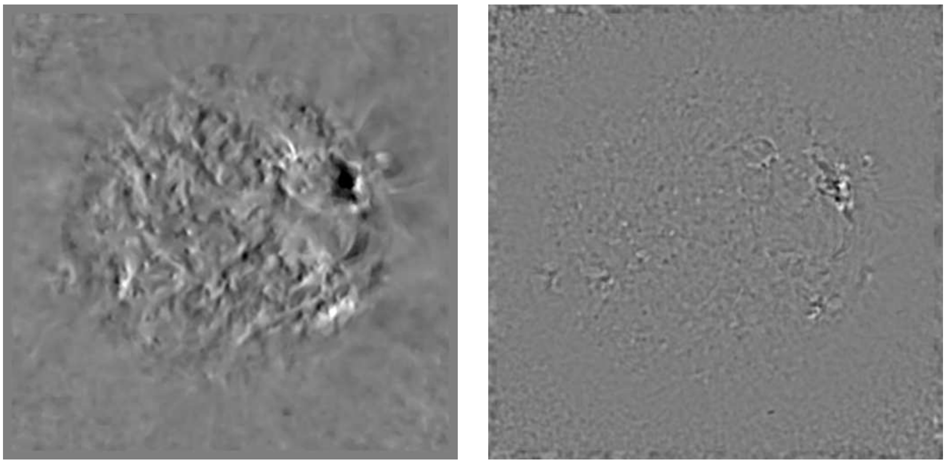

Figure 4.8: EIT1. (a) Model for difference image $I_d = I_2 - I_1$. This is the quantity $-(\vec{\nabla} I_m \cdot \vec{\delta x} + \alpha \delta I)$ at the 512 pixel resolution. The variance is 7×10^{-4}: the model interprets 76% of the data (the difference image). (b) Residual for the sequence (I_1, I_2). This is the quantity $I_d + \vec{\nabla} I_m \cdot \vec{\delta x} + \alpha \delta I$ at the 512 pixel resolution. The variance is 9.35×10^{-5}: it means that 10% of the variance of data (the difference image) is interpreted as residual.

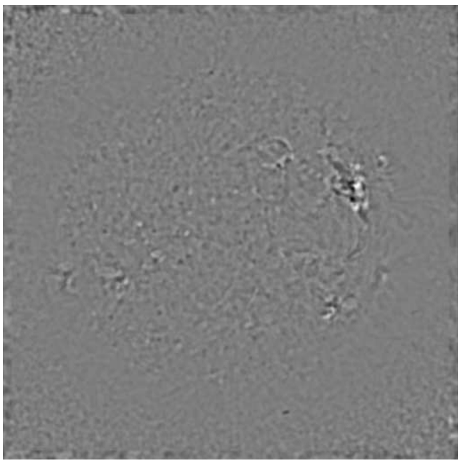

Figure 4.9: EIT1. Residual for the sequence (I_1, I_2). This is the quantity $I_d + \vec{\nabla} I_m \cdot \vec{\delta x} + \alpha \delta I$ at the 512 pixel resolution. The variance is 9.35×10^{-5}: it means that 10% of the variance of data (the difference image) is interpreted as residual.

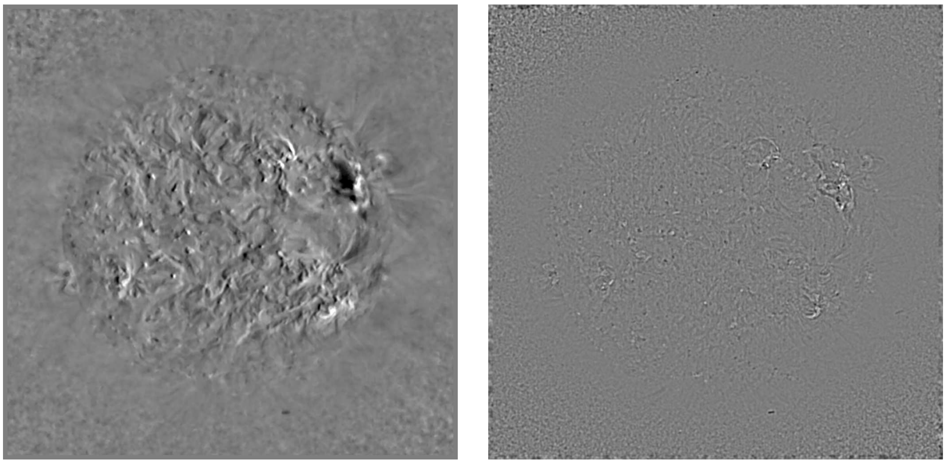

Figure 4.10: EIT1. (a) Model for difference image $I_d = I_2 - I_1$. This is the quantity $-(\vec{\nabla} I_m \cdot \vec{\delta x} + \alpha \delta I)$, but in the high-resolution case (1024×1024 pixels). The variance is 1.4×10^{-3} (78% of the difference image variance). (b) Residual for the sequence (I_1, I_2). This is the quantity $I_d + \vec{\nabla} I_m \cdot \vec{\delta x} + \alpha \delta I$, but in the high-resolution case (1024×1024 pixels). The spatial resolution of the residual is higher than at the 512 pixel resolution. The variance is 1.8×10^{-4} (10% of the difference image variance). The sum of the model and the residual explains 88% of the difference image variance.

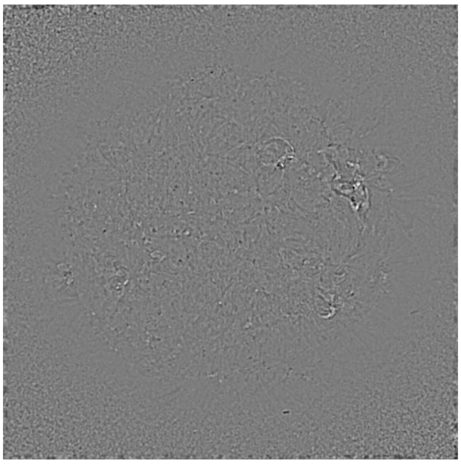

Figure 4.11: EIT1. Residual for the sequence (I_1, I_2). This is the quantity $I_d + \vec{\nabla} I_m \cdot \vec{\delta x} + \alpha \delta I$, but in the high-resolution case (1024×1024 pixels). The spatial resolution of the residual is higher than at the 512 pixel resolution. The variance is 1.8×10^{-4} (10% of the difference image variance). The sum of the model and the residual explains 88% of the difference image variance.

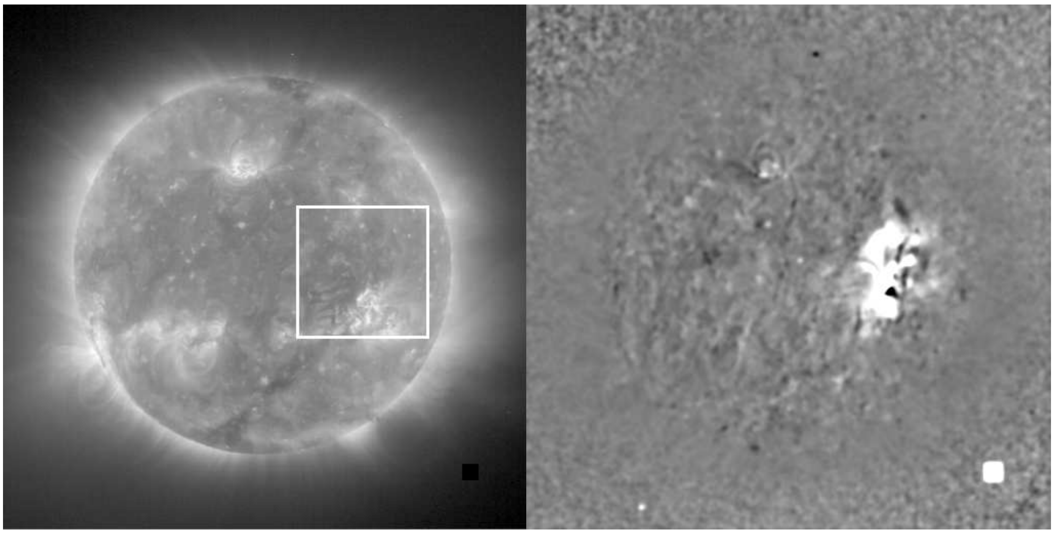

(a) First image J_1 (b) Difference image J_d

Figure 4.12: EIT2. Left: first image J_1 showing the location of a strong brightness variation at the 512 pixel resolution. Right: difference image $J_d = J_2 - J_1$ at the 512 pixel resolution. The variance is 2.94×10^{-3}.

choose detection thresholds to automatically identify this event. In that case, the full difference image J_d (Figure 4.12b) is only partly explained quantitatively by the model $-(\vec{\nabla} J_m \cdot \vec{\delta x} + \alpha \delta J)$: indeed it represents 44% of the variance of J_d. Both terms of the model undergo the strong correction that biases the parameters, but here the difference image has been explained mostly by brightness variation. We also show in Figure 4.16 the measurement of the rotation when the two high-quality pixels selections by bins and whose density is represented in linear scale. It shows that, although the rotation is retrieved from this motion measurement (coefficient A), the selection of the pixels using the quality does not allow in these examples to give precise information on the differential rotation (measurement of coefficient B).

4.1.3 TRACE Sequence and Oscillation Tracking

The TRACE images K_1 and K_2 are observed on 15 April 2001 at times 12:50:16 (K_1) and 12:52:46 (K_2), respectively. For this application, we chose the strong correction mode: $\beta = 1$ and $\alpha = 1$. It is adapted to measuring the velocities in the normal direction of the loop. The original image with the region of interest is shown in Figure 4.14a. The global shift motion is estimated with coarse full-image cross-correlation and then introduced as an initial velocity vector to the algorithm. Again, in this case, the difference image (Figure 4.15a) is not completely explained by the model (Figure 4.15b), which explains 29% of the difference-image variance.

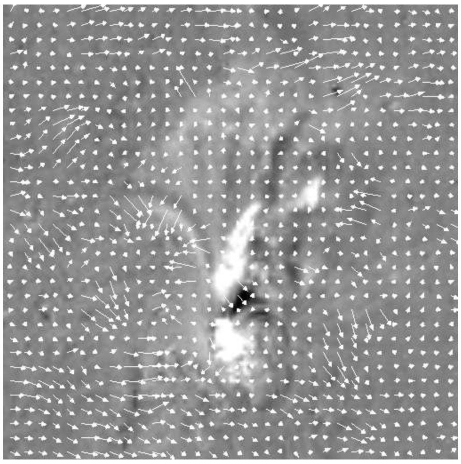

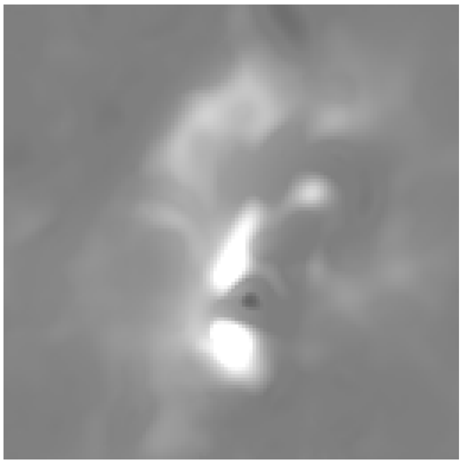

Figure 4.13: EIT2. (a) Zoom on difference image (no smoothing) with velocity field $\delta\vec{x}$ superimposed. The loop motion in the middle of the image can be clearly identified. (b) Zoom on the brightness variation map $-\alpha\delta J$. The brightness variations that dominate in the difference image are correctly identified as such on the brightness variation map.

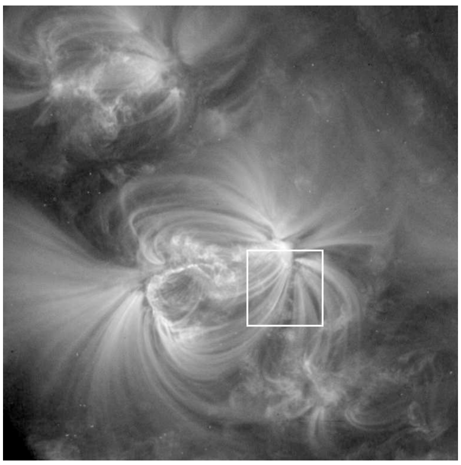

(a) Image of K_1 showing the location of the region of interest. The resolution is 768×768 pixels.

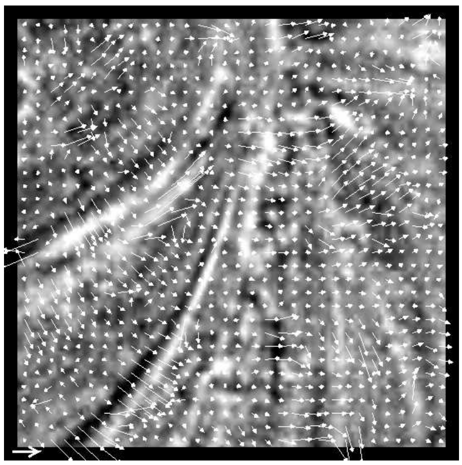

(b) Zoom on the region of study for the sequence (K_1, K_2). The subsampled velocity field is superimposed on the difference image. The arrow in the lower left corner represents a displacement of one pixel.

Figure 4.14: TRACE image and zoom.

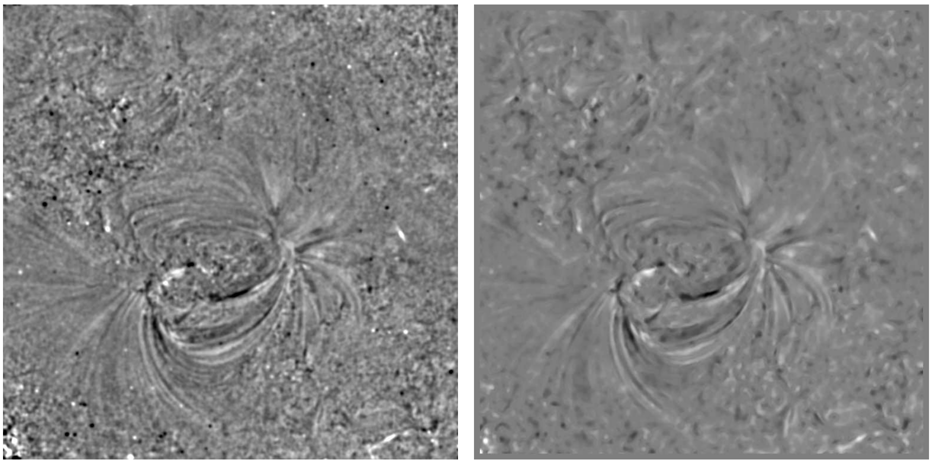

(a) Difference image $K_d = K_2 - K_1$.

(b) Model of difference image $K_d = K_2 - K_1$.

Figure 4.15: TRACE. (a) Difference image $K_d = K_2 - K_1$. The variance is 1.36×10^{-3}. (b) Model of difference image $K_d = K_2 - K_1$. This is the quantity $J_d + \vec{\nabla} J_m \cdot \vec{\delta x} + \alpha \delta J$. The variance is 4×10^{-4}.

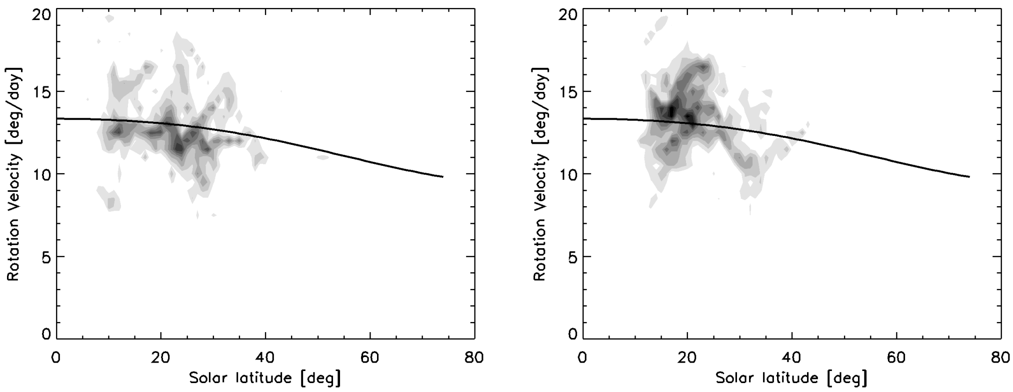

a. bin of quality q

b. bin of highest quality q+1

Figure 4.16: Density of solar disc pixels as a function of synodic rotation velocity (ordinate) and latitude (abscissa) for quality levels 4 and 5.

The velocity term of the model seems to overlap the moving loops of the active region. The strong aperture reduction mode ensures that these loops are oscillating, although we still have to analyze the error prediction in detail. On the other hand, the brightness variation map covers some part of the active region but also operates over all the Quiet Sun. We focus the study on a region located at the footpoints of the active region loops (Figure 4.14a). The velocity field superimposed on the difference image is shown in Figure 4.14b for this region: the loop oscillation is observable from this sequence of two images. The estimated velocities can be used for detecting and measuring the loop oscillation with precision.

4.2 Discussion

We have demonstrated the ability of our optical flow algorithm to interpret the difference image of a sequence of two EUV images as the sum of two components, one due to the motion and the second due to the brightness variation of the moving objects. Real and semi-artificial EIT sequences have been analyzed in terms of motion and brightness variations over the full solar image. A multiscale implementation refining the estimation from coarse scale to fine scales enables us to cope with complex motions. The estimation is dense (one estimation for each pixel), and the algorithm provides a quality map, which is related to the error maps. This quality factor has been calibrated on synthetic images with prescribed values of the parameters, and this calibration has given empirical rules for error prediction. The calibrated error helps in reliably distinguishing moving objects and appearance/disappearance of coronal structures in a sequence of EUV images. The model for the difference image can be used for event detection. An event can be defined as a particular motion (e.g. a loop motion in the sequence (J_1, J_2) or a strong brightness variation $-\alpha\delta J$). In the velocity maps, we observe accumulations of pixels into clusters that have a common rotation velocity. In a future work, we will study the variability in the rotation velocity of, e.g., an active region over half a rotation, which will be possible after processing longer sequences.

We plan to analyze the trends of the differential rotation over the solar cycle. Also, investigating the BV maps will allow for a better understanding of the weak dimmings and brightenings, which are concurrent with the fast motion but are merged in the difference image.

This algorithm is a scientific data-analysis tool that provides the apparent velocities and the brightness variation of any coronal events on the difference-image time scale. For instance, the processing of a long sequence will provide precise measurements of the loop oscillations observed in TRACE data. The algorithm also has the potential to achieve automatic event detection: *e.g.*, it can become a routine of oscillation detection (see Chapter 5). Automatic detection of events in sequences of two coronal EUV images can also be achieved using the BV maps, such as in the sequence of 1999-04-17 (EIT1): a brightening covering a large area has been unambiguously singled out from the regular solar signal. Moreover, we want to investigate the correlations in time between our events (fast motions, strong brightness variations), their localisations, and high corona signals (LASCO CMEs and in-situ Advanced Composition Explorer (ACE) data).

Ultimately, the software will achieve online computation and automatic interpretation of EUV movies of the solar corona, and the outputs will be ready to be assimilated by physical models and data assimilation processes. The presented optical flow algorithm leads to solar physics research, as well as to real-time space weather services.

Chapter 5

Tracking of Solar Extreme Ultraviolet Features

We have presented in Chapter 3 an algorithm able to estimate motion and brightness variation from a pair of solar images. We shall here combine it with a tracking algorithm (Section 5.1) in order to detect and analyze coronal loop transverse oscillations. We also apply the tracking algorithm to the synoptic mode of the Extreme ultraviolet Imaging Telescope (EIT) instrument (4 images per day); the results allow us to analyze the differential rotation of the Sun and thus complete our knowledge of this phenomena (see Section 1.2.4). Some part of this chapter dealing with oscillation tracking (Section 5.2) has been partially published in [39]. For all what concerns the wavelet transforms mentioned in this chapter, we refer to Appendix A.

5.1 Tracking over more than Two Images

In the sequences of Extreme Ultraviolet (EUV) images, our objective is to track features such as bright points, loops and point-like objects. These objects undergo the motions which stems from physical phenomena described and detailed in Chapter 1. Instead of tracking all pixels in a sequence of images, one can achieve detection of moving features at a lower computation time by choosing the best possible features to track. There exist several different criteria for extracting features to track; in solar EUV images, we aim to track bright points and other point-like structures, as well as detecting and analyzing loop oscillations. In [97] corner-like objects are extracted and tracked over time, corners are defined as highly textured region according to the structure of the spatial gradient. A dense motion field may be obtained by increasing the density of features and by interpolating the sparse motion field.

5.1.1 Feature Selection

Bright points and point-like structures can be identified as tracers, or features (we will use both names to denote the objects to track), and they might be identified in our applications by a pixel that we track in sequences of images. The selection of the features will depend on the application. A tracking of all pixels contained in the images would be preferable, but is difficult to achieve because of the time of computation. From the optical flow analysis, bright points can be selected as corners in the (x,y) or in the $(x,y,\delta I)$ parameter space, or as a local maxima of a smoothed version of the image. Loops, prominences, and possibly coronal hole edges are elongated features and can be tracked more reliably along the normal direction to these features.

5.1.2 Tracking Method

In order to lower the computation time, we choose features that can be reliably tracked, rather than track all pixels. Once the features are selected, the tracking of these tracers is achieved by applying the velocity field estimated at the feature location of each existing trajectories. The trajectory is then updated by adding the new position of the feature. New trajectories are initiated for each appearing feature that is not in the vicinity of an already existing trajectory. Future applications will track all pixels, and initiate a new trajectory at each pixel that does not belong to an existing trajectory. The tracking algorithm is detailed hereafter.

In Algorithm 1, the Feature tracers are defined by the procedure of selection of the features. Each feature Feature(k,i) where k denotes the trajectory number and i is the time variable corresponding to the image number, describes the position of the tracer, but it could also include other variables describing the feature such as intensity measurerements, the instantaneous velocity, or any other quantity of interest. For each existing trajectory, the new position Feature(k,i+1) is estimated from the previous position Feature(k,i+1) using a motion estimation method that can be either the optical flow computation presented in Chapter 3 or the Local Correlation Tracking (LCT) method introduced in Section 2.3.1. The trajectory of a feature is interrupted if the quality of the tracking falls below a certain predefined value. In the case of the LCT method, the quality is defined as the correlation coefficient, while the quality of the optical-flow estimation has been defined in Section 3.4.

5.2 Detection of Loop Oscillations

In this method of oscillation detection applied to coronal loop oscillations, the features (see 5.1.1) are selected as pixels that are local maxima of the low-passed image

Algorithm 1 Build the trajectories of features in sequence of images I

Traj() {initiate the first trajectory}
for i= 1 to nbr_images-1 **do**
  Feature $\leftarrow$ features in $I(i)$
  for j= 1 to nbr_features **do**
    if Feature(j) $\notin$ Traj **then**
      Traj$\leftarrow$Traj$\cup$Traj() {add a new trajectory to Traj}
    end if
  end for
  for k= 1 to nbr_traj **do**
    Feature(k,i+1)$\leftarrow$ shifted Feature(k,i) {using motion estimation}
    $Q \leftarrow$ estimation quality of Feature(k,i+1)
    if $Q \geq$ Threshold **then**
      Traj(k,i+1) $\leftarrow$ Traj(k,i)$\cup$Feature(k,i+1)
    else
      end Traj(k)
    end if
  end for
end for

(smoothed by a Gaussian kernel). The displacement between successive positions of features is estimated using the optical-flow algorithm (see Chapter

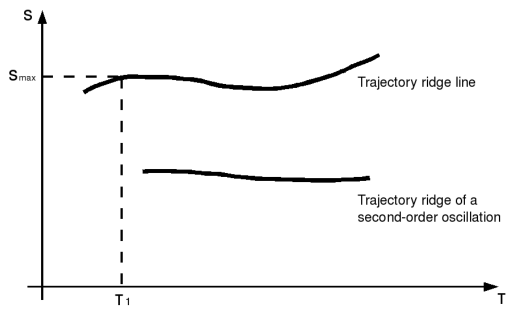

Figure 5.1: Morlet analysis of a trajectory showing a main oscillation component and a second-order oscillation.

5.2.1 Complex Trajectory

We define the trajectory as a complex value of function $z(t) = x(t) + iy(t)$, where x and y denotes respectively the horizontal and the vertical positions of a feature (Feature in Algorithm 1). In our case, the sequence has an irregular temporal sampling. We thus resample the trajectory of the feature using cubic interpolation at N locations. Using the continuous Morlet transform described in A.2.2, for a trajectory

$$x(t) = x_0 + b_x t + a\sin(k_1 t)\cos(\theta) \ , \tag{5.1}$$

$$y(t) = y_0 + b_y t + a\sin(k_1 t)\sin(\theta) \ , \tag{5.2}$$

we have

$$z(t) = ae^{i\theta}\sin(k_1 t) + b(t) \ . \tag{5.3}$$

5.2.2 Morlet Analysis of the Trajectory

The continuous Morlet transform $W_z : (b,s) \mapsto W_z(b,s)$ of the discrete signal z is given by

$$W_z(\tau, s) = \langle z|\psi_{\tau,s}\rangle = z * \psi_s^\sharp$$

where τ is the time parameter, s is the scale, $\psi_s^\sharp(\tau) = \frac{1}{s}\overline{\psi(-\tau/s)}$ in the L1 norm, and the wavelet is $\psi(\tau) = \pi^{-1/4}\exp(ik_0\tau)\exp(-\tau^2/2)$. The Morlet transform W_z removes the linear trend $b(t)$ of the motion because of its vanishing moments. The time variable is discretized as $t = \frac{n}{N}T, n = 0, N-1$ where T is the total duration of the trajectory, and N is the number of regular samples. To estimate the local oscillation period, we use the L1-normalised wavelet transform formula that gives $W_z(\tau, s)$. The letter $\mathcal{F}$ denotes the Fourier transform as explained in Section A.1. One defines the complex trajectory in the Fourier domain and its Morlet Wavelet transform as:

$$\widehat{z}[k] = \frac{1}{\sqrt{2\pi}}\int dt\ z(t)\ e^{-i\,kt}$$

so that

$$\widehat{W_{z\tau,s}}[k] = \sqrt{2\pi}\ \ \widehat{z}[k]\ \ \widehat{\psi_s^\sharp}[k]$$

which leads, in the Fourier domain, to

$$\widehat{z}[k] = a\ e^{i\theta}\frac{i\sqrt{2\pi}}{2}[\delta(k+k_1) - \delta(k-k_1)] + \widehat{b}(k)$$

where

$$z_0 = x_0 + iy_0 \text{ and } z_1 = b_x + ib_y \ .$$

The trajectory and the wavelet function is given by

$$\widehat{b}(k) \quad = \quad \sqrt{2\pi}\ \delta(k)\ z_0 + i\ \sqrt{2\pi}\ z_1\delta'(k) \ .$$

Since we have these four properties

$$\begin{aligned}
\widehat{\psi_s^\sharp}[k] &= \mathcal{F}[\psi_s^\sharp](k) = \overline{\widehat{\psi}}(sk) \ , \\
\mathcal{F}[e^{-\tau^2/2}] &= e^{-k^2/2} \ , \\
\mathcal{F}[e^{ik_0 t}f(t)] &= \widehat{f}[k-k_0] \ , \\
\widehat{\psi_s^\sharp}[k] &= \pi^{-1/4}\ e^{-1/2(sk-k_0)^2} \ ,
\end{aligned}$$

we can write

$$\widehat{W}_{z\tau,s}[k] = \sqrt{2\pi}\ \pi^{-1/4}\ e^{-1/2(sk-k_0)^2}[a\ e^{i\theta}\frac{i\sqrt{2\pi}}{2}[\delta(k+k_1)-\delta(k-k_1)]+\widehat{b}(k)]\ .$$

Since

$$\forall s>0\ ,\quad e^{-1/2(-sk_1-k_0)^2}\simeq 0\ ,$$

we derive that

$$\widehat{W}_{z\tau,s}[k]\simeq -\pi^{3/4}\ i\ e^{-1/2(sk_1-k_0)^2}a\ e^{i\theta}\delta(k-k_1)\ ,$$

and as

$$\delta(k-k_1)\overset{\mathcal{F}^{-1}}{\longleftrightarrow}\frac{1}{\sqrt{2\pi}}e^{ik_1t}\ ,$$

we can conlude that

$$W_z(\tau,s) = -\frac{1}{\sqrt{2}}\pi^{1/4}a\,i\,e^{i\theta}e^{-\frac{1}{2}(sk_1-k_0)^2}e^{ik_1\tau}\ .$$

The oscillation period is given by the formula

$$P_{max}(\tau) = 2\pi s_{max}/k_0 \text{ and } k_{1,max} = k_0/s_{max}$$

where $s_{max}(\tau) = \arg\max_s |W_z(\tau,s)|^2$.

5.2.3 Detection Method

The set of points $(\tau, P_{max}(\tau))$ defines the trajectory ridge. In the last formula, we use the wavelet power spectrum $|W_z(\tau,s)|^2$ to determine the main oscillation period. The phase of coefficient, equal to $\Phi(W_z(\tau,s)) = \pi/2+\theta+k_{1,max}\cdot\tau \bmod 2\pi$, carries the information of direction of the trajectory. In practice, the original velocity vectors also give the direction tangent to the trajectory, while the phase is more difficult to estimate precisely. We define the relative contribution of the oscillating component by

$$P_{ratio} = \frac{\sum_{\tau\in\Omega_\tau}|W_z(\tau,s_{max})|^2}{\sum_{(\tau,s)\in\Omega_W}|W_z(\tau,s)|^2}\ ,$$

where Ω_τ is the ridge line defining the trajectory restricted by the Cone of Influence (COI) of the edges and Ω_W is the whole domain inside the COI. In this work, we use the criterion

$$P_{ratio} > T_{osc} \tag{5.4}$$

where T_{osc} is an empirical threshold, to decide whether a trajectory of ridge $(\tau, P_{max}(\tau))$ oscillates or not.

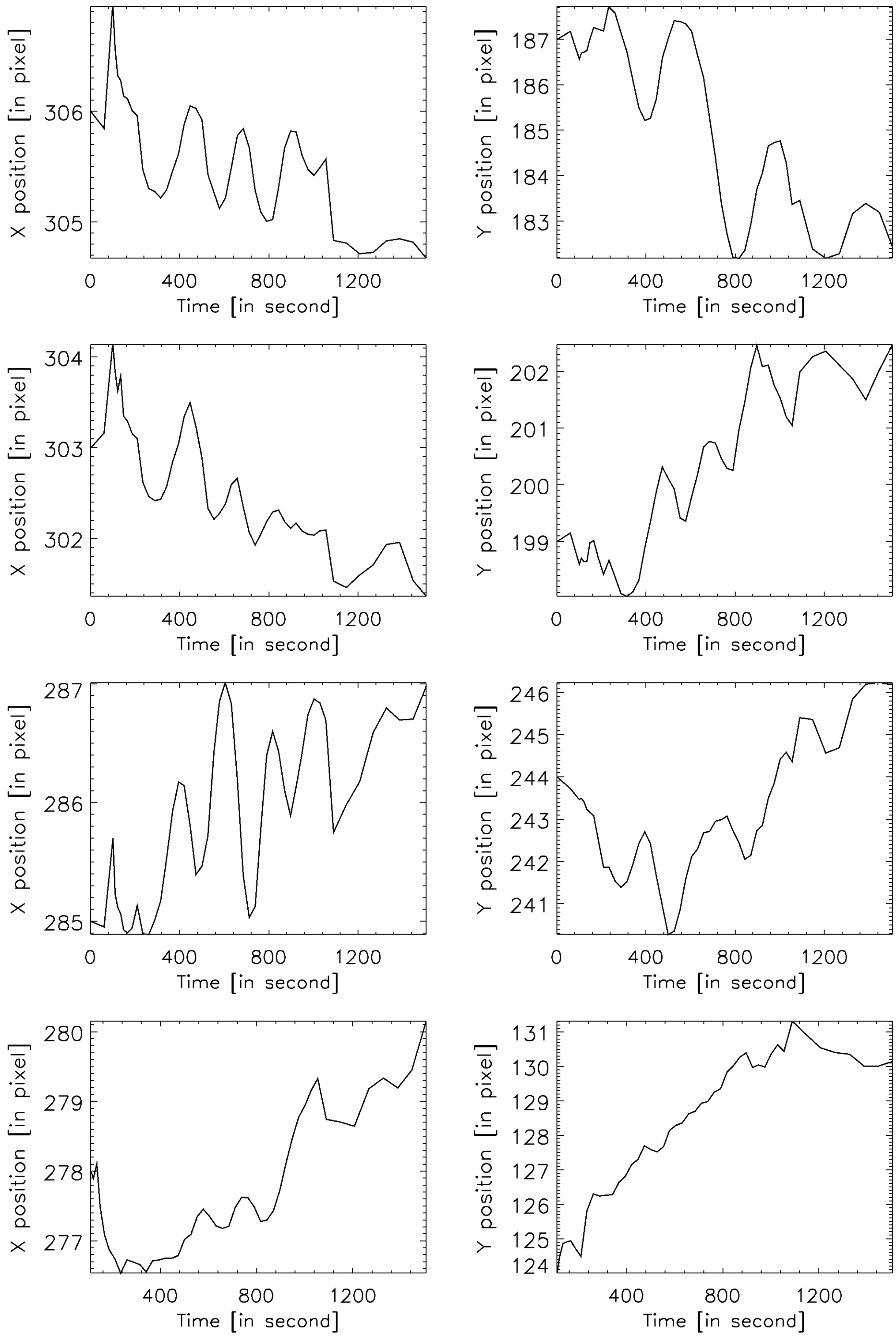

Figure 5.2: Trajectories coordinates along x (left) and y (right) axes, for trajectory 1 (upper plot) to 4 (lower plot).

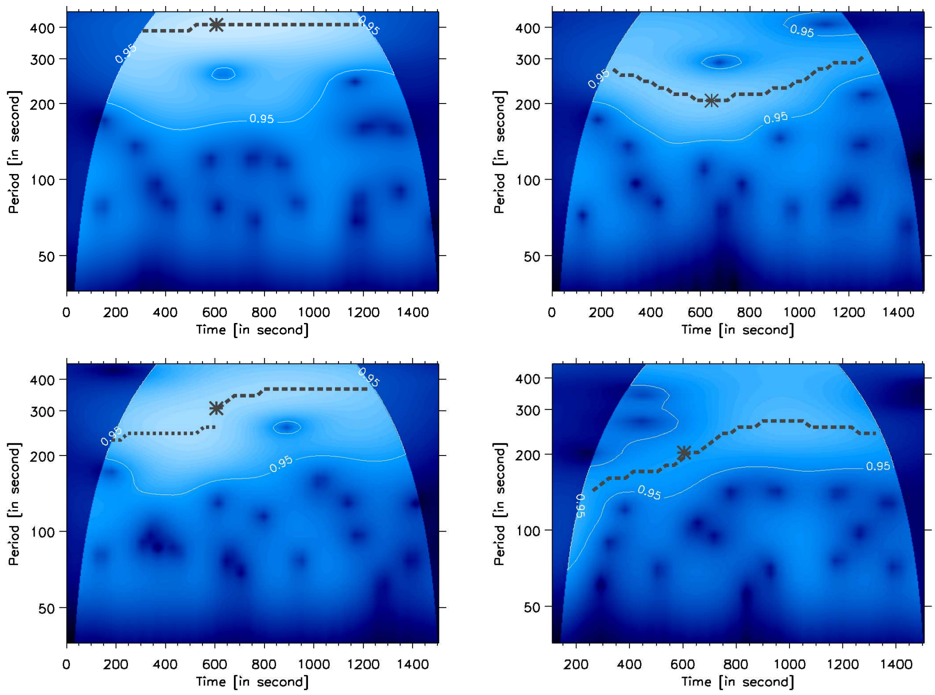

Figure 5.3: Morlet transform of trajectories 1 (upper left), 2 (upper right), 3 (lower left), and 4 (lower right). The dotted line is the trajectory selected inside the Cone of Influence (COI). A star mark plotted over the trajectory ridge indicate the frame 25 at time $\tau = 604$ seconds.

5.2.4 Results and Discussion

We applied our oscillation analysis method to a TRACE sequence observed on 15 April 2001. We choose the possible candidates for oscillating trajectories among the trajectory ridges defined by $(\tau, P_{max}(\tau))$ using the spectrum of Morlet wavelet transform. We then define the criterion for selecting the oscillating features among these trajectories. We show the Morlet wavelet transform of four different pixel trajectories (Figure 5.2), and propose a representation showing the instantaneous oscillation period, see Figure 5.3, where the dotted line shows the trajectory ridge that has been identified. A mark (star) is located at time $\tau = 604$ seconds and corresponds to the frame 25 shown in Figure 5.4. The trajectory 3 is anomalously divided into two trajectories by the automatic detection of the trajectory. Because of a numerical artifact, only the latter part of the trajectory is correctly selected. The trajectory 1 shows a second oscillation with a 200 second period that could be as well considered. In Figure 5.4, all the features appear as + or x marks: the x marks indicate oscillating trajectories selected according to the criterion (5.4). The spatial oscillations of coronal loops have been shown to be triggered by flares, and have been identified with magneto-acoustic waves that are the fast kink modes of Magnetohydrodynamics (MHD) waves. The coronal seismology consists in estimating the magnetic field strength B, since the kink-mode period P_{kink} is related to B through $B = \frac{L}{P_{kink}}\sqrt{8\pi\rho_i(1+\rho_e/\rho_i)}$ [81]. The work presented here enables precise measurements of the period P_{kink}, estimated by the quantity P_{max}, and where the other quantities, namely the loop length L, the external mass density ρ_e and the internal mass density ρ_i, are derived from physical hypotheses. The future work will consist in estimating the differential rotation in the other EIT channels and in STEREO data.

5.3 Rotation Measurements using Feature Tracking

5.3.1 Differential Rotation Measurements and Cycle Study

For this application the features are defined as the local maxima of the Continuous Wavelet Transform (CWT). In the passband that will be used in this application (30.4 nm), this definition of features has the advantage of generating a high density of tracers, at almost all latitudes of the solar disc, contrarily to other methods used so far and that are based for instance on sunspots. This approach is also motivated by the translation covariance of the CWT. If the motion is a translation, the tracking in the series of the CWT transformed object is equivalent to the tracking of the object in the series of the image. The search of the local maxima of the CWT [3] have been used to detect bright points in solar EUV images [56]. In this section, we describe our algorithm for tracking features defined as local spatial maxima of the wavelet transform at a constant scale. Here the tracking is accomplished by optical-flow

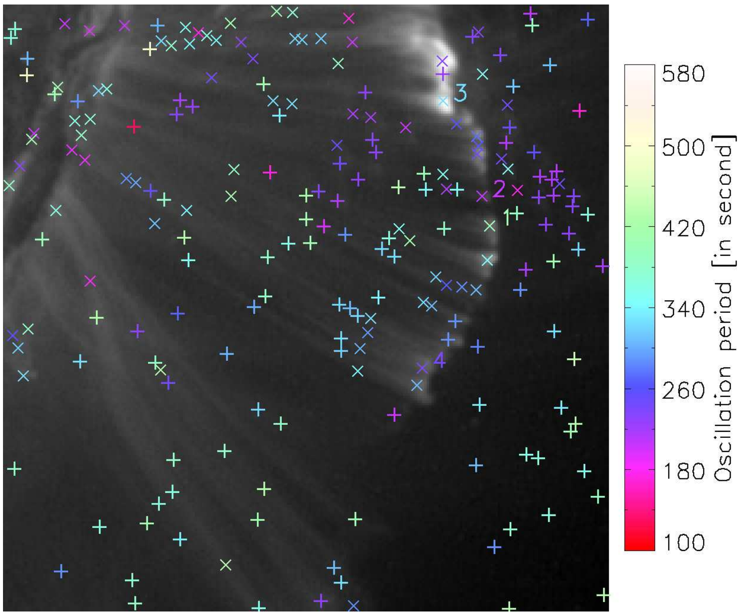

Figure 5.4: Frame 25 at time $\tau = 604$ seconds with selected features. The feature color and the colorbar on the side indicate the oscillation period of the trajectory. The x marks are the features of oscillating trajectories according to the criterion $P_{ratio} > T_{osc}$. Features marked 1 to 4 are the ones detailed in this study.

computation (see Chapter 3) at local maxima of the CWT of the sequence. Let ω be a neighborhood of $\vec{X}$ and S the spectrum of the wavelet transform. The local maxima are defined as

$$\vec{X} = \{\vec{X_j} | \forall \vec{X} \in \Omega, S(\vec{X_j}) > S(\vec{X})\} \ . \tag{5.5}$$

At each scale, the local maxima are tracked using the tracking algorithm of Section 5.1.2 in which the motion estimation is achieved using LCT: a successor is searched for the best match local maxima in the successive image. Each successive positions of the tracked feature is chained into a trajectory using the following rule

$$u_j = \{\vec{X_j}(t_i) | \forall t_i \in [1, N]\} \ ,$$

where N is the number frames in the sequence in which the feature is not lost. The trajectories are then gathered in

$$U = \{u_j | \forall j \in [1, M]\} \ ,$$

where M is the number of trajectories. The trajectory of a feature is interrupted if the quality of the tracking, here defined as the correlation value, falls below a certain threshold. When a trajectory is interrupted, and the feature disappears in the frame

n but reappears in the frame $n+1$, then the algorithm builds two trajectories rather than one; this choice does not prevent the estimation of the differential rotation.

For each trajectory u_j, the positions $\vec{X}_j(t_i)$ of the features are converted to heliocentric coordinates (b, Λ), see Section 3.7, and the mean motion is derived by fitting the linear motion model $\Lambda_j(t_i) = c_j + d_j \times t_i$ in the longitudinal locations of all features of the trajectory. For a period of one month (arbitrarily chosen), the rotation velocities d_j of each trajectory is then plotted as a function of the mean of the latitudinal positions $b_j(t_i)$ of the trajectory. In the plot showing the rotation velocities as a function of their mean latitudinal location (see Figure 5.6), we select the region where the local density of tracked features (represented by a small circle) is sufficiently high, as illustrated by the red line in Figure 5.7. We then fit the differential rotation model, given by the formula (1.3), of all the tracked features over one month of data as a function of their mean latitudinal position.

Application on EIT Archive

We have applied our method of feature tracking to the EIT archive available at the Royal Observatory of Belgium (ROB). In particular, we have focused our effort on the 30.4 nm channel. Our objective is to fit our measurements with the models of differential rotation described in Section 1.2.4. We have tracked the local maxima of the CWT: Figure 5.5 shows one frame of the month of May 1997 sequence, with all tracked features labeled by a number superimposed on the image.

We fit the differential rotation according to Equation (1.3) of all the tracked features over one month of data (slightly more than a solar rotation). Depending on the scale, the local maxima have different corresponding features in the 30.4 nm images. At the scale $s = 8$ pixels, the algorithm tracks features that correspond to Active Region (AR) and small AR, as well as some part of the chromospheric network and large filaments. Smaller scales ($s = 4$ and $s = 2$ pixels) correspond to the bright network, smaller active regions, small loops and bright points. The analysis was achieved using the Mexican Hat (MH) CWT on dyadic scales, discretized on the scales 2, 4, and 8 pixels. Indeed, these scales appear to be, in the 30.4 nm channel, the extreme values of scale for local maxima tracking. The monthly solar rotation parameters A and B are shown in Figures 5.8, 5.9, and 5.10, in order to look for the trends of these rotation parameters over the 23rd solar cycle. At the highest scale ($a = 8$ pixels), the motion is clearly underestimated due to the fact that at this scale several objects with possibly independent motions are contributing to the estimation of motions. Thus, this tracking algorithm will tend to favor the lowest motion solution thus biasing the estimated rotation towards slow motions. At the lowest spatial scale ($a = 2$ pixels), the density of features is too high for fast computation since it approaches the full density case.

Figure 5.5: Single frame showing the tracking of EUV solar features defined as local maxima and at scale $a = 4$ pixels, over the month of February 1997. Each tracked feature is labeled by a number.

Results

We can draw several conclusions from our study of the differential rotation, and the results of Figures 5.6 5.7, 5.8, 5.9, and 5.10:

- there exist a best scale for motion estimation ($s = 4$ pixels, $\approx 4 \times 1.8$ Mm ≈ 7.2 Mm), that corresponds at best to visual observation of the rotation in terms of number of features to track: it certainly corresponds to a trade-off between the typical size of the network cell borders observed in the 30.4 nm passband and the size of bright points,

- at the scale $s = 4$, the rigid rotation coefficient A is varying around the value of 13.62 ± 0.03 degree per day, and shows two periods of 12-month period variation due to rotation and incorrect radius value, and a yet unexplained pseudo-period of ≈ 4 years,
- the coefficient of differential rotation (B) also periodically varies but with a different period,
- the other models (asymmetric, sin4) show that the cycle variation is asymmetric.

These results have to be compared to the existing knowledge of the differential rotation observed in the atmospheric layers of the solar atmosphere. We have provided synodic rotation rates. The synodic rotation is classically transformed into a sidereal one by correcting the synodic rotation rate by a factor 0.986 deg per day. Nevertheless in our case, the short-time scales imposes to use the more precise correction method suggested in [90] but this has not been implemented here.

5.4 Discussion

We have presented our analysis of oscillating displacements of coronal loops in a sequence observed by the TRACE instrument. Once the features are selected, they are tracked by optical flow and gathered into trajectories. These trajectories are analyzed using a Morlet wavelet, and a criterion is used to extract the oscillating features from trajectory ridges. Our method does not depend on a prior manual feature selection and line segment definition. It can process motions that have linear trends such as translations, and sequences with irregular time sampling. In a future work, we will augment our algorithm so that it tracks all pixels by optimising the code and using a more powerful processor with extended memory. We will also use the error prediction to analyze and select more precisely the trajectories.We plan to apply our technique to the upcoming SDO/AIA data for which automatic detection of oscillations will be needed. The tracking procedure is also a powerful tool to estimate rotation velocity of the solar atmosphere. This method tracks the wavelet local maxima of the CWT using the LCT, but in the future the optical flow could be used to fasten the computation and enhance the precision of the result in terms of sub-pixel velocity measurements. This method yields promising results, especially concerning the evolution of the parameters of the differential rotation over the 23rd solar cycle. There exist other very challenging results to obtain using the tracking to refine our knowledge of the differential rotation: study of the meridional flows, of the lifetimes of the tracker, of the feature intensity, of its latitude and longitudes by bins in order to investigate the torsional oscillations, of the spatial scale and of the wavelength through multiwavelength study.

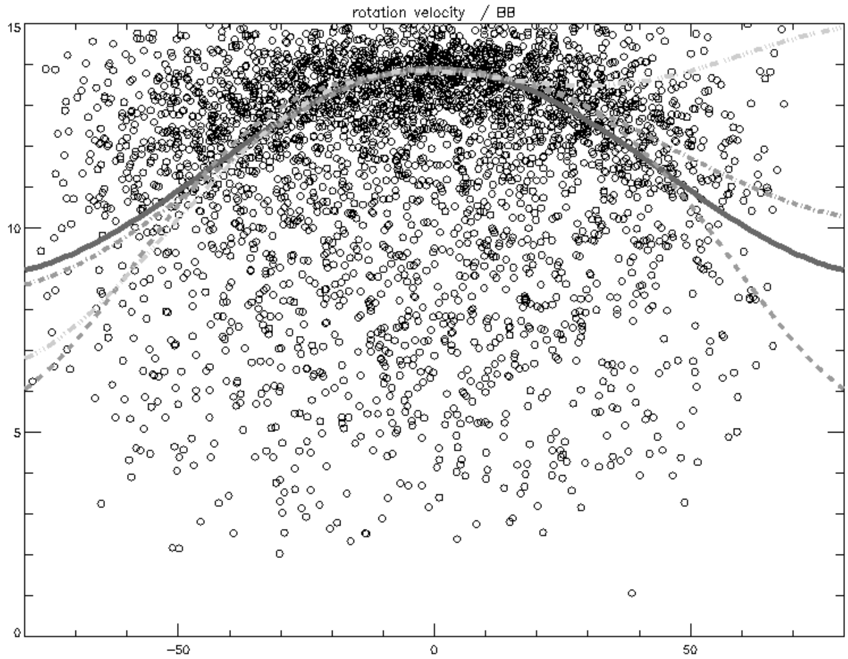

Figure 5.6: Tracking of EUV solar features over 23rd solar cycle at scale $a = 4$ pixels during February 1997. Horizontal axis: Latitude in degrees. Vertical Axis: Synodic Rotation Velocity, in degree per day. Each circle represents a trajectory: its vertical axis coordinate indicates the rotation velocity (from a fit by a linear motion), and its horizontal axis coordinate is its mean latitude. The solid line represents the regression of the model (1.3) through a selection of solar features by threshold a 2D density function. The other lines correspond to other differential rotation models, for instance given by formula (1.2.4).

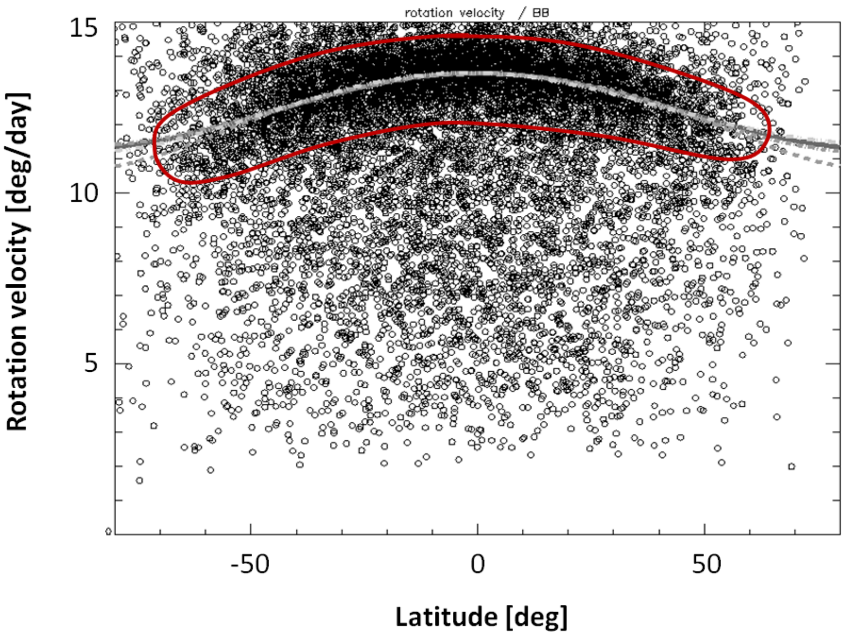

Figure 5.7: Tracking of EUV solar features over 23rd solar cycle at scale $a = 2$ pixels during February 1997. Horizontal axis: Latitude in degrees. Vertical Axis: Synodic Rotation Velocity, in degree per day. Each circle represents a trajectory: its vertical axis coordinate indicates the rotation velocity (from a fit by a linear motion), and its horizontal axis coordinate is its mean latitude. The solid line represents the regression of the model (1.3) through a selection of solar features by threshold a 2D density function (red line). The other lines correspond to other differential rotation models, for instance given by formula (1.2.4).

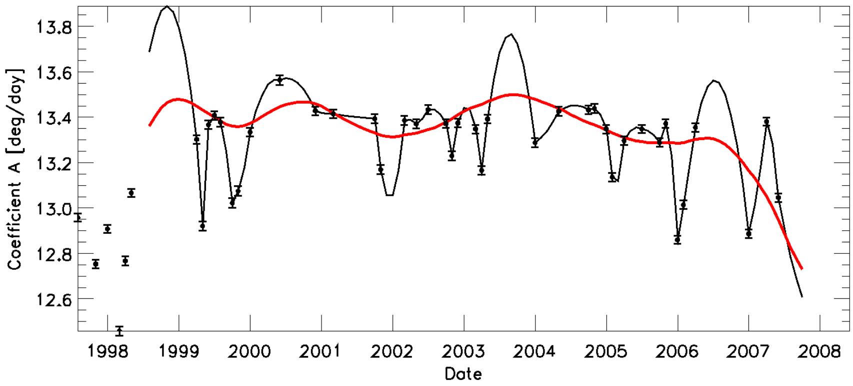

Figure 5.8: Coefficient A over 23rd solar cycle at scale $a = 8$ pixels. The red line is the a smoothed version of the signal for which the oscillating components with period lower than 12 months have been removed. In Formula 1.3, the coefficient A is the coefficient of rigid rotation equal to the rotation rate at the equator.

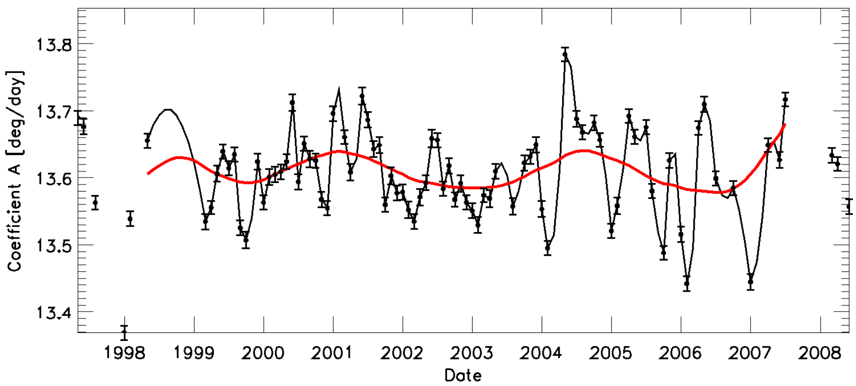

Figure 5.9: Coefficient A over 23rd solar cycle at scale $a = 4$ pixels. The red line is the a smoothed version of the signal for which the oscillating components with period lower than 12 months have been removed. In Formula 1.3, the coefficient A is the coefficient of rigid rotation equal to the rotation rate at the equator.

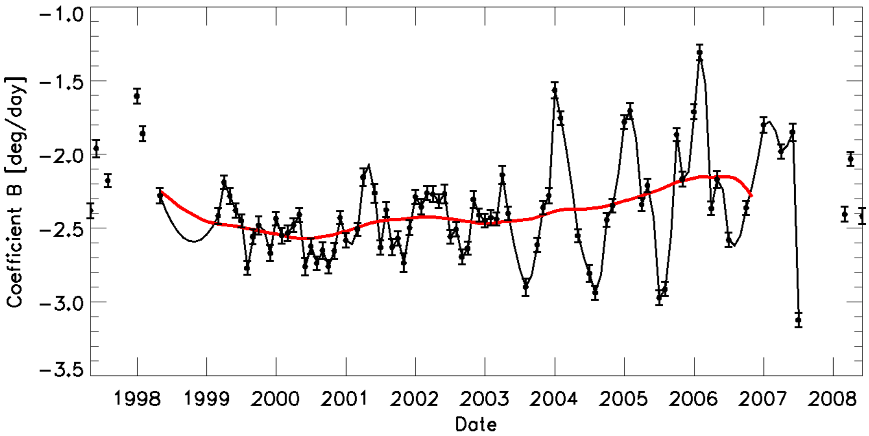

Figure 5.10: Coefficient B over 23rd solar cycle at scale $a = 4$ pixels. The red line is the a smoothed version of the signal for which the oscillating components with period lower than 12 months have been removed. In Formula 1.3, the coefficient B is the coefficient of differential rotation.

Chapter 6

Stereo Reconstruction using STEREO-SECCHI-EUVI Data

Since the launch of the Solar TErrestrial RElations Observatory (STEREO) mission, the Sun Earth Connection Coronal and Heliospheric Investigation (SECCHI)-Extreme UltraViolet Imager (EUVI) telescopes provide the first Extreme Ultraviolet (EUV) images enabling a 3D reconstruction of solar coronal structures. In this chapter, we present a stereoscopic reconstruction method based on the *Velociraptor* algorithm, a multiscale optical-flow method that estimates displacement maps in sequences of EUV images. Following earlier calibration on sequences of SoHO-EIT data, we apply the algorithm to retrieve depth information from the two STEREO viewpoints using the SECCHI-EUVI telescope. We first establish a simple reconstruction formula that gives the radial distance to the centre of the Sun of a point identified both in EUVI-A and -B from the separation angle and the displacement map. We select pairs of images taken in the 30.4 nm passband of EUVI-A and -B, and apply a rigid transformation from the EUVI-B image in order to put both images in the same frame of reference. The optical flow computation provides displacement maps from which we reconstruct a dense map of depths using a stereoscopic formula. Finally, we discuss the estimation of the height of an erupting filament. This method has been presented in Gissot *et al.* [42].

6.1 Introduction

The complexity of magnetic structures of the solar corona is well observed in EUV observations of the Sun. In EUV images of the solar atmosphere, loops and filaments appear as compact structures that are well observed at the limb and on the disc when compared to the surrounding fuzzy corona. In the latter case, there remains an ambiguity on the height of the features. In order to solve the third dimension, two points of view are necessary to perform a stereoscopic reconstruction. The height of EUV bright points has been estimated and analyzed in Brajša *et al.* [17] using the method proposed by Rosa *et al.* [88]. Similar work has been achieved on filament height estimation [105]. Since the launch of the Solar TErrestrial RElations Observatory (STEREO) mission [57], it is possible to resolve the 3D ambiguity by using the observation of the two viewpoints STEREO-A and STEREO-B. First loop reconstructions have been published in Feng *et al.* [32] using a loop extraction [55]. A method for stereoscopic reconstruction and epipolar geometry has been proposed [54]. We present a method for retrieving the depth information from a pair of STEREO-SECCHI-EUVI images observed on-board the two spacecrafts of the STEREO mission using simple geometrical facts and a novel algorithm, *Velociraptor* [40, 41], to estimate the subpixel displacement. The *Velociraptor* algorithm is a multiscale optical flow algorithm derived from a local gradient-based technique able to estimate displacement and brightness variation maps in solar extreme-ultraviolet images as recorded by the Extreme ultraviolet Imaging Telescope (EIT) on board the Solar and Heliospheric Observatory (SOHO) and by the Transition Region and Coronal Explorer (TRACE). Here the displacement maps to estimate are shifts along the epipolar line caused by the separation of the two STEREO viewpoints, and no brightness variation is supposed: this method is here applied to estimate the height of an erupting filament.

6.2 3D Reconstruction Method

In this section we present the method for retrieving the altitude information from a pair of STEREO images. In the following we will refer to the image observed in EUVI on-board STEREO spacecraft STEREO-A and STEREO-B as EUVI-A and EUVI-B, respectively. We introduce two heliocentric-Cartesian coordinate systems S_A and S_B with notation (x,y,z), that both have their origin at the Sun centre O, with y normal to the STEREO mission plane (STEREO-A,STEREO-B,O) and z pointing to solar disc centre of either EUVI-A (system S_A), or EUVI-B (system S_B). In the following, the indices A and B refer to the coordinate systems S_A and S_B, respectively. The objective is to measure the radius $R = OP$ of a point P of coordinates $(X_\mathrm{A},Y_\mathrm{A},Z_\mathrm{A})$ in S_A and $(X_\mathrm{B},Y_\mathrm{B},Z_\mathrm{B})$ in S_B. After the pre-registration step, the point P observed in EUVI-A is seen in EUVI-B as P', *i.e.* as P rotated by an angle of $\Delta\lambda$.

6.2.1 Pre-Registration

Since the Sun may be assumed to be at an infinite distance of STEREO-A and of STEREO-B, Figure 6.3 shows that in both instruments the solar disc as traced by its limb is the orthogonal projection of the solar sphere of centre O and photospheric radius R_s as observed in EUVI-A. In the following, the separation angle between

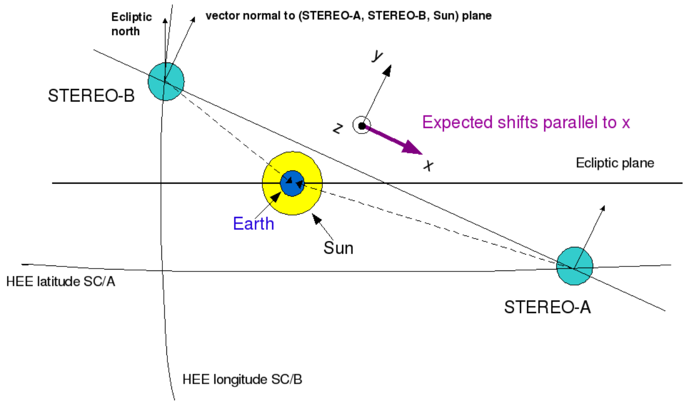

Figure 6.1: STEREO mission plane (STEREO-A, STEREO-B, O) and ecliptic north axis. The S_{A} and S_{B} coordinate systems have their origin at the Sun centre O and their y-axis perpendicular to (STEREO-A, STEREO-B, O) and z pointing either to STEREO-A (S_{A}) or STEREO-B (S_{B}).

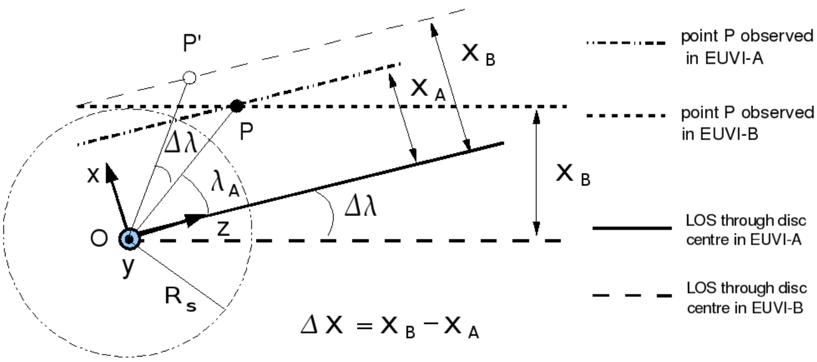

Figure 6.2: Apparent displacement ΔX of P after the pre-registration step applied to EUVI-B so that it can be matched with EUVI-A. The point P appears as P' in EUVI-B where P' is the point P rotated by $\Delta\lambda$.

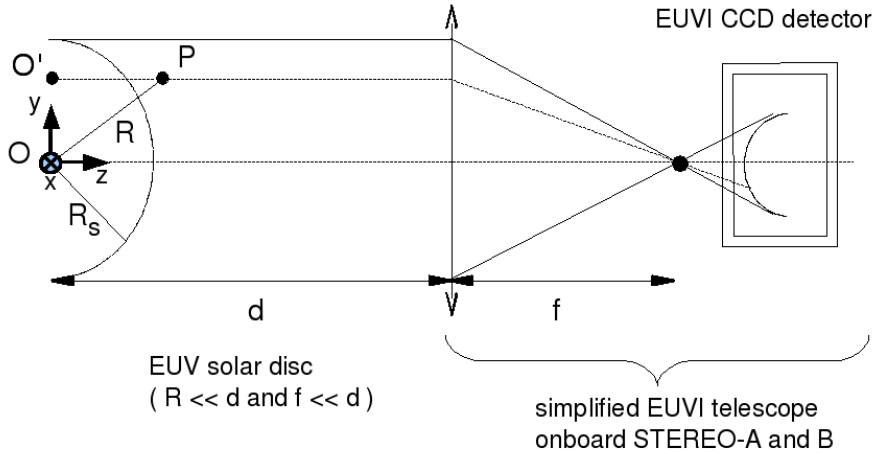

Figure 6.3: The projection model of the Sun in the EUVI detectors of the STEREO spacecrafts STEREO-A and STEREO-B.

spacecrafts is denoted by $\Delta\lambda$, λ_A is the angle of P to Oy, R is the distance of P to the Sun centre, (X_A,Y_A,Z_A) and (X_B,Y_B,Z_B) are the coordinates of P in S_A and S_B, respectively (see Figure 6.4). Figure 6.2 shows that observing P on the solar sphere from two different viewpoints (spacecrafts STEREO-A and STEREO-B) is equivalent to observing, from one unique viewpoint, the point P in EUVI-A rotated to a virtual point P' by an angle $\Delta\lambda$. Indeed the displacement

$$\Delta X = X_\mathrm{B} - X_\mathrm{A} = r\sin(\lambda_\mathrm{A} + \Delta\lambda) - r\sin(\lambda_\mathrm{A}) \ ,$$

is equal to the apparent displacement of P moving to P' after a rotation of angle $\Delta\lambda$ and centre O (see Figure 6.4). Observed in EUVI-B, the point P is equal to P' of coordinates (X_B,Y_B,Z_B) in S_A.
This equivalence requires three conditions: the pointing to the heliospheric centre O must be known with precision, the radius of the solar limb must be the same in EUVI-A and EUVI-B (or equivalently, the distance from STEREO-A and STEREO-B to O must be known with precision), and the axis of the rotation, or the normal to the STEREO mission plane containing STEREO-A, STEREO-B and O (see Figure 6.1) must be known as well. If we impose that this axis be vertical in both image planes, the last requirement ensures that the epipolar lines are horizontal if we neglect the projective geometry effects, so that $Y_\mathrm{A} = Y_\mathrm{B}$. The pre-registration step consists in transforming EUVI-B using translation, rotation, and dilation, in order to set EUVI-B in the same reference frame as EUVI-A so that both image centres are pointing to the Sun centre, they both have the same apparent photospheric radius R_s, and their vertical axis is aligned with the epipolar north. After applying the pre-registration

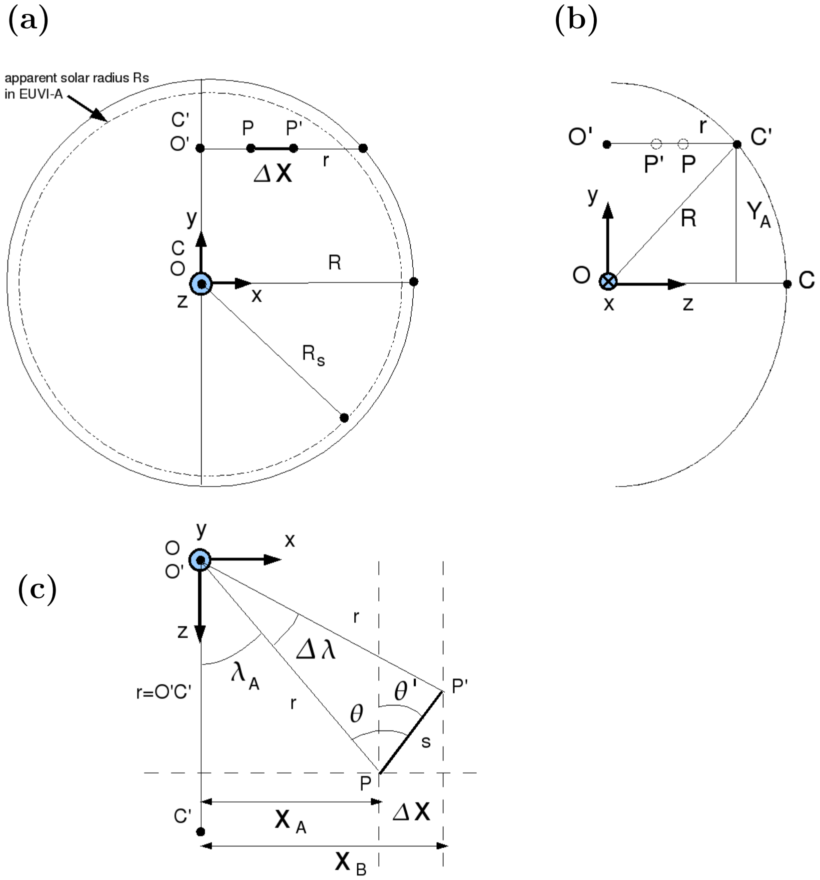

Figure 6.4: Representation of the angles λ_{A}, $\Delta\lambda$, θ, the radii r and R, and the distance s. R_{s} is the photospheric radius as observed in EUVI-A. After the pre-registration step, both images EUVI-A and -B are in the same frame of reference. Figure (a): front view from STEREO-A (EUVI-A) image. Figure (b): left view. Figure (c): top view.

procedure that reads the information contained in the FITS headers, EUVI-A and B now have:

- the line-of-sight (LOS) of the image centres passing through the Sun centre O (after a translation),
- the vertical axis perpendicular to the plane containing (STEREO-A, STEREO-B, O), see Figure 6.1 (after a rotation),
- the same limb radius equal to the photospheric radius R_s from EUVI-A (after a dilation). This dilation is achieved using the distance to the Sun of both spacecrafts.

6.2.2 3D Reconstruction Formula

In Figure 6.4 the point P becomes P' after a rotation of the sphere by an angle $\Delta\lambda$. The line OC shows the LOS passing through the apparent disc centre (Figure 6.2) and pointing to the heliospheric centre O, which is now the same in EUVI-A and EUVI-B. As we estimate depths in EUVI-A, we denote by (X_A,Y_A,Z_A) the coordinates of P. Figure 6.4 introduces the angle λ_A and the distance s. In Figure 6.4, we define $r^2 = X_\mathrm{A}^2 + Z_\mathrm{A}^2$ and $R^2 = X_\mathrm{A}^2 + Y_\mathrm{A}^2 + Z_\mathrm{A}^2$.

As $O'P = O'P' = r$, we have that

$$s = 2r\sin(\Delta\lambda/2) \tag{6.1}$$

and

$$\theta = \pi/2 - \Delta\lambda/2 \ .$$

Moreover, Figure 6.4 (bottom right) shows that $\theta' = \theta - \lambda_\mathrm{A}$ and

$$\sin(\theta') = \frac{\Delta X}{s} = \sin(\theta - \lambda_\mathrm{A}) \ .$$

As a consequence, the expression of the displacement ΔX in terms of the angles λ_A and $\Delta\lambda$ is

$$\Delta X = s\sin(\pi/2 - \lambda_\mathrm{A}/2 - \Delta\lambda/2) \ . \tag{6.2}$$

Using Equations (6.1) and (6.2), the displacement ΔX is related to r and the angles λ_A and $\Delta\lambda$ by

$$\Delta X = 2r\sin(\Delta\lambda/2)\cos(\Delta\lambda/2 + \lambda_\mathrm{A}) \ . \tag{6.3}$$

Furthermore, as $r^2 = X_\mathrm{A}^2 + r^2\cos(\lambda_\mathrm{A})^2$ and

$$X_\mathrm{A} = r\sin(\lambda_\mathrm{A}) = \sqrt{R^2 - Y_\mathrm{A}^2}\sin(\lambda_\mathrm{A}) \ ,$$

we have

$$\Delta X = 2r\sin(\Delta\lambda/2)\cos(\Delta\lambda/2 + \sin^{-1}(X_\mathrm{A}/\sqrt{R^2 - Y_\mathrm{A}^2})) \ . \tag{6.4}$$

We can expand the right-hand side of Equation (6.3) since

$$\begin{aligned} r\cos(\Delta\lambda/2+\lambda_{\mathrm{A}}) &= r\cos(\Delta\lambda/2)\cos(\lambda_{\mathrm{A}}) - r\sin(\Delta\lambda/2)\sin(\lambda_{\mathrm{A}})\ , \quad (6.5)\\ &= \cos(\Delta\lambda/2)(r^2 - X_{\mathrm{A}}^2)^{1/2} - \sin(\Delta\lambda/2)X_{\mathrm{A}}\ . \quad (6.6) \end{aligned}$$

Injecting Equation (6.6) into Equation (6.3) gives

$$r^2 = X_{\mathrm{A}}^2 + \left[\tan(\frac{\Delta\lambda}{2})X_{\mathrm{A}} + \frac{\Delta X}{\sin\Delta\lambda}\right]^2 \quad (6.7)$$

for the value of the apparent radius r. As r is equal to $O'C' = O'P = O'P'$, it is related to the $R = OC$ through $R^2 = r^2 + Y_{\mathrm{A}}^2$. Using Equation (6.7), we obtain the final reconstruction formula of R

$$R^2 = X_{\mathrm{A}}^2 + Y_{\mathrm{A}}^2 + \left[\tan(\frac{\Delta\lambda}{2})X_{\mathrm{A}} + \frac{\Delta X}{\sin\Delta\lambda}\right]^2\ . \quad (6.8)$$

6.2.3 Displacement Estimation and 3D Reconstruction

To reduce the computation time, we estimate the value of ΔX_{s} around the expected displacement at the photospheric level using the formula (6.3) in which we use $R = R_{\mathrm{s}}$ where R_{s} is the photospheric radius. We then use ΔX_{s} as a first guess and let the *Velociraptor* algorithm [40] find the precise sub-pixel displacement ΔX around ΔX_{s}.

6.2.4 Error Formula

We only consider the variance on ΔX, and neglect the uncertainties on other variables X_{A}, Y_{A}, and $\Delta\lambda$ since they have significantly lower contribution to the total error. If V is a centered normal random variable, we have the formulas $\mu_{V^2} = \mu_V^2 + \sigma_V^2$ and $\sigma_{V^2}^2 = 4\sigma_V^2\mu_V^2 + 2\sigma_V^4$. Using these formulas, and assuming that $\mu_{\Delta X} = \Delta X$ is the mean value of ΔX, we compute

$$\mu_{R^2} = X_{\mathrm{A}}^2 + Y_{\mathrm{A}}^2 + \frac{1}{\sin(\Delta\lambda)^4}\left[(2\sin(\Delta\lambda/2)^2 X_{\mathrm{A}} + \Delta X)^2 + \sigma_{\Delta X}^2\right]\ ,$$

and

$$\sigma_{R^2}^2 = \frac{2\,\sigma_{\Delta X}^2}{\sin(\Delta\lambda)^8}\left[(2\sin(\Delta\lambda/2)^2 X_{\mathrm{A}} + \Delta X)^2 + 2\sigma_{\Delta X}^2\right]\ .$$

If we suppose that R as calculated from Equation (6.8) behaves like a random, normally-distributed variable of mean value μ_R and variance σ_R^2, and that

$$\mu_R = \sqrt{\mu_{R^2} - \sigma_R^2} \simeq \sqrt{\mu_{R^2}}\ ,$$

where we assumed that $\mu_{R^2} >> \sigma_R^2$, then the variance σ_R^2 depends on $\sigma_{R^2}^2$ through the relation

$$\sigma_{R^2}^2 = 4\sigma_R^2\mu_R^2 + 2\sigma_R^4\ . \quad (6.9)$$

After solving the second degree equation (6.9), we obtain the formula

$$\sigma_R^2 = \frac{1}{4}\left[\sqrt{16\mu_R^4 + 8\sigma_{R^2}^2} - 4\mu_R^2\right] \simeq \frac{\sigma_{R^2}^2}{4\mu_R^2}\ , \tag{6.10}$$

assuming that $\sigma_{R^2}^2 \ll \mu_R^4$. This formula gives the variance of R.

6.3 STEREO-EUVI Application: Data Reduction and First Results

6.3.1 Description of the STEREO Dataset

We choose a set of EUVI images observed in 30.4 nm passband observed on 19 May 2007 at times 12:41:45 (top), 12:51:45 (middle) and 13:01:45 (bottom), which have a lossy compression level ICER5, meaning a compression ratio of 28 by the ICER compression algorithm. We process them to reconstruct the radius R at each pixel in the image EUVI-A. The stereo separation angle is $\Delta\lambda = 8.6$ deg.

6.3.2 Pre-Registration: Limb Fitting and Rotation Correction

In order to have correct pointing to the Sun centre, we run the *secchi_prep.pro* IDL routine on a pair of fits images that allows a very high quality pointing. Now images EUVI-A and EUVI-B have their centre pointing to the Sun centre O. We then apply the procedure *scc_stereopair.pro* so that both images satisfiy the conditions required in Section 6.2 (see Figure 6.1). At the end of this pre-registration step, we apply the formula described in Section 6.2 and Figure 6.4.

6.3.3 Displacement Estimation

From the formula (6.3) we derive the expected displacement between EUVI-A and EUVI-B images. We then apply the *Velociraptor* algorithm, which gives the displacement at a sub-pixel precision. A high precision is required on the estimation of the upper chromosphere observed in the 30.4 nm passband because the maximum expected height of the maximum network altitude is $\approx$ 10 Mm above the photosphere altitude ($\approx$ 1.45 % of the solar photospheric radius), while prominences are normally observed in the 10 Mm-100 Mm altitude range.

6.3.4 Depth Estimation

In this particular sequence of 19 May 2007, a filament located in the NOAA active region AR0956 is erupting from frame 12:51:45. The existence of this filament is confirmed by the Hα observation of 19 May 2007 at 06:36:32 provided by the Kanzelhöhe observatory (see Figure 6.7). The GOES flare curve indicates that a

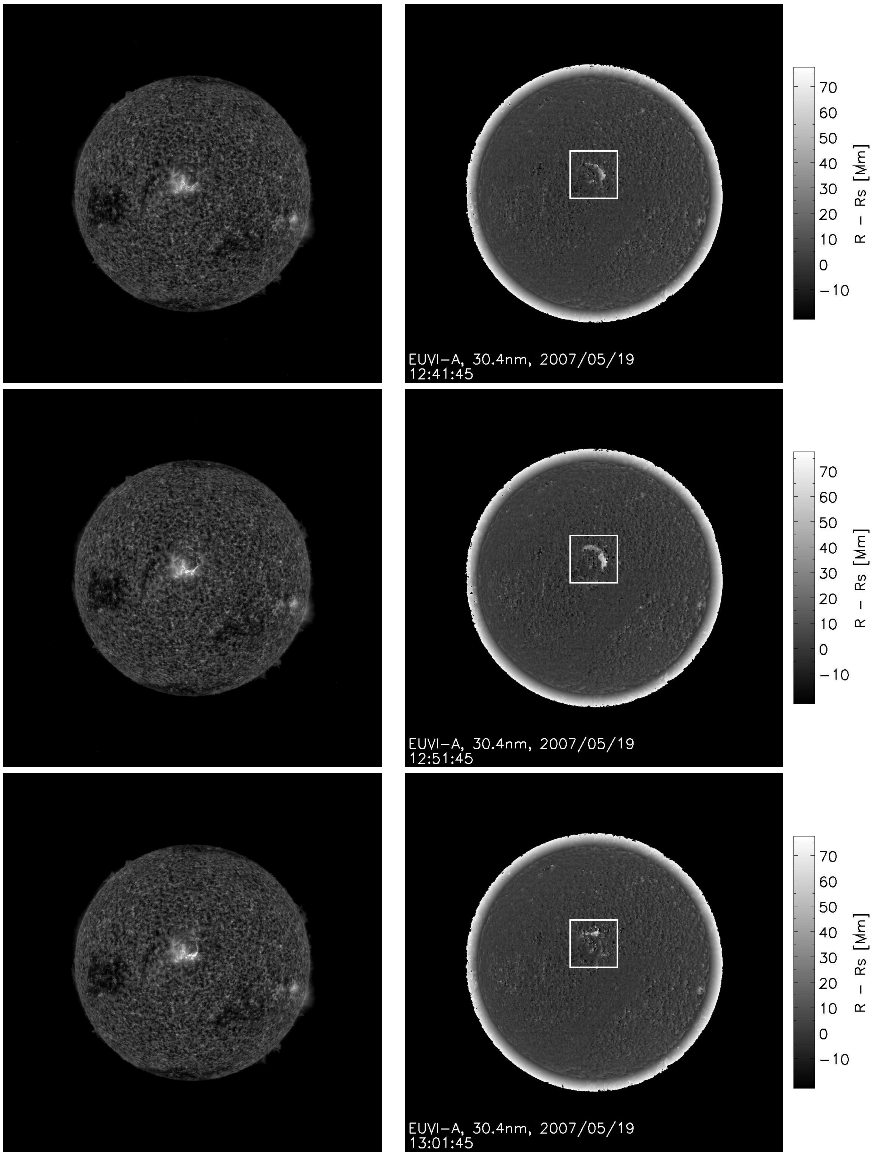

Figure 6.5: Depth map of the EUVI-A stereoscopic reconstruction. Left: original EUVI-A images observed at times on 19 May 2007 at times 12:41:45 (top), 12:51:45 (middle) and 13:01:45 (bottom). Right: corresponding maps of radius estimations, showing the height $R - R_\mathrm{s}$ above the limb.

C-flare is simultaneously observed in the same active region. At the three different times, we reconstruct the full solar disc; Figure 6.5 shows the maps of relative radius R. On the left part are the original images, while the radius maps stand in the right column. The dark values, indicating heights below the surface, are due to unstable displacement estimations. In this sequence of three reconstructions, the erupting filament, indicated by a square region of interest (ROI) in the upper right image of Figure 6.5. The zooms on this ROI are shown in Figure 6.6. We plot the heights of points located on the filament in Figure 6.8 and on line segments across the filament in Figure 6.9. The 1-sigma error bar provided by the formula (6.10), using a value of $\sigma_{\Delta X} = 0.5$, are overplotted on the height curves. Figures 6.8 and 6.9 show the process during which the filament disappears at the same time that a C-flare is observed in the 30.4 nm image (Figure 6.6, middle and bottom figures); it is confirmed by the GOES flux (Figure 6.7 (b)). During this sequence of images, the filament is rising and expanding as shown in Figure 6.9. In the middle image (12:51:45), the flare starts after the onset of the filament eruption. In the lower right figure (13:01:45) of Figure 6.6, the filament has partially broken away. The brighter part of the ribbons of the flare is situated on both sides of the polarity inversion line (PIL) but only in the part of the PIL where no elevated filament is observed, while a less bright ribbon is observed very closely aligned with the erupting filament, possibly because of the projection effect due to the filament elevation. From our analysis, a possible scenario is that the PIL passes between the two ribbon sites where there is no filament, and that in this part of the PIL, a flare occurs and causes the two ribbons as well as post-flare loops observed in images of hotter coronal lines such as 19.5 nm. Along the part of the PIL where the filament is reconstructed, the eruption occurs without ribbons and post-flare loops because there is no plasma heating in the reconnection site of the erupting filament. In a future work, the filament height estimations will be compared with critical heights of eruption defined and analyzed in Filippov and Den [34] and Filippov and Koutchmy [33]. The time cadence (10 minutes) limits the measurement of the velocity of the erupting filament. Despite this limitation, the present study enables the 3D reconstruction of the on-disc eruption.

6.4 Conclusion

We have presented our method of stereoscopic reconstruction using pairs of EUVI images provided by the two STEREO spacecrafts. We have first established in the heliocentric coordinate system the formula that provides, given the separation angle and a preprocessing step, the expected displacement between two pixels at the photospheric radius. After inversion of this formula, we derive the stereoscopic reconstruction formula that gives the radius of solar features given the estimated apparent displacement between the two STEREO frames. We use the former formula to calculate the expected displacement at the photospheric level in order to lower

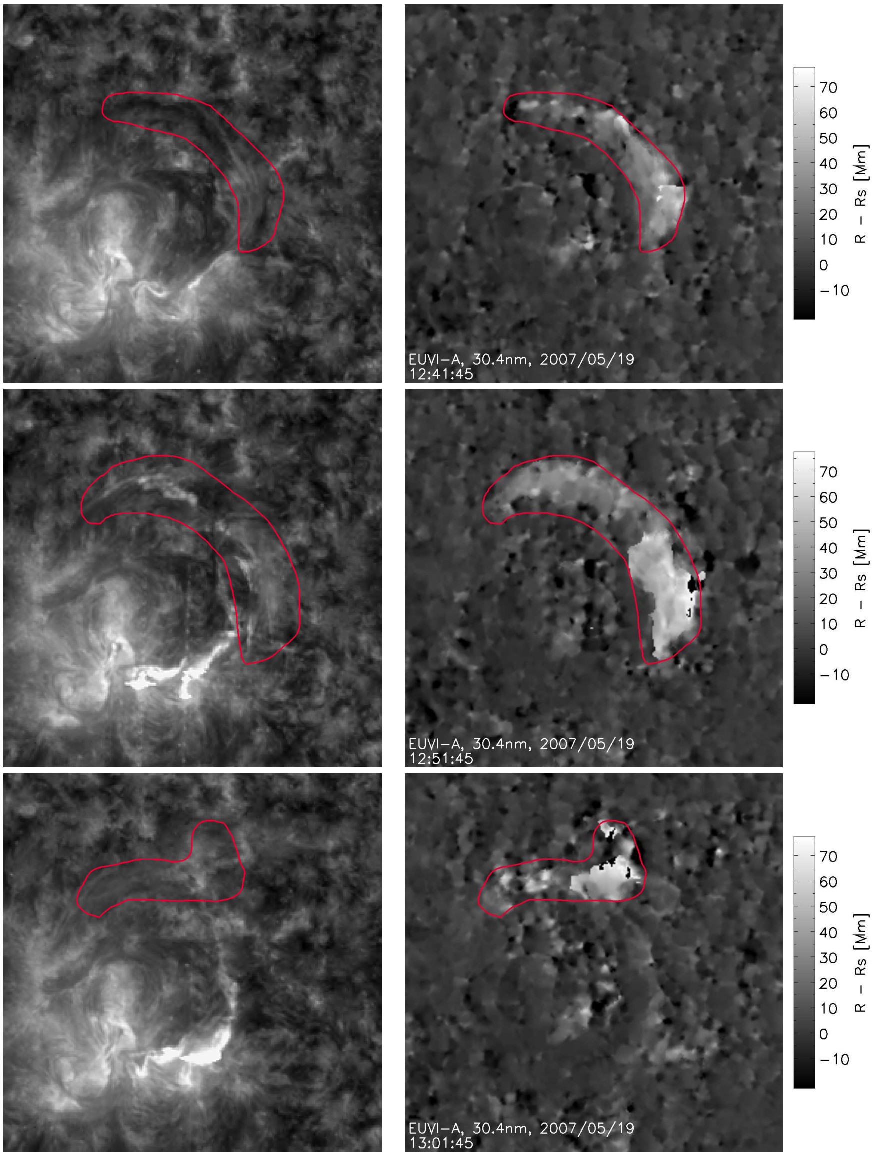

Figure 6.6: Depth map of the EUVI-A stereoscopic reconstruction. Left: zoom on original EUVI-A images observed at times on 19 May 2007 at times 12:41:45, 12:51:45 and 13:01:45. Right: zoom on corresponding maps of radius estimations, showing the height $R - R_{\mathrm{s}}$ above the limb.

(a) **(b)**

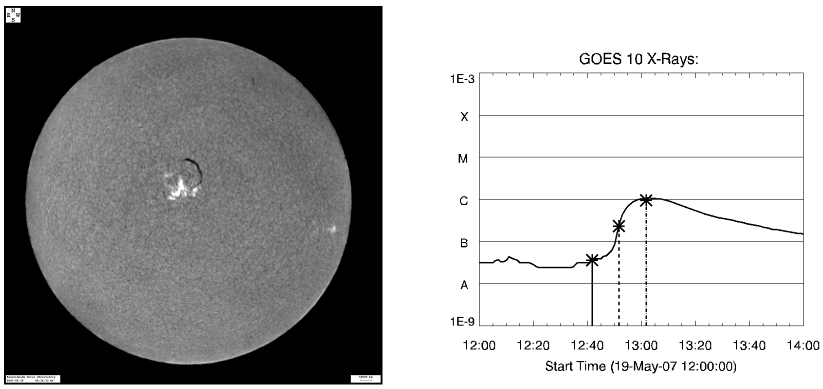

Figure 6.7: The presence of the filament is also observed in the Kanzelhöhe Hα image on 19 May 2007 at 06:36:32 UT in panel (a). The presence of the C-flare is confirmed by the GOES flux in panel (b).

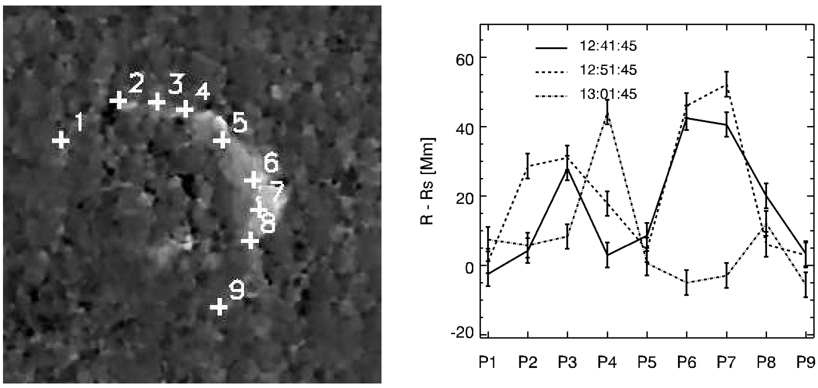

Figure 6.8: Height above the limb ($R - R_{\mathrm{s}}$) for pixels 1 to 9.

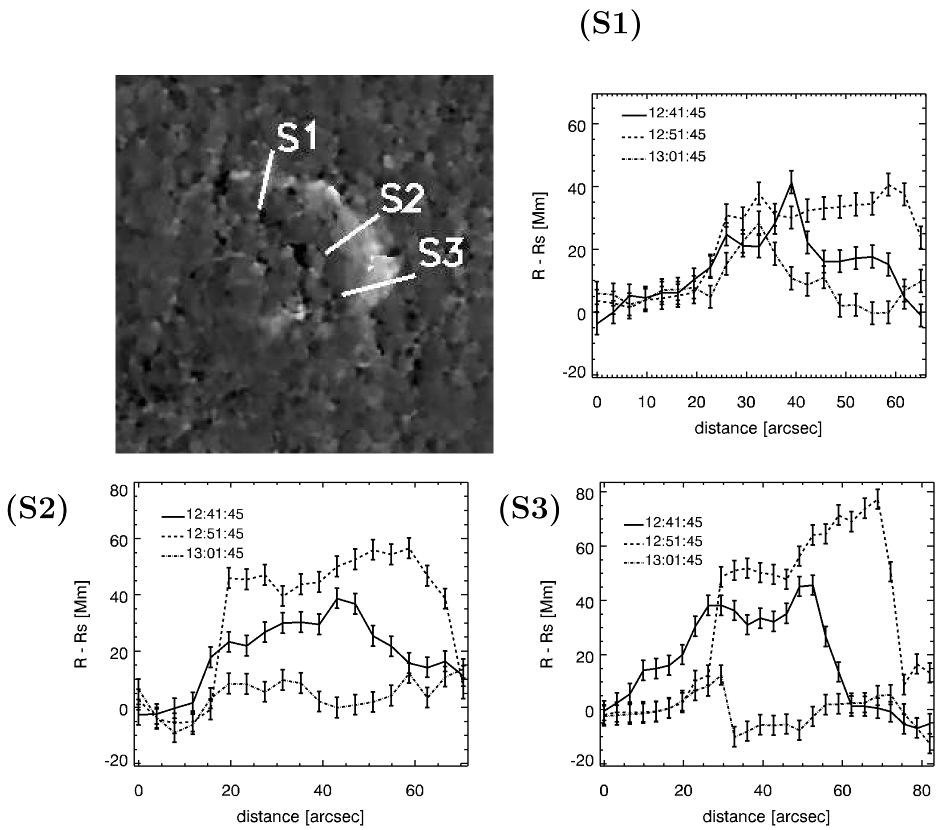

Figure 6.9: Height variations of segments S1, S2 and S3 above the limb ($R - R_{\rm s}$).

the computation time. In the sequence of 19 May 2007, the study of the altitude of the eruptive filament is achieved simultaneously with the observation of a C-flare.

In the future, we will process calibration images showing solar-like textures generated on a sphere using the work of Chainais [21], to calibrate the error prediction method developed in Gissot and Hochedez [40], and improve the value $\sigma_{\Delta X} = 0.5$ in order to assess with precision the error on our radius measurement; we expect to be able to measure precisely the local radius of the Sun in the 30.4 nm upper chromosphere, in order for instance to assess the altitude of the chromospheric network. This will also allow us to study the altitude of quiescent and eruptive filaments and their evolution along the year 2007 of STEREO data, and study the mass and 3D motion estimation of the erupting filament.

Chapter 7

Spatio-Temporal Algorithms for Motion Estimation of Solar EUV Images

Images of the solar atmosphere are observed and interpreted by astronomers in order to get the dynamics characteristics of solar and coronal events. So far, we have only considered the motion estimation in pairs of frames and processed the information contained in the difference image as shown in Chapter 3. One may want to use more temporal information of sequences longer than two images. A time series of image data forms a three-dimensional array of values, of dimension 2 in space and 1 in time (2D + T), equivalent to a 3D datacube. The $(2+1)-D$ continuous wavelet transform may be utilized to represent a datacube according to the following parameters: location in space and time, spatial scale, and the velocity parameters (direction and velocity amplitude), see Section A.4. The Motion-Tuned Spatio-Temporal Wavelet Transform (MTSTWT) aims to estimate velocity from the datacube of image; it has been introduced by Duval-Destin and described in Antoine *et al.* The velocity measurement estimation using the spatio-temporal wavelet transform uses the temporal information contained in the datacube and is thus more robust against noise than two-frame motion estimations such as the optical-flow method: there is indeed less information in a two-frame sequence analyzed by typical optical flow algorithms. The main drawback of this approach is that the sequence is assumed to be regularly sampled over time. The MTSTWT can be seen as a spatio-temporal filtering operation where the filter characteristics are controlled by a set of parameters associated with motion features, *i.e.* velocity and size. This algorithm has been successfully tested in [3] on test sequences including Gaussian shaped objects. The continuous spatio-temporal wavelet transform is detailed in Appendix A.4 and A.4.

7.1 The Motion-Tuned Spatio-Temporal Wavelet Transform Algorithm

A sequence of images can be modeled as a spatio-temporal signal $s(\vec{x}, t) \in L^2(\mathbb{R}^2 \times \mathbb{R})$. The MTSTWT [63, 71, 72] provides a complete representation of s in the parameter space of location $\vec{x}$, time t and velocity $\vec{v} = (c, \theta)$. The MTSTWT has several advantages: it is robust against noise, and the temporal scale is linked to the velocity such that short time scales correspond to fast motions. As noted in [1], "*this transformation comes from the behavior of our visual system: in order to be visible, fast moving objects must be wide, and narrow objects must move slowly.*" It also enables an estimation of the location of the moving objects. This event detection may arise from a single parameter threshold applied on the wavelet spectrum. One of its effects is that it tends to smooth the velocity field over time. The original tracking algorithm proposed by [71] aims to update the positions and displacement estimations that are supposed to be known. The spatio-temporal transform is introduced in Appendix A.4.

There are several applications of the MTSTWT: compression and reconstruction of image series, displacement prediction using Kalman filtering (real-time tracking), and the estimation of motions from sub-pixel displacements up to large motions.

7.1.1 Algorithm

Using the MTSTWT algorithm, we estimate the velocity field at any time step and at each pixel location of a sequence of Extreme Ultraviolet (EUV) images of the solar atmosphere. The resulting velocity field depends on the scale of the transform; this scale represents the spatial scale of the signal and is analogous to the neighbourhood size in the optical flow algorithm. The wavelet spectrum value is the result of the motion oriented filtering, and gives the level of confidence of the velocity estimate. In the method presented here, this value is compared to a threshold in order to determine the locations where the estimated displacement is reliable. We apply the algorithm in the following way: We fix the scale $a = a_0$, and for each parameters $(\vec{b}, \tau)$, meaning at each location and at each time step, we search the motion parameters c, θ (see Figure 7.1, inspired from [19]) maximizing the wavelet spectrum $E(g) = |\langle \psi_g | s \rangle| = |S_\psi(g)|$ where g is the set of wavelet transform parameters. As the wavelet transform may be interpreted as a "selective velocity" filtering, we then filter the map of coefficients $E(\vec{b}, \tau, a_0, \theta, c)$ by thresholding it in order to keep only the reliable estimated motion field (c, θ) at each location. It should be noted that in this operation, the algorithm selects the "best angle" θ for motion estimation, meaning that it solves automatically the aperture issue (see Section 3.5) when possible by selecting the normal component of the flow but without having to use any arbitrary threshold coefficient.

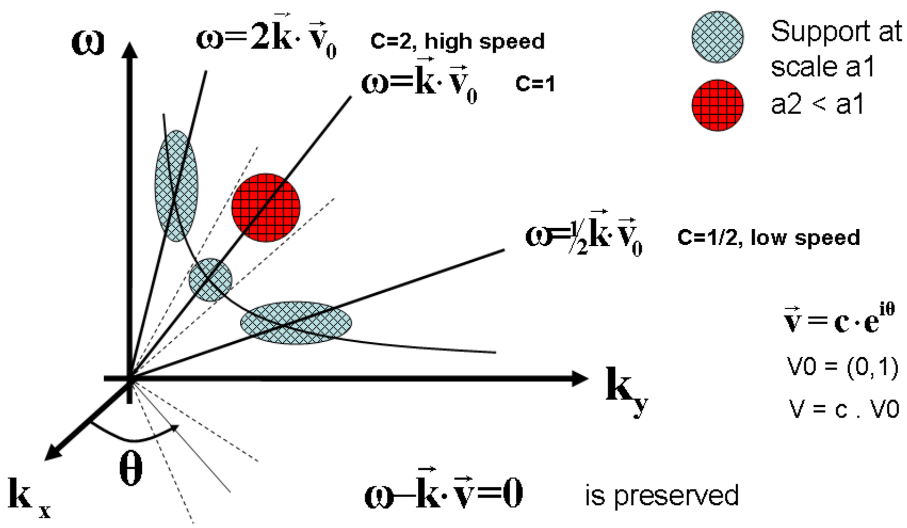

Figure 7.1: Spatio-temporal wavelet analysis in the Fourier domain. The ellipses represent the support of the wavelet for different transform parameters; one observes the effect of spatial dilation (parameter a), rotation of parameter θ corresponding to the direction of motion, and the motion-tuning (parameter c) that correspond to the absolute value of the motion vector. This illustrates how the motion parameters c and θ adapt to the dispersion relation $\omega = \vec{k}\vec{v}$ that corresponds to a linear displacement the signal.

We have discretized the set of parameters $\vec{b}, \tau, a, \theta, c$ so that they give the best results on our calibration data. It is possible to achieve this operation at each spatial scale of interest, but in our application we fix the scale a as if we were looking for a specific type of coronal objects.

Reconstruction Formula The signal can be reconstructed from the coefficients of the ST wavelet transform. Indeed, this transform is isometric [3] and thus invertible on its range.

7.2 Results

7.2.1 Calibration on Synthetic Data

We apply the ST wavelet transform on synthetic data to prove its efficiency at estimating the velocity parameters in a synthetic sequence.

Isotropic Objects

The synthetic signal is made of a sum of two Gaussian objects with two different starting times and two different trajectories, see Figure 7.2. The results, compared to the ground truth shown as the black arrow.

Directional Objects

We also have calibrated our algorithm by estimating the motion field on a sequence simulating a loop expansion. The resulting estimated motions are displayed in Figures 7.4 and 7.3. This demonstrate the ability of the MTSTWT to estimate motions of directional objects via its anisotropic spatio-temporal wavelet (see Appendix A.4).

7.2.2 Application

The analysis based on the spatio-temporal wavelet can be used to estimate motion and to compress the signals. In our solar physics application, we use the algorithm to derive velocity fields but it is shown that with high-cadence data of future solar missions such as Solar Dynamics Observatory (SDO), extraction and identification of moving objects using the one-parameter of the MTSTWT may be achieved. We apply the algorithm on a EUV sequence of solar atmospheric observations.

The result is compared to a flow computed using our optical flow motion estimation algorithm presented in Chapter 3. The results are comparable but their difference my be interpreted this way: the MTSTWT flow field is much closer to the normal flow along the loops in the active region (upper part of the image in Figure 7.5).

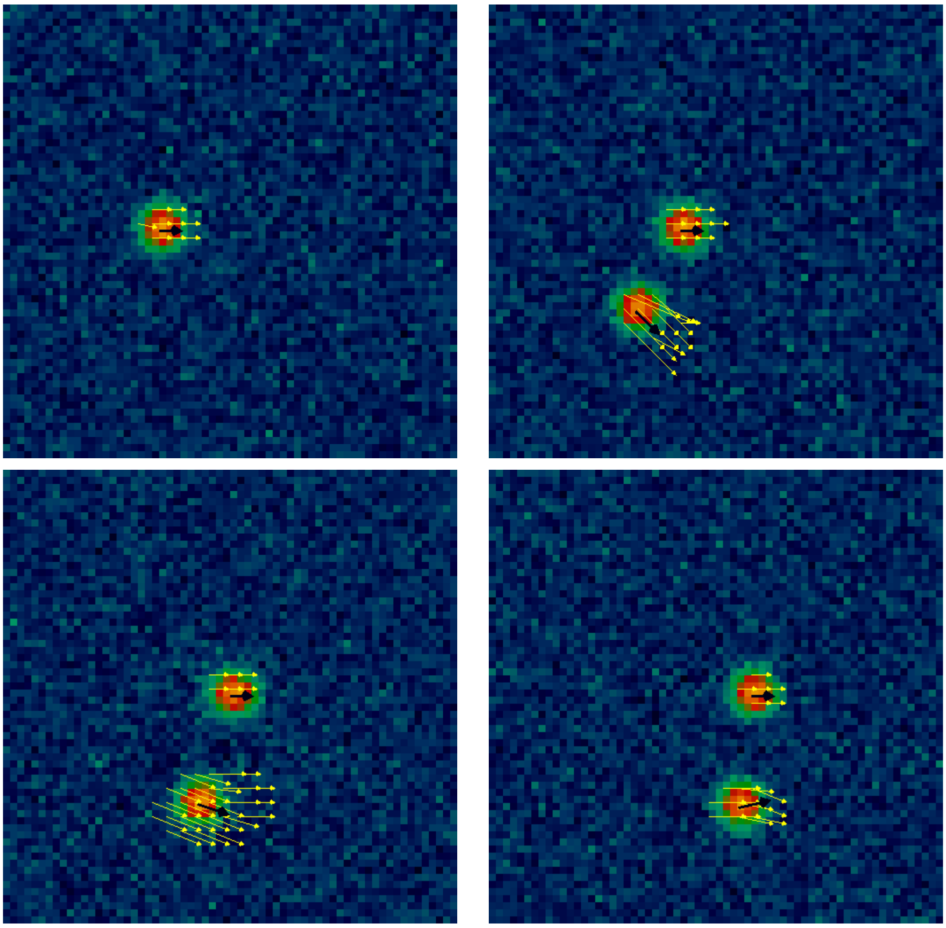

Figure 7.2: Results on isotropic synthetic data (a sum of Gaussian objects).

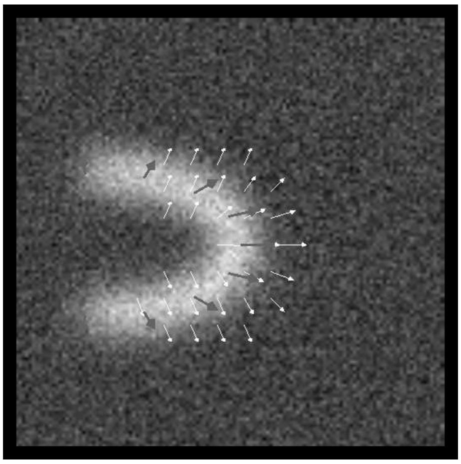

Figure 7.3: Results on synthetic directional data that simulate a loop expansion. The velocity prescribed to the synthetic data is in gray and the estimated field is super imposed in white color.

7.3 Discussion

The spatio-temporal wavelet transform is a powerful motion estimation tool adapted to the search of moving objects in datacube. It processes the space-time datacube; by using the analysis formula, one can build sparse representation of the signal s using a threshold of the wavelet coefficients. The sparse representation of the signal gives access to the velocity field, and possibly to the extraction of moving objects by thresholding the ST wavelet spectrum. Its inconveniences is the memory required for computation (through the 3D FFT) but the computation time remains acceptable compared to unoptimized optical flow (Interactive Data Language (IDL) code in both cases); they both take roughly the same time on 512×512 Extreme ultraviolet Imaging Telescope (EIT) images. The resulting velocity is smooth over time but robust against intensity errors and outlying pixels; it is less adapted to the tracking of fast motions, for instance to motions that would be observed only during the succession of two frames. It is more intended to be used on noisy block of data, regularly cadenced, containing features that move smoothly. It also has the advantage that it automatically spots Gaussian-like objects, similar to bright points, from a single arbitrary coefficient, but also adapts and detects the motion of elongated objects such as coronal loops, which means it is simple to use and to adapt to the data. The high-cadence SDO mission may be an unique occasion to get the benefits from the MTSTWT wavelet transform.

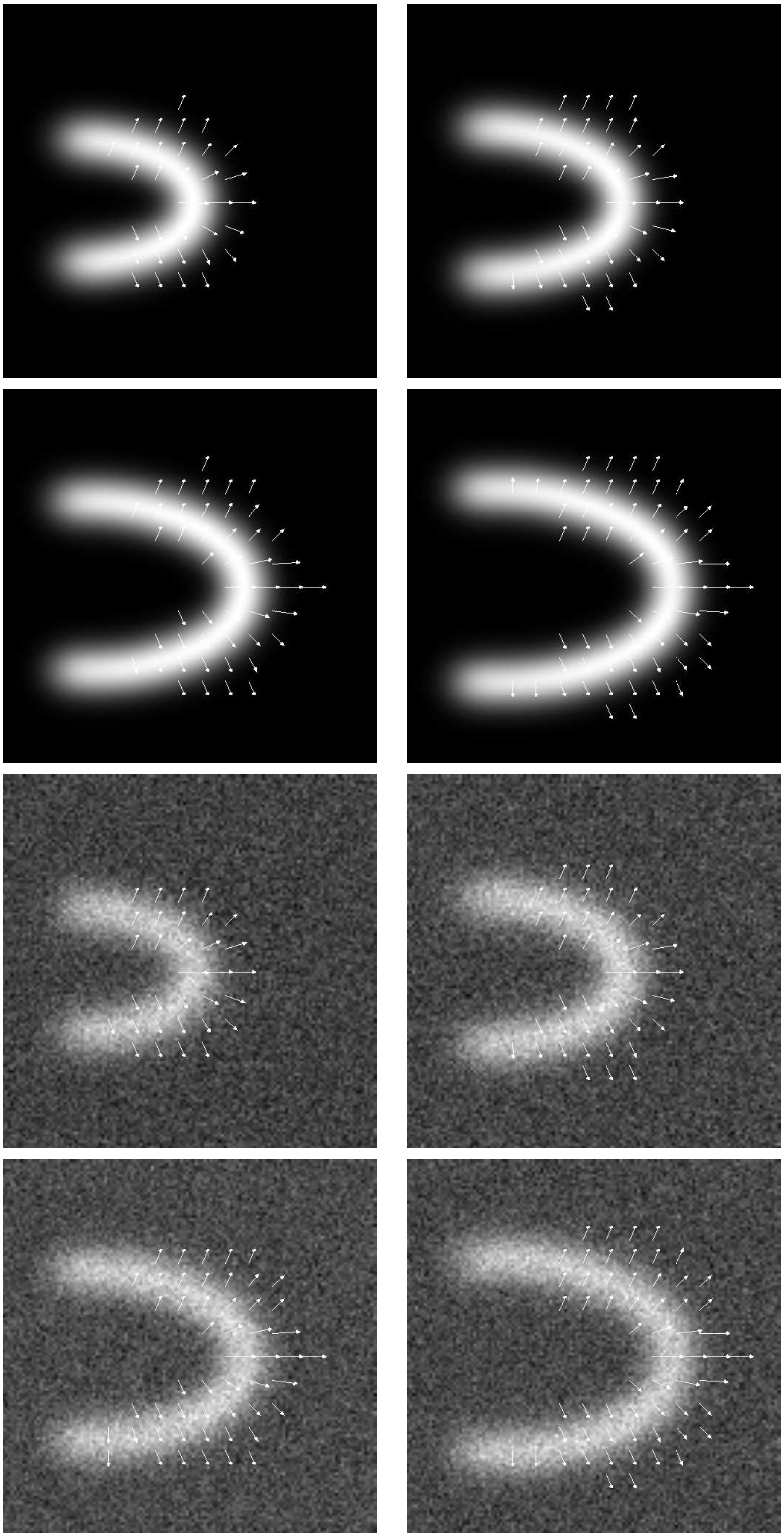

Figure 7.4: Result on synthetic data (upper part: original signal, lower part: signal and noise). The estimated velocity field is superimposed.

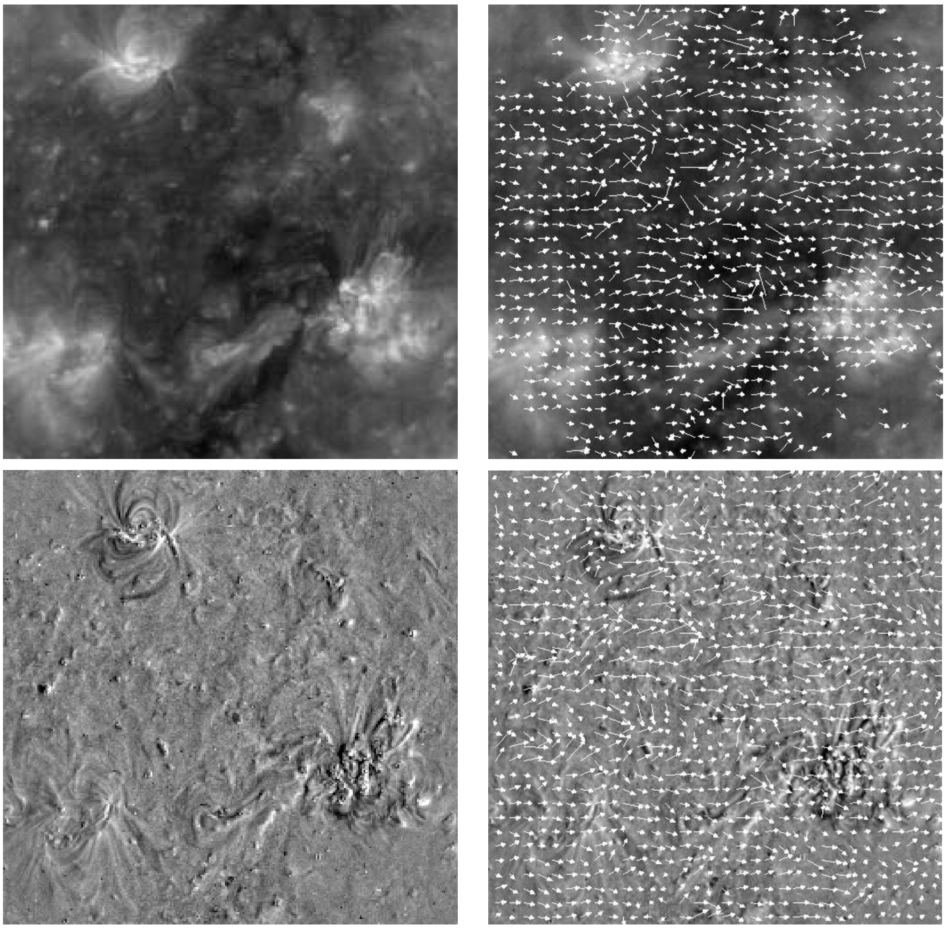

Figure 7.5: Results on real data. Upper right: the estimated flow using MTSTWT. Lower right: estimated flow using optical-flow Velociraptor.

Conclusion and Prospects

In this work, we have presented several algorithms of motion analysis. The first of them is based on a classic optical flow algorithm that is used to disentangle motion from brightness variation effect in Extreme Ultraviolet (EUV) difference images of observations of the solar atmosphere. It can be extended to longer sequence via a tracking algorithm applied to the detection of loop oscillations. The tracking algorithm, combined with stereoscopic reconstruction formula, is used to reconstruct an ondisc prominence observed by the Solar TErrestrial RElations Observatory (STEREO) imagers. Combined with basic Local Correlation Tracking (LCT), the tracking algorithm contributes to the analysis of the differential rotation in the Extreme ultraviolet Imaging Telescope (EIT) bandpasses and can be studied over the full 23rd solar cycle. Finally, a spatio-temporal Continuous Wavelet Transform (CWT) algorithm, named Motion-Tuned Spatio-Temporal Wavelet Transform, is shown to give promising results when compared with the optical flow computation. The algorithms presented in this thesis have their advantages and their drawbacks that we summarize in Table 7.1. The successful applications validate our approach when compared to existing methods of observations, based on the human visual system; the methods presented in this work do not require any interaction with human observers.

These techniques have been successfully applied to EIT images, as well as on Extreme UltraViolet Imager (EUVI) and Transition Region and Coronal Explorer (TRACE) images. The upcoming multiwavelength Atmospheric Imaging Assembly (AIA) onboard Solar Dynamics Observatory (SDO) images will require intense use of automatic algorithms to analyse all possible events present in the AIA data. The search for coronal loop oscillations is crucial to the attempt of probing the magnetic field, the temperature and the density parameters of the coronal plasma.

The Future Missions

Several crucial solar missions are planned in the near future and two of them will be of particular interest in the context of solar physics imaging processing techniques and motion estimation algorithms.

Algorithms	Velociraptor LK Optical Flow	CWT Local Maxima Tracking	Spatio-Temporal MTSTWT
Sequence length	two frames	more than two frames	long (min. 16 frames)
Number of parameters	two frames	one parameter	none
Aperture Problems	aperture reduction	none	inherent
BV Estimation	yes	possible	no

Table 7.1: Comparison of the motion analysis algorithms used in this study.

Solar Dynamics Observatory (SDO) is a multiwavelength and high temporal and spatial resolution imager planned to be launched in beginning of 2010.

With recent SoHO, TRACE, and Hinode missions, much progress has been made on the issues of structuring and dynamics in various regions of the solar atmosphere : transition region and "quiet" corona, coronal holes, active region loops. However, no clear conclusion could be drawn about the processes which determine their existence and their physics, especially their observed high temperatures or flows. The lack of sufficient spatial resolution at all observed wavelengths has prevented the study of the continuity between cool and hot, source and deposit, magnetic and non magnetic regions. For another reason, the study of the important regions of open magnetic field (mostly located at poles) has faced the severe drawback of observations performed from the ecliptic plane, except for (in-situ) ULYSSES measurements at a few astronomical units. We discuss the potential of discoveries offered by Solar Orbiter resulting notably from its spatial resolution performances and its capacity to fly above the ecliptic plane. We also stress how it is essential that remote sensing and in-situ measurements be coordinated.

Solar Orbiter The Solar Orbiter is a spacecraft which will follow an elliptic orbit very close to the Sun allowing an unprecedented view of the polar regions.

It will carry two instrument packages: it includes solar remote sensing instruments to directly view the Sun from close, high latitudes making observations of the solar atmosphere at high temporal and spatial resolutions, with the heliospheric in-situ instruments making measurements of the currently unexplored inner heliosphere. The exceptional orbits of the Solar Orbiter mission will allow us to achieve several breakthroughs in the EUV imaging of the solar atmosphere. In comparison with current instruments, a major advance is the possibility to obtain very high resolution images (while keeping moderate telescope dimensions) due to the position of the orbit perihelion close to the Sun (0.22 AU). Another major breakthrough will be achieved by taking the first ever images of the Sun from an out-of-ecliptic viewpoint (up to 34 degrees of solar latitude during the extended mission phase). Extreme Ultraviolet Imager (EUI) is a keystone instrument package of Solar Orbiter that will provide image sequences of solar atmospheric layers above the photosphere, thus offering the indispensable link between the solar surface and the outer corona which ultimately shapes the characteristics of the interplanetary medium. The Solar Orbiter spacecraft is not planned to be launched before 2017.

Kuafu is a Chinese project to establish a space weather forecast system composed of three satellites to be completed by 2012.

Proba2 is a Belgian satellite including an EIT-like EUV imager (SWAP) and a Lyman-Alpha radiometer (LYRA).

CORONAS-Photons CORONAS (Complex ORbital Observations Near-Earth of Activity of the Sun) is a Russian program for study of the Sun and solar-terrestrial connections physics by series of spacecrafts, which provides launching of three solar-oriented satellites onto the near-Earth orbit. CORONAS-PHOTON (or Koronas-Foton) is the third satellite in this series. Two previous missions of the project are CORONAS-I (launched on March 2, 1994) and CORONAS-F (launched on July 31, 2001). The CORONAS-PHOTON spacecraft was launched in January 2009.

Future Applications of Motion Estimation Softwares

Multi-wavelength Optical Flow Estimation

Such multiwavelength data will be provided by the SDO instrument. If we suppose the emitting plasma density varies with time and temperature, the intensity is given by

$$I(x - v \cdot \delta t, t + \delta t, \lambda_i) = \int K_{\lambda_i}(T)\phi(T - \alpha t, x - v \cdot \delta t, t)dT \ .$$

Measuring the displacement in space and temperature of the differential emission measure $\phi(T)$ may be achieved by inverting the relationship above but this is a difficult task. Another approach would be to assume the knowledge of the Differential Emission Measure (DEM) maps, for instance through the reconstruction of the DEM from the multiwavelength intensities at each image. The optical flow equation can be extended to the emission measure E_m through the following formula

$$D[E_m](\vec{dx}, dT, dt) = \frac{\partial E_m}{\partial t}dt + \vec{\nabla} E_m \cdot \vec{dx} + \frac{\partial E_m}{\partial T}dT \ . \tag{7.1}$$

Using the future SDO data, we can solve this equation by integrating over a local space-wavelength neighbourhood to retrieve the displacement $\vec{dx}$ and the variation of temperature dT of the emitting plasma volume.

Event Detection from Velocity Fields and Brightness Variation Maps

We aim to apply the motion estimation algorithm presented in Chapter 3 to detect specific events in high-cadence sequence of SDO data. This can be achieved by using the oscillation tracking method detailed in Chapter 5, but also via thresholding techniques of the maps estimated in Chapter 4 of motion and brightness variation. The error maps will contribute to the selection of regions containing interesting dynamical events detected using motion and brightness variations maps.

3D Tracking of Solar Features from STEREO EUV images

Combining the velocity estimation and the 3D estimation of solar atmospheric features presented in Chapter 6, one can for instance study further the tracking of the tracers over in sequence of images while estimating their altitude above the solar surface using the STEREO images to improve our knowledge of the differential rotation. It also enables to reconstruct routinely the 3D maps of the STEREO images in the 30.4 nm wavelength ; a thresholding method applied on these maps is a promising way of detecting and localizing the filaments on the solar disc visible in the 30.4 nm images of the upper chromosphere. Thus, a second important objective is to build a pioneering catalog of solar filaments detected in the 30.4 nm bandpass from the current STEREO archive.

Methods of Motion Analysis and Future Solar Missions

In the future solar missions, and in the context of the SDO archive of data of very great size, the routine of oscillation detection may be used to analyze routinely the sequence of SDO images. The cycle studies, as well as the STEREO and SDO images, require to use an optimized version of the optical flow algorithm. Recent improvements have made possible to compute the motion and Brightness Variation (BV) maps of an EIT pair of full-size images (1024^2 pixels) in ≈ 2 seconds using a C implementation on graphical processors, and thus approaching real-time computation. The algorithms introduced in this work, used as routines on data of existing and future solar missions, will contribute to answer the highly exciting solar physics mysteries, such as for instance the mechanisms that lead to the CMEs, filament eruptions, and flares, the nature of the magnetic reconnection on small scales reorganizing the large-scale field topology and current systems, as well as the determination of the mechanisms heating the corona and accelerating the solar wind.

Appendix A

Introduction to the Continuous Wavelet Transform

Applied on continuous signals, the CWT provides an overcomplete representation of the signals.

A.1 Fourier Transforms

A.1.1 1D Fourier Transform

In the 1D case, the Fourier transform $\mathcal{F}$ applied on a signal s is defined by

$$\hat{s}(k) = \mathcal{F}[s](k) = \frac{1}{\sqrt{2\pi}} \int_{\mathbb{R}} dx \ \exp^{-ikx} s(x) \ .$$

A.1.2 2D Fourier Transform

In the 2D case, the Fourier transform $\mathcal{F}$ applied on an image $I \in L^2(\mathbb{R}^2, d^2\vec{x})$ is defined by

$$\hat{I}(\vec{k}) = \mathcal{F}[I](\vec{k}) = \frac{1}{2\pi} \int_{\mathbb{R}^2} d^2\vec{x} \ \exp^{-i\vec{k}\cdot\vec{x}} s(\vec{x}) \ .$$

A.2 1D Continuous Wavelet Transform (CWT)

The wavelet transform projects a signal s onto a set of functions $\psi_{b,a}$ deriving from a "mother" wavelet ψ and depending on a translation b and a dilation parameter a. This local filtering in time (or in space) and in scale produces coefficients $S(a,b)$ that are non negligible only when the wavelet $\psi_{b,a}$ matches the signal. The wavelet transform filters the part of the signal, if any, that lives around the time (or space) b and the scale a. In 2D, one also adds the direction as a fourth parameter indexing the wavelets, unless the wavelet is isotropic. We will define the conditions on ψ and the

$\psi_{b,a}$ so that the transform is a continuous wavelet transform. For a comprehensive understanding of the CWT, the reader should consult [3].

A.2.1 1D Wavelet Transform

For a complex-valued signal $s \in L^2(\mathbb{R})$,

$$S(b,a) = \langle z|\psi_{\tau,s}\rangle \tag{A.1}$$

where $\psi_{\tau,s} = U\psi$ is a transformed version of the wavelet ψ by the transform operator U. The operator U is in fact the square integrable unitary and irreducible representation of the group defining the wavelet transform [see 3].

The wavelet transform mapping $W_\psi : s \mapsto c_\psi^{-1/2}\langle z|\psi_{\tau,s}\rangle$ has three essential properties: this mapping is a linear isometry.

Linearity

The wavelet transform is a linear transform by definition.

Covariance

The wavelet transform is covariant under translations and dilation:

$$\begin{aligned} W_\psi \qquad s(x-b_0) &\mapsto S(b-b_0,a) \\ a_0^{-1}s(x/a_0) &\mapsto S(a_0^{-1}b, a_0^{-1}a) \ . \end{aligned}$$

Energy Conservation

We have that $||S||^2 = c_\psi||s||^2$. Conversely, all these three conditions, plus some continuity, uniquely determine the wavelet transform defined in Equation A.1.

As a consequence of these properties, the mapping $W\psi$ is invertible.

Admissibility

The wavelet transform exists when the representation is admissible, namely that there exist an admissible wavelet. A wavelet is said to be admissible if the quantity c_ψ is finite, where

$$c_\psi = 2\pi \int_\infty^\infty dk \frac{|\hat{\psi}(k)|^2}{|k|} < \infty \ .$$

The admissibility condition is given by

$$0 < c_\psi < \infty \ .$$

In practice, this means that the wavelet should as a necessary condition have a zero mean function, and consequently be an oscillating function since

$$\hat{\psi}(0) = 0 \ .$$

Vanishing Moments

A wavelet ψ has N vanishing moments if

$$\int_{-\infty}^{\infty} x^N \psi(x) = 0 \ , \ n = 0, 1, \ldots, N \ .$$

This property improves the efficiency of ψ at detecting singularities in the signal , since it is then blind to polynomials up to order N, which constitutes the smoothest part of the signal.

A.2.2 The 1D Morlet Wavelet

The Morlet wavelet is defined as

$$\psi_{\mathrm{M}}(\tau) = \exp(ik_0\tau)\exp(-\frac{1}{2}\tau^2) + c(x) \ ,$$

and in the Fourier domain by

$$\hat{\psi}_{\mathrm{M}}(k) = \exp(-\frac{1}{2}(k-k_0)^2) + \hat{c}(k) \ .$$

The Morlet wavelet is well located in frequency: its support is concentrated around k_0. Its spatial support is wider and spreads more around the location of computation, as a consequence of the tradeoff between spatial and frequency supports. For a correct choice of $k_0 = 5.33$, one can neglect the correction term c that ensures the admissibility of the Morlet wavelet.

A.3 2D CWT

The 2D CWT of an image considered as a function I in $L^2(\mathbb{R}^2)$ is [2] $S = W_\psi I$.

$$W_I(\vec{b}, a, \theta) \quad = \quad \int_{\mathbb{R}^2} \mathrm{d}\vec{x}\ I(\vec{x})\, \psi^*_{\vec{b},a,\theta}(\vec{x}), \tag{A.2}$$

where $*$ denotes the complex conjugation, and $\psi_{\vec{b},a,\theta}$ is the shifted and dilated wavelet ψ in normalization L^1 given by

$$\psi_{\vec{b},a,\theta}(\vec{x}) \quad = \quad \frac{1}{a^2}\psi\Big(a^{-1}r_{-\theta}(\vec{x}-\vec{b})\Big), \tag{A.3}$$

for $\vec{b} \in \mathbb{R}^2$, $a \in \mathbb{R}^*_+$, and $\theta \in [0, 2\pi)$. If the wavelet is anisotropic, we can omit the index θ; the transform is then rotation-invariant. The main properties of the 2D wavelet transform are similar to the 1D CWT (linearity, covariance and energy conservation). They ensure the invertibility of the wavelet transform and the existence of the reproducing kernel.

A.3.1 2D Morlet Wavelet

The 2D Morlet Wavelet Transform is a directional wavelet transform: it means that one of its parameters (the direction) permits to correlate the signal with an elementary function that has a preferential direction. Thus, a high coefficient of the wavelet transform at a given parameter in direction. The Morlet wavelet is given by

$$\psi_{\mathrm{M}}(\vec{x}) = \exp(i\vec{k}_0 \cdot \vec{x}) \exp(-\frac{1}{2}|A\vec{x}|^2) + c(x) \ .$$

where c is the correction term that we neglect for $k \geq 5.6$ and $A = \mathrm{diag}[\epsilon^{-1/2}, 1]$ and $\epsilon\ ge1$ is the 2×2 anisotropy matrix.

A.3.2 2D Isotropic Mexican Hat (MH) Wavelet

The 2D MH wavelet is defined by:

$$\psi_{\mathrm{H}}(\vec{x}) \quad = \quad (2 - |\vec{x}|^2) e^{-|\vec{x}|^2/2} \ . \tag{A.4}$$

Like the wavelet itself, the Fourier transform of the MH is real and its analytical definition is:

$$\hat{\psi}_{\mathrm{H}}(\vec{k}) \quad = \quad |\vec{k}|^2 e^{-|\vec{k}|^2/2} \ . \tag{A.5}$$

It has been shown that the MH wavelet has an optimal sensitivity for Gaussian peaks on 1/f noise [56]. As in 1D, the Mexican Hat is known to have 2 vanishing moments so that any area of an image that can be approximated by a 0 or 1-degree polynomial function has vanishing wavelet coefficients. This filtering property allows to better detect singularities, e.g. spikes and peaks, and to a lesser extent elongated ridges such as magnetic loops. The wavelet coefficient maxima are found where the position and scale of the wavelet approach the most those of local features.

A.3.3 The Wavelet Local Maxima

The wavelet local maxima are defined, at a given scale a, by [56] the set of points $(\vec{b}(a), a)$ such that $\vec{b}(a)$ is a local maximum around $\vec{b}$ for a fixed a. Unless they are produced by the noise, these local maxima do in fact belong to the maxima lines that structure the images and along which one can analyze the regularity and the fractal dimension of the signal or the image [3].

A.4 Spatio-temporal Wavelet Transform

Definition A.4.1. Let s be a square integrable spatio-temporal signal $s \in L(\mathbb{R}^2 \times \mathbb{R}, d^2xdt)$. This means that $||s||^2 = \int_{\mathbb{R}^2\times\mathbb{R}} |s(x,t)|^2 d^2xdt < \infty$. The wavelet transform S is given by

$$S = \langle \psi_{\vec{b},\tau,a,\theta;c,\theta} | s \rangle \tag{A.6}$$

The spatio-temporal transform is defined by

$$S_\psi(\vec{b},\tau,\theta;a,c) = \iint_{\mathbb{R}^2\times\mathbb{R}} d^2\vec{x} s(\vec{x},t)\overline{\psi_{\theta,a,c}}(\vec{x}-\vec{b},t-\tau) \tag{A.7}$$

where $\psi_{\theta,a,c} = U\psi$ is the operator transform and $g = \{\vec{b},\tau,\theta;a,c\}$ are the parameters of the wavelet transform, namely the spatio-temporal translation $\vec{b},\tau$, θ is the spatial rotation and c is the modulus of the velocity vector (both give the "normal" velocity flow), and a is the spatial scale. The transform U applied to the signal s and the wavelet ψ in $L^2(\mathbb{R}^2, d^2\vec{x})$ can be decomposed into the following elementary operations: spatio-temporal shift T, rotation R, scaling D and speed tuning Λ, so that

$$\psi_{\vec{b},\tau,\theta;a,c} = U(\vec{b},\tau,\theta;a,c)\Psi$$
$$U(\vec{b},\tau,\theta;a,c) = T_{\vec{b},\tau}R_\theta D_\theta \Lambda_c \ .$$

If we require that the speed tuning transform is a unitary operation and keeps conserved the relation $\omega = \vec{k}\cdot\vec{v}$, then the operator U is given by

$$[U(\vec{b},\tau,\theta;a,c)\psi](\vec{x},t) = a^{-3/2}\psi(a^{-1}c^{-1/3}r_{-\theta}(\vec{x}-\vec{b}), a^{-1}c^{2/3}(t-\tau)) \ .$$

W_ψ is the linear map defined by

$$\begin{aligned} W_\psi \colon L^2(\mathbb{R}^2, d^2\vec{x}) &\longrightarrow \quad L^2(G,dg) \\ s &\longmapsto \quad c_\psi^{-1/2} S \ . \end{aligned}$$

The Spatio-temporal Morlet Wavelet

Let s be a square integrable spatio-temporal signal $s \in L_(\mathbb{R}^2\times\mathbb{R}, d^2xdt)$. This means that $||s||^2 = \int_{\mathbb{R}^2\times\mathbb{R}} |s(x,t)|^2 d^2xdt < \infty$. The wavelet transform S is given by

$$S = \langle \psi_{\vec{b},\tau,a,\theta;c,\theta} | s\rangle \ . \tag{A.8}$$

The spatio-temporal wavelet, as proposed in [3], is given in the spatio-temporal domain by

$$\psi_{\vec{x},t} = (e^{(i\vec{k}_0\cdot A^{-1}\vec{x})}e^{(-\frac{1}{2}|A^{-1}\vec{x}|^2)} - e^{-\frac{1}{2}|A^{-1}\vec{x}|^2}e^{-\frac{1}{2}|\vec{k}_0|^2}) \times (e^{i\omega_0 t}e^{-\frac{1}{2}t^2} - e^{-\frac{1}{2}t^2}e^{-\frac{1}{2}\omega_0^2}) \ .$$

and in the wavenumber-frequency domain by

$$\hat{\psi}(\vec{k},\omega) = (e^{(-\frac{1}{2}|A\vec{k}-\vec{k}_0|^2)} - e^{(-\frac{1}{2}(|A\vec{k}|^2+|\vec{k}_0|^2))})(e^{-\frac{1}{2}(\omega-\omega_0)^2} - e^{-\frac{1}{2}(\omega^2+\omega_0^2)})$$

where A is the anisotropy matrix. The second term (correction terms) in both formula vanishes for $|veck_0| \geq 5.6$. This continuous wavelet transform shares with the 2D CWT the properties of linearity, covariance, and energy conservation so that its mapping W_ψ also is an isometry from the space of signals into the space of wavelet transforms, thus it is invertible on its range and has an exact reconstruction formula. We do not use this property here. In the computations, we apply a 3D Fast Fourier Transform (FFT) to the signal that we multiply by the Fourier domain version of the spatio-temporal wavelet transform.

Appendix B

Some Properties of Motion Estimation

B.1 Properties of Optical-flow

B.1.1 Symmetric Optical Flow and Equivalence with Lucas' Symmetric Flow.

This formulation is equivalent to Lucas' formulation of symmetric optical flow. Our probabilistic approach shows that the role of the symmetric approach is to estimate the motion of the mean image $1/2(I_1 + I_2)$ regularization against texture variation. The formula proposed by [68] for a symmetric optical flow is based on the symmetry between both Optical Flow Constraint Equation (OFCE) equations. Indeed we can impose that

$$
\begin{aligned}
I_2(\vec{x} + \delta\vec{x}) &= I_1(\vec{x}) \ , \\
I_1(\vec{x} - \delta\vec{x}) &= I_2(\vec{x}) \ .
\end{aligned}
$$

Thus, a symmetric optical flow is obtained by minimizing

$$\sum (I_2(\vec{x} + \delta\vec{x}) - I_1(\vec{x}))^2 + \sum (I_1(\vec{x} - \delta\vec{x}) - I_2(\vec{x}))^2 \ . \tag{B.1}$$

The solution to this problem, in the 1-D case is

$$\delta x = \frac{\sum (I_1 - I_2)(I_{1x} - I_{2x})}{\sum I_{1x}^2 + I_{2x}^2} \ . \tag{B.2}$$

We will give a better interpretation of the symmetric optical flow. As noted by [68], "*whether this symmetric version provides any significant advantage over the asymmetric version is an open question*". A similar formula gives the solution in the 2-D case.

B.1.2 Relation between Q and Theoretical Covariance

The quality value Q is related to the theoretical covariance, *i.e.* the diagonal elements $\mathbf{V}_{\hat{\theta},\mathbf{ii}} = \sigma^{\mathbf{2}}_{\hat{\theta}_{\mathbf{i}}}$ of $\mathbf{V}_{\hat{\theta}}$, by the following relation:

$$Q \leq \frac{1}{\max \sigma^2_{\hat{\theta}_i}} \ .$$

B.1.3 Optical Flow Constraint Equation (OFCE) in nD (n dimensions)

There are two equivalent formulations of the OFCE.

Intensity Conservation

The Partial Differential Equation (PDE) approach considers the image intensity $I(\vec{x}(t), t)$, where $\vec{x} = (x_1, ..., x_n)^T$, as a physical quantity that is conserved over time. This statement is formulated in the transport OFCE equation:

$$\frac{dI}{dt}(\vec{x}(t), t) = \sum_i \frac{dx_i}{dt} \times \frac{\partial I}{\partial x_i} + \frac{\partial I}{\partial t} \ . \tag{B.3}$$

The assumption that intensity I does not vary over time, and that intensity variations observed in difference images is only due to motion, implies that

$$\frac{dI}{dt} = 0 \ .$$

The temporal and spatial derivatives can be approximated using finite difference scheme. The motion of the structure implies that: $\vec{x}(t)$ is mapped to $\vec{x}(t + \delta t) = \vec{x}(t) + \frac{\partial x}{\partial t}\delta t$.

$$\frac{\partial I}{\partial t} \simeq \frac{\delta I}{\delta t} = \frac{I(\vec{x}(t+\delta t), t+\delta t) - I(\vec{x}(t), t)}{\delta t} \tag{B.4}$$

$$= \frac{I(\vec{x}(t) + \frac{dx}{dt}\delta t, t+\delta t) - I(\vec{x}(t), t)}{\delta t} \tag{B.5}$$

The equation is then discretized , assuming that $\delta t = 1$, Equation (B.5) becomes:

$$\begin{aligned} 0 &\simeq \sum_i \frac{\delta x_i}{\delta t} \times \frac{\partial I}{\partial x_i} + \frac{\delta I}{\delta t} \\ &= \sum_i \delta x_i \times \frac{\partial I}{\partial x_i} + I_2 - I_1 \end{aligned}$$

In this approach,the spatial derivative of image I can be either computed in image I_1 or I_2.

B.1.4 Discretization Error

The discretized OFCE is:

$$\nabla\tilde{I}\cdot\vec{v}+\frac{\delta\tilde{I}}{\delta t}=\xi(\vec{x},\delta t), \tag{B.6}$$

where $\delta\tilde{I}=\tilde{I}_2(\vec{x})-\tilde{I}_1(\vec{x})=g_a\star\delta I$. The order of the discretization error (different from the model error) is [see 83]:

$$\xi(\vec{x},\delta t)\sim\delta t\frac{\partial^2\tilde{I}}{\partial t^2}.$$

In this first approach, the spatial derivatives can be computed from either image I_1 and/or I_2. In the case of image registration, the order of error due to the truncation of higher order terms is:

$$\xi(\vec{x},\delta\vec{x})\sim\delta\vec{x}^{\mathrm{T}}H_{\tilde{I}}\,\delta\vec{x},$$

where $H_{\tilde{I}}$ is the Hessian matrix of $\tilde{I}$.

B.1.5 Motion Models (2D) and Matrix Notations

Here we show the matrix formulation of the optical flow for $n=2$. We write the motion model (local translation) using matrices:

$$\delta\vec{x}=\begin{pmatrix}1&0\\0&1\end{pmatrix}\times\begin{pmatrix}c_x\\c_y\end{pmatrix}=\begin{pmatrix}c_x\\c_y\end{pmatrix}.$$

More generally, for a polynomial motion model (affine motion model):

$$\delta\vec{x}=P\times C=\begin{pmatrix}1&x_i&y_i&0&0&0\\0&0&0&1&x_i&y_i\end{pmatrix}\times\begin{pmatrix}c_0&c_1&c_2&c_3&c_4&c_5\end{pmatrix}^T.$$

In our applications, coefficients of the vector $\vec{C}$ are dimensionless coefficient whereas the coefficients of P, which are the motion parameters, are expressed in units of displacement, in our case, in pixels ($1=\Delta x$, the spatial unit in which the displacement is expressed).

Eigenvalues $\lambda_\pm$

To invert the symmetric matrix A^TA, we first diagonalize it into : $P^{-1}DP$ where

$$D=\begin{bmatrix}\lambda_1&0\\0&\lambda_2\end{bmatrix}. \tag{B.7}$$

where $\lambda_1>\lambda_2$ In the algorithm, this matrix is computed via the IDL procedure *eigenql*. We can express the eigenvalues in terms of image derivatives I_x :

$$\lambda_\pm(\alpha)=\frac{1}{2}\times(\alpha^2+\sum g_i^2I_x^2\pm((\alpha^2-\sum g_i^2I_x^2)^2+4\times(\alpha\sum g_i^2I_x)^2)^{\frac{1}{2}}). \tag{B.8}$$

The existence of these two eigenvalues is related to the $1D$ aperture problem in the intensity derivative-intensity variation plane. It can be seen that the inversion of the system depends on the term $(\sum g_i^2 I_x)^2)$. As $(\sum g_i^2 I_x)^2 \leq \sum g_i^2 I_x^2$, we can check that if α^2 is large compared to $\sum g_i^2 I_x^2$, then we have the obvious eigenvalues :

$$\lambda_\pm(\alpha) = \alpha^2 \text{ or } \sum g_i^2 I_x^2 \ .$$

The consequence in numerical applications is that these eigenvalues are relevant to the study of texture in simultaneous v and bv estimations if the condition $\alpha^2 \gg \sum g_i^2 I_x^2$ is not satisfied. In this case, the ratio λ_+/λ_-, which is called the conditioning number, is used to ensure that the matrix is invertible. High values of the conditioning number indicate that the signal texture within the window of observation Ω is well adapted to simultaneous v/bv estimation. It is there that we avoid the aperture problem. In practice, as noted by Shi and Tomasi [97] λ_+ is bounded, at maximum due to the dynamics of the signal (quantification or finite number of encoded bits), and the minimum value is reached when $\lambda_- = \lambda_+$. The minimum value is given by :

$$\frac{1}{2}\mathbf{trace}(A^T A) = \frac{\lambda_+ + \lambda_-}{2} = \frac{1}{2}(\alpha^2 + \sum g_i^2 I_x^2) \ .$$

An even finer lower boundary value is :

$$\max(\alpha^2, \sum g_i^2 I_x^2) \ .$$

Finally , boundary values of $\lambda_{\max}$ are given by :

$$\max(\alpha^2, \sum g_i^2 I_x^2) \leq \lambda_{\max} \leq \alpha^2 + I_{x,\max}^2 \ .$$

In practice, as the spatial derivative is computed using finite difference (IDL *deriv* function, 3-points Lagrange method), we state that

$$I_{x,\max} = \max\{\frac{1}{2}(I(x+1) - I(x-1)), x \in \Omega\} \ .$$

It is obvious that this value is in general far below the maximum allowed value

$$\max\{I(x), x \in \Omega\} - \min\{I(x), x \in \Omega\} \ .$$

due to the spatial continuity of the signal I. Stronger values are expected when the neighborhood Ω contains discontinuity such as edges. Similarly, boundary values for $\lambda_{\min}$ are given by :

$$0 \leq \lambda_{\min} \leq \min(\alpha^2, \sum g_i^2 I_x^2) \ .$$

The boundary values (upper for $\lambda_{\min}$, lower for $\lambda_{\max}$) are reached when $\sum g_i^2 I_x = 0$. This case occurs when the intensity pattern is symmetric (maximum variance of texture gradients) within the window of observation. In this case the convexity of the pattern allows for a simultaneous observation of distinct velocity and brightness variation parameters (see figure) : the aperture effect vanishes.

Texture Analysis

In this section we study the behavior of our definition of the texture for the motion analysis, Before computing deformation, a strong change in texture between signals can be detected between signals I_1 and I_2. A statistic test is carried out on the random variable $T' = \sum g_i^2 I_{2x}^2 - \sum g_i^2 I_{1x}^2$. Assuming that the spatial derivative I_x is a Gaussian white noise $(I_x \sim N(0, \sigma_d^2))$, and that I_{1x} and I_{2x} are uncorrelated, the mean $\mu_{T'}$ and the variance $\sigma_{T'}^2$ of T' are equal to

$$\begin{aligned} \mu_{T'} &= 2\sigma_d^2 \ , \\ \sigma_{T'}^2 &= 4\sigma_d^4 \ . \end{aligned}$$

Similarly, a median filter could be applied to the difference image within the neighborhood to detect outliers such as cosmic ray hits (CRHs).

Eigenvectors

The eigenvectors of the matrix P indicate how to combine the variables v and δI to diagonalize the matrix $A^T A$:

$$p = [p_1 p_2] \ .$$

B.1.6 Calibration and Analysis of Quality Index

Error

As noted by Okutomi and Kanade, the error on disparity field is the addition of two different random variables: the statistical error ϵ_I and the systematic error ϵ_{II} . We can model the residual error by:

$$\epsilon = \epsilon_I + \epsilon_{II} \ .$$

We assume $\epsilon_I \sim N(0, 2\sigma^2)$ where σ^2 is the variance of the Gaussian additive random noise on images I_1 and I_2. When the size of the observation window increases, the residual ϵ_I decreases, because it has a higher signal to noise ratio, whereas ϵ_{II} tends to increase because the assumption of local constant deformation parameters is no longer valid.

B.1.7 Multiscale Update and Refinement of Quality

The multiscale update procedure of the quality will improve the predicted relative error at the condition that the quality is improved at the finer scale.

B.1.8 Calibration of Error

In order to predict correctly the error on our estimate of motion, we have set up a procedure for calibrating the error function. Our goal is to relate empirically the error measured on estimations of synthetic textures and prescribed parameters of motion and brightness variation to the quality index. The quality, as defined in 3.4 is obtained using the estimated covariance matrix of the linear least-squares estimation. This relationship may vary according to the parameters to estimate (here, the velocity and the BV). As we would like this calibration to be achieved on various types of solar textures, we designed a procedure to generate these textures; the goal is to generate the textures in a wide range of value T (defined in Section 3.4), and to degrade the signal by adding noise, so that the residual or the dissimilarity S also varies and that the law of error is meaningful for several values of texture and dissimilarity.

The range of solar-like textures are generated by applying a continuous wavelet transform on a white noise image. By changing the spatial scale of the CWT, one obtains significant changes on the value of the texture parameter T.

B.2 Tracking Theorems

B.2.1 Low-pass Filtering of the Periodic Signal

We smooth the periodic signals to obtain the "trend‘" of the periodic signal by removing the periodic component of the signal. If S_1 and S_2 are respectively the trend an the oscillatory component of the signal of period T, we have that

$$\begin{aligned} S &= S_1 + S_2 \ , \\ F[S] &= F[S_1] + F[S_2] \ , \end{aligned}$$

where F is a smoothing low-pass filter. We choose the frequency of the filter using our prior knowledge on the period T of the signal, obtained from a simple Morlet 1D wavelet analysis. Then all components of the signal S that have an oscillation frequency greater are removed by the smoothing filter F. has the effect of removing the frequency components greater than $1/T$. For our application, we use a basic "sync" filter (or local mean filter).

B.3 Preprocessing Procedures and Data Format

Most of the Interactive Data Language (IDL) procedures to calibrate and pre-process data are available in the Solar Soft libraries and that are developed by the solar physics community. The data used in this work have been preprocessed by the procedures *eit_prep.pro*, *trace_prep.pro*, and *secchi_prep.pro* of the solarsoft. EUV data are stored as floating point images in *.fits* files which is a NASA file format of image.

Bibliography

[1] Antoine, J.-P. 1996. Symmetry-adapted wavelet analysis. Proc. IEEE Intern. Conf. on Image Processing, III:177–180.

[2] Antoine, J.-P., Carrette, P., Murenzi, R., and Piette, B. 1993. Image analysis with two dimensional continuous wavelet transform. Signal Proc., 31:241–272.

[3] Antoine, J.-P., Murenzi, R., Vandergheynst, P., and Ali, S. 2004. *Two-Dimensional Wavelets and their Relatives.*. Cambridge University Press.

[4] Aschwanden, M. J. 2004. *Physics of the Solar Corona. An Introduction*. Physics of the Solar Corona.

[5] Aschwanden, M. J., Fletcher, L., Schrijver, C. J., and Alexander, D. 1999. Coronal Loop Oscillations Observed with the Transition Region and Coronal Explorer. ApJ, 520:880–894.

[6] Barra, V., Delouille, V., Hochedez, J.-F., and Chainais, P. 2005. Segmentation of EIT Images Using Fuzzy Clustering: a Preliminary Study. In *The Dynamic Sun: Challenges for Theory and Observations*, volume 600 of *ESA Special Publication*.

[7] Barra, V., Delouille, V., Kretzschmar, M., and Hochedez, J. F. 2009. Fast and robust segmentation of solar EUV images: algorithm and results for solar cycle 23. A&A.

[8] Barron, J., Fleet, D., Beauchemin, S., and Burkitt, T. 1992. Performance Of Optical Flow Techniques. CVPR, 92:236–242.

[9] Beckers, J. M. 1968. Solar Spicules (Invited Review Paper). Sol. Phys., 3:367–433.

[10] Benz, A. 2002. *Plasma Astrophysics, second edition*, volume 279 of *Astrophysics and Space Science Library*. Kluwer.

[11] Berghmans, D. and Clette, F. 1999. Active region EUV transient brightenings - First Results by EIT of SOHO JOP80. Sol. Phys., 186:207–229.

[12] Berghmans, D., Clette, F., and Moses, D. 1998. Quiet Sun EUV transient brightenings and turbulence. A panoramic view by EIT on board SOHO. A&A, 336:1039–1055.

[13] Berghmans, D., McKenzie, D., and Clette, F. 2001. Active region transient brightenings. A simultaneous view by SXT, EIT and TRACE. A&A, 369:291–304.

[14] Black, M. and Anandan, P. 1993. A Framework for the Robust Estimation of Optical Flow. In *ICCV93*, pages 231–236.

[15] Brajša, R., Wöhl, H., Vršnak, B., Ruždjak, V., Clette, F., and Hochedez, J.-F. 2001. Solar differential rotation determined by tracing coronal bright points in SOHO-EIT images. I. Interactive and automatic methods of data reduction. A&A, 374:309–315.

[16] Brajša, R., Wöhl, H., Vršnak, B., Ruždjak, V., Clette, F., and Hochedez, J.-F. 2002. Solar differential rotation determined by tracing coronal bright points in SOHO-EIT images. II. Results for 1998/99 obtained with interactive and automatic methods. A&A, 392:329–334.

[17] Brajša, R., Wöhl, H., Vršnak, B., Ruždjak, V., Clette, F., Hochedez, J.-F., and Roša, D. 2004. Height correction in the measurement of solar differential rotation determined by coronal bright points. A&A, 414:707–715.

[18] Brajša, R., Wöhl, H., Ruždjak, D., Vršnak, B., Verbanac, G., Svalgaard, L., and Hochedez, J.-F. 2007. On the solar rotation and activity. Astronomische Nachrichten, 328:1013–+.

[19] Brault, P. 2005. *Segmentation d'image et estimation de mouvement*. Ph.D. thesis, Univertisté Paris-Sud XI.

[20] Brekke, P., Kjeldseth-Moe, O., Brynildsen, N., Maltby, P., Haugan, S. V. H., Harrison, R. A., Thompson, W. T., and Pike, C. D. 1997. Flows and Dynamics in the Corona Observed with the Coronal Diagnostic Spectrometer (cds). Sol. Phys., 170:163–177.

[21] Chainais, P. 2007. Infinitely Divisible Cascades to Model the Statistics of Natural Images. 29(12):2105–2119.

[22] Corpetti, T., Mémin, É., and Pérez, P. 2002. Dense Estimation of Fluid Flows. IEEE Trans. Pattern Anal. Mach. Intell., 24(3):365–380.

[23] De Groof, A., Berghmans, D., van Driel-Gesztelyi, L., and Poedts, S. 2004. Intensity variations in EIT shutterless mode: Waves or flows? A&A, 415:1141–1151.

[24] De Pontieu, B., Hansteen, V. H., Rouppe van der Voort, L., van Noort, M., and Carlsson, M. 2007. High-Resolution Observations and Modeling of Dynamic Fibrils. ApJ, 655:624–641.

[25] Deforest, C. E. 2004. On Re-sampling of Solar Images. Sol. Phys., 219:3–23.

[26] Deforest, C. E. and Gurman, J. B. 1998. Observation of Quasi-periodic Compressive Waves in Solar Polar Plumes. ApJ, 501:L217+.

[27] DeForest, C. E., Hagenaar, H. J., Lamb, D. A., Parnell, C. E., and Welsch, B. T. 2007. Solar Magnetic Tracking. I. Software Comparison and Recommended Practices. ApJ, 666:576–587.

[28] Delaboudinière, J.-P., Artzner, G. E., Brunaud, J., Gabriel, A. H., Hochedez, J. F., Millier, F., Song, X. Y., Au, B., Dere, K. P., Howard, R. A., Kreplin, R., Michels, D. J., Moses, J. D., Defise, J. M., Jamar, C., Rochus, P., Chauvineau, J. P., Marioge, J. P., Catura, R. C., Lemen, J. R., Shing, L., Stern, R. A., Gurman, J. B., Neupert, W. M., Maucherat, A., Clette, F., Cugnon, P., and van Dessel, E. L. 1995. EIT: Extreme-Ultraviolet Imaging Telescope for the SOHO Mission. Sol. Phys., 162:291–312.

[29] Delouille, V., de Patoul, J., Hochedez, J. F., Jacques, L., and Antoine, J. P. 2005. Wavelet Spectrum Analysis Of Eit/Soho Images. Sol. Phys., 228:301–321.

[30] Dere, K. P., Moses, J. D., Delaboudinière, J.-P., Brunaud, J., Carabetian, C., Hochedez, J.-F., Song, X. Y., Catura, R. C., Clette, F., and Defise, J.-M. 2000. The Preflight Photometric Calibration of the Extreme-Ultraviolet Imaging Telescope EIT. Sol. Phys., 195:13–44.

[31] Duval-Destin, M. 1991. *Analyse spatiale et spatio-temporelle de la perception visuelle ‘a l’aide de la transform’ee en ondelettes*. Ph.D. thesis.

[32] Feng, L., Inhester, B., Solanki, S. K., Wiegelmann, T., Podlipnik, B., Howard, R. A., and Wuelser, J.-P. 2007. First Stereoscopic Coronal Loop Reconstructions from STEREO SECCHI Images. ApJ, 671:L205–L208.

[33] Filippov, B. and Koutchmy, S. 2002. About the prominence heating mechanisms during its eruptive phase. Sol. Phys., 208:283–295.

[34] Filippov, B. P. and Den, O. G. 2001. A critical height of quiescent prominences before eruption. J. Geophys. Res., 106:25177–25184.

[35] Fleet, D. and Weiss, Y. 2005. *Mathematical Models in Computer Vision: The Handbook*, chapter 15, pages 239–258. Springer.

[36] Foukal, P. 1987. Active region flows. In Athay, G. and Spicer, D. S., editors, *Theoretical Problems in High Resolution Solar Physics*, pages 15–35.

[37] Foukal, P. V. 2004. *Solar Astrophysics, 2nd, Revised Edition*. Solar Astrophysics, 2nd, Revised Edition, by Peter V. Foukal, pp. 480. ISBN 3-527-40374-4. Wiley-VCH , April 2004.

[38] Gabriel, A. H. 1976. A magnetic model of the solar transition region. Royal Society of London Philosophical Transactions Series A, 281:339–352.

[39] Gissot, S. and Hochedez, J.-F. 2008. Oscillation analysis using optical flow: Application to an EUV movie of the solar corona. Statistical Methodology, 5:340–349.

[40] Gissot, S. F. and Hochedez, J.-F. 2007. Multiscale optical flow probing of dynamics in solar EUV images. Algorithm, calibration, and first results. A&A, 464:1107–1118.

[41] Gissot, S. F., Hochedez, J.-F., Dibos, F., Brajša, R., Jacques, L., Berghmans, D., Zhukov, A., Clette, F., Wöhl, H., and Antoine, J.-P. 2003. Extracting the apparent motion from two successive EIT images. In Wilson, A., editor, *Solar Variability as an Input to the Earth's Environment*, volume 535 of *ESA Special Publication*, pages 853–856.

[42] Gissot, S. F., Hochedez, J.-F., Chainais, P., and Antoine, J.-P. 2008. 3D Reconstruction from SECCHI-EUVI Images Using an Optical-Flow Algorithm: Method Description and Observation of an Erupting Filament. Sol. Phys., 252:397–408.

[43] Golub, L. and Pasachoff, J. M. 1997. *The Solar Corona*. The Solar Corona, by Leon Golub and Jay M. Pasachoff, pp. 388. ISBN 0521480825. Cambridge, UK: Cambridge University Press, September 1997.

[44] Golub, L., Bookbinder, J., Deluca, E., Karovska, M., Warren, H., Schrijver, C. J., Shine, R., Tarbell, T., Title, A., Wolfson, J., Handy, B., and Kankelborg, C. 1999. A new view of the solar corona from the transition region and coronal explorer (TRACE). Physics of Plasmas, 6:2205–2216.

[45] Handy, B. N., Acton, L. W., Kankelborg, C. C., Wolfson, C. J., Akin, D. J., Bruner, M. E., Caravalho, R., Catura, R. C., Chevalier, R., Duncan, D. W., Edwards, C. G., Feinstein, C. N., Freeland, S. L., Friedlaender, F. M., Hoffmann, C. H., Hurlburt, N. E., Jurcevich, B. K., Katz, N. L., Kelly, G. A., Lemen, J. R., Levay, M., Lindgren, R. W., Mathur, D. P., Meyer, S. B., Morrison, S. J., Morrison, M. D., Nightingale, R. W., Pope, T. P., Rehse, R. A., Schrijver, C. J., Shine, R. A., Shing, L., Strong, K. T., Tarbell, T. D., Title,

A. M., Torgerson, D. D., Golub, L., Bookbinder, J. A., Caldwell, D., Cheimets, P. N., Davis, W. N., Deluca, E. E., McMullen, R. A., Warren, H. P., Amato, D., Fisher, R., Maldonado, H., and Parkinson, C. 1999. The transition region and coronal explorer. Sol. Phys., 187:229–260.

[46] Hassler, D. M., Rottman, G. J., and Orrall, F. Q. 1991. Systematic radial flows in the chromosphere, transition region, and corona of the quiet sun. ApJ, 372:710–718.

[47] Henze, W. and Dupree, A. K. 1973. Solar Rotation in the Chromosphere and Corona. Sol. Phys., 33:425–429.

[48] Hildreth, E. 1984. *The measurement of visual motion*. MIT Press.

[49] Hochedez, J.-F., Clette, F., Verwichte, E., Berghmans, D., and Cugnon, P. 2001. Long Term Variations in the Extreme UV Corona: the EIT/SoHO perspective. In Brekke, P., Fleck, B., and Gurman, J. B., editors, *Recent Insights into the Physics of the Sun and Heliosphere: Highlights from SOHO and Other Space Missions*, volume 203 of *IAU Symposium*, pages 501–+.

[50] Hochedez, J. F., Zhukov, A., Robbrecht, E., Van der Linden, R., Berghmans, D., Vanlommel, P., Theissen, A., and Clette, F. 2005. Solar weather monitoring. Annales Geophysicae, 23:3149–3161.

[51] Horn, B. and Schunck, G. 1981. Determining optical flow. Artificial Intelligence, 17:185–203.

[52] Howard, R. and Harvey, J. 1970. Spectroscopic Determinations of Solar Rotation. Sol. Phys., 12:23–51.

[53] Hudson, H. S. and Cliver, E. W. 2001. Observing coronal mass ejections without coronagraphs. J. Geophys. Res., (15):25199–25214.

[54] Inhester, B. 2006. Stereoscopy basics for the STEREO mission. ArXiv Astrophysics e-prints.

[55] Inhester, B., Feng, L., and Wiegelmann, T. 2008. Segmentation of Loops from Coronal EUV Images. Sol. Phys., 248:379–393.

[56] Jacques, L. 2004. *Ondelettes, repères et couronne solaire*. Ph.D. thesis, Université catholique de Louvain.

[57] Kaiser, M. L., Kucera, T. A., Davila, J. M., St. Cyr, O. C., Guhathakurta, M., and Christian, E. 2007. The STEREO Mission: An Introduction. Space Science Reviews, pages 198–+.

[58] Kamide, Y. and Chian, A. C.-L. 2007. *Handbook of the Solar-Terrestrial Environment*. Springer.

[59] Klimchuk, J. A., Tanner, S. E. M., and De Moortel, I. 2004. Coronal Seismology and the Propagation of Acoustic Waves along Coronal Loops. ApJ, 616:1232–1241.

[60] Krijger, J. M. and Roudier, T. 2003. Photospheric flows measured with TRACE II. Network formation. A&A, 403:715–723.

[61] Krijger, J. M., Roudier, T., and Rieutord, M. 2002. Photospheric flows measured with TRACE. A&A, 387:672–677.

[62] Kucera, T. A., Tovar, M., and De Pontieu, B. 2003. Prominence Motions Observed at High Cadences in Temperatures from 10000 to 250000 K. Sol. Phys., 212:81–97.

[63] Leduc, J.-P., Mujica, F., Murenzi, R., and Smith, M. 1997. Spatio-temporal wavelet transforms for motion tracking. In *Proc. IEEE International Conference on Acoustics, Speech, and Signal Processing ICASSP-97*, volume 4, pages 3013–3016.

[64] Lemaire, J. and Pierrard, V. 2001. Kinetic Models of Solar and Polar Winds. Ap&SS, 277:169–180.

[65] Lippincott, S. L. 1955. A preliminary investigation of the small changes in the chromospheric structure. Annales d'Astrophysique, 18:113–+.

[66] Longcope, D. W. 2004. Inferring a Photospheric Velocity Field from a Sequence of Vector Magnetograms: The Minimum Energy Fit. ApJ, 612:1181–1192.

[67] Lucas, B. and Kanade, T. 1981. An Iterative Image Registration Technique with an Application to Stereo Vision. In *IJCAI81*, pages 674–679.

[68] Lucas, B. D. 1984. *Generalized Image Matching by the Method of Differences*. Ph.D. thesis, Robotics Institute, Carnegie Mellon University, Pittsburgh, PA.

[69] Mariska, J. T. 1992. *The solar transition region*. Cambridge Astrophysics Series, New York: Cambridge University Press, —c1992.

[70] Moses, D., Clette, F., Delaboudinière, J.-P., Artzner, G. E., Bougnet, M., Brunaud, J., Carabetian, C., Gabriel, A. H., Hochedez, J. F., Millier, F., Song, X. Y., Au, B., Dere, K. P., Howard, R. A., Kreplin, R., Michels, D. J., Defise, J. M., Jamar, C., Rochus, P., Chauvineau, J. P., Marioge, J. P., Catura, R. C., Lemen, J. R., Shing, L., Stern, R. A., Gurman, J. B., Neupert, W. M., Newmark, J., Thompson, B., Maucherat, A., Portier-Fozzani, F., Berghmans,

D., Cugnon, P., van Dessel, E. L., and Gabryl, J. R. 1997. EIT Observations of the Extreme Ultraviolet Sun. Sol. Phys., 175:571–599.

[71] Mujica, F., Leduc, J.-P., Murenzi, R., and Smith, M. 2000. A new motion parameter estimation algorithm based on the continuous wavelet transform. 9(5):873–888.

[72] Mujica, F., Murenzi, R., Smith, M., and Park, S.-I. 2000. Motion estimation using the spatio-temporal continuous wavelet transform: new results and alternative implementations. In *Proc. International Conference on Image Processing*, volume 2, pages 550–553.

[73] Newton, H. W. and Nunn, M. L. 1951. The Sun's rotation derived from sunspots 1934-1944 and additional results. MNRAS, 111:413–+.

[74] Noglik, J. B., Walsh, R. W., and Ireland, J. 2005. Indirect calculation of the magnetic reconnection rate from flare loops. A&A, 441:353–360.

[75] November, L. J. and Simon, G. W. 1988. Precise proper-motion measurement of solar granulation. ApJ, 333:427–442.

[76] Odobez, J.-M. and Bouthemy, P. 1995. Robust multiresolution estimation of parametric motion models. Journal of Visual Communication and Image Representation, 6(4):348–365.

[77] Okutomi, M. and Kanade, T. 1990. A Locally Adaptive Window for Signal Matching. In *Proceedings of the Third International Conference on Computer Vision (ICCV '90)*, pages 190–199.

[78] Park, S. and Schowengerdt, R. 1983. Image Reconstruction by Parametric Cubic Convolution. Computer Vision, Graphics & Image Processing, 23:256.

[79] Periaswamy, S. and Farid, H. 2003. Elastic Registration in the Presence of Intensity Variations. IEEE Transactions on Medical Imaging, 22(7):865–874.

[80] Peter, H., Gudiksen, B. V., and Nordlund, Å. 2006. Forward Modeling of the Corona of the Sun and Solar-like Stars: From a Three-dimensional Magnetohydrodynamic Model to Synthetic Extreme-Ultraviolet Spectra. ApJ, 638:1086–1100.

[81] Phillips, K., Feldman, U., and Landi, E. 2008. *Ultraviolet and X-ray Spectroscopy of the Solar Atmosphere*. Cambridge Astrophysics Series.

[82] Podladchikova, O. and Berghmans, D. 2005. Automated Detection Of Eit Waves And Dimmings. Sol. Phys., 228:265–284.

[83] Press, W. H., Teukolsky, S. A., Vetterling, W. T., and Flannery, B. P. 1992. Numerical recipes in C. Cambridge: University Press.

[84] Qiu, J., Wang, H., Chae, J., and Goode, P. R. 1999. Counter-streaming Mass Flow and Transient Brightening in Active Region Loops. Sol. Phys., 190:153–165.

[85] Robbrecht, E. and Berghmans, D. 2004. Automated recognition of coronal mass ejections (CMEs) in near-real-time data. A&A, 425:1097–1106.

[86] Robbrecht, E., Verwichte, E., Berghmans, D., Hochedez, J. F., Poedts, S., and Nakariakov, V. M. 2001. Slow magnetoacoustic waves in coronal loops: EIT and TRACE. A&A, 370:591–601.

[87] Robinson, D. and Milanfar, P. 2004. Fundamental performance limits in image registration. IEEE Transactions on Image Processing, 13(9):1185–1199.

[88] Rosa, D., Vrsnak, B., Bozic, H., Brajsa, R., Ruzdjak, V., Schroll, A., and Wohl, H. 1998. A Method to Determine the Solar Synodic Rotation Rate and the Height of Tracers. Sol. Phys., 179:237–252.

[89] Roudier, T., Rieutord, M., Malherbe, J. M., and Vigneau, J. 1999. Determination of horizontal velocity fields at the sun's surface with high spatial and temporal resolution. A&A, 349:301–311.

[90] Roša, D., Brajša, R., Vršnak, B., and Wöhl, H. 1995. The Relation between the Synodic and Sidereal Rotation Period of the Sun. Sol. Phys., 159:393–398.

[91] Schrijver, C. J. 2001. Catastrophic cooling and high-speed downflow in quiescent solar coronal loops observed with TRACE. Sol. Phys., 198:325–345.

[92] Schrijver, C. J., Title, A. M., Berger, T. E., Fletcher, L., Hurlburt, N. E., Nightingale, R. W., Shine, R. A., Tarbell, T. D., Wolfson, J., Golub, L., Bookbinder, J. A., Deluca, E. E., McMullen, R. A., Warren, H. P., Kankelborg, C. C., Handy, B. N., and de Pontieu, B. 1999. A new view of the solar outer atmosphere by the Transition Region and Coronal Explorer. Sol. Phys., 187:261–302.

[93] Schrijver, C. J., Aschwanden, M. J., and Title, A. M. 2002. Transverse oscillations in coronal loops observed with TRACE I. An Overview of Events, Movies, and a Discussion of Common Properties and Required Conditions. Sol. Phys., 206:69–98.

[94] Schroeter, E. H. 1985. The solar differential rotation - Present status of observations. Sol. Phys., 100:141–169.

[95] Schuck, P. W. 2006. Tracking Magnetic Footpoints with the Magnetic Induction Equation. ApJ, 646:1358–1391.

[96] Schuck, P. W. 2008. Tracking Vector Magnetograms with the Magnetic Induction Equation. ApJ, 683:1134–1152.

[97] Shi, J. and Tomasi, C. 1994. Good Features to Track. In *IEEE Conference on Computer Vision and Pattern Recognition (CVPR'94)*. Seattle.

[98] Simon, G. W. and Leighton, R. B. 1964. Velocity Fields in the Solar Atmosphere. III. Large-Scale Motions, the Chromospheric Network, and Magnetic Fields. ApJ, 140:1120–+.

[99] Simon, G. W., Title, A. M., Topka, K. P., Tarbell, T. D., Shine, R. A., Ferguson, S. H., Zirin, H., and SOUP Team. 1988. On the relation between photospheric flow fields and the magnetic field distribution on the solar surface. ApJ, 327:964–967.

[100] Simoncelli, E. P. 1999. Bayesian Multi-scale Differential Optical Flow. In Jähne, B., Haussecker, H., and Geissler, P., editors, *Handbook of Computer Vision and Applications*, volume 2, pages 397–422. Academic Press, San Diego.

[101] Simoncelli, E. P., Adelson, E. H., and Heeger, D. J. 1991. Probability Distributions of Optical Flow. In *Proc Conf on Computer Vision and Pattern Recognition*, pages 310–315. IEEE Computer Society, Mauii, Hawaii.

[102] Vaiana, G. S. and Rosner, R. 1978. Recent advances in coronal physics. ARA&A, 16:393–428.

[103] Verri, A. and Poggio, T. 1989. Motion Field and Optical Flow: Qualitative Properties. IEEE Transactions on Pattern Analysis and Machine Intelligence, PAMI-11(5):490–498.

[104] Verwichte, E., Nakariakov, V. M., Ofman, L., and Deluca, E. E. 2004. Characteristics of transverse oscillations in a coronal loop arcade. Sol. Phys., 223:77–94.

[105] Vršnak, B., Rošd, A., Božić, H., Brajša, R., Ruždjak, V., Schroll, A., and Wöhl, H. 1999. Height of Tracers and the Correction of the Measured Solar Synodic Rotation Rate: Demonstration of the Method. Sol. Phys., 185:207–225.

[106] Vršnak, B., Brajša, R., Wöhl, H., Ruždjak, V., Clette, F., and Hochedez, J.-F. 2003. Properties of the solar velocity field indicated by motions of coronal bright points. A&A, 404:1117–1127.

[107] Welsch, B. T., Fisher, G. H., Abbett, W. P., and Regnier, S. 2004. ILCT: Recovering Photospheric Velocities from Magnetograms by Combining the Induction Equation with Local Correlation Tracking. ApJ, 610:1148–1156.

[108] Wilcox, J. M. and Howard, R. 1970. Differential Rotation of the Photospheric Magnetic Field. Sol. Phys., 13:251–260.

[109] Winebarger, A. R., DeLuca, E. E., and Golub, L. 2001. Apparent Flows above an Active Region Observed with the Transition Region and Coronal Explorer. ApJ, 553:L81–L84.

[110] Winebarger, A. R., Warren, H., van Ballegooijen, A., DeLuca, E. E., and Golub, L. 2002. Steady Flows Detected in Extreme-Ultraviolet Loops. ApJ, 567:L89–L92.

[111] Young, C. A. and Gallagher, P. T. 2008. Multiscale Edge Detection in the Corona. Sol. Phys., 248:457–469.

[112] Zhukov, A. N. and Auchère, F. 2004. On the nature of EIT waves, EUV dimmings and their link to CMEs. A&A, 427:705–716.